
Phase-field modeling of thermal fracture and its applications to additive manufacturing

Zur Erlangung des akademischen Grades Doktor-Ingenieur (Dr.-Ing.)
Genehmigte Dissertation von Hui Ruan aus Anhui, China
Tag der Einreichung: 18.09.2024, Tag der Prüfung: 18.11.2024

1. Gutachten: Prof. Dr. Bai-Xiang Xu
 2. Gutachten: Prof. Dr. Dietmar Gross
- Darmstadt, Technische Universität Darmstadt



TECHNISCHE
UNIVERSITÄT
DARMSTADT

Materials and Earth
Sciences Department
Mechanics of Functional
Materials

Phase-field modeling of thermal fracture and its applications to additive manufacturing

Accepted doctoral thesis by Hui Ruan

Date of submission: 18.09.2024

Date of thesis defense: 18.11.2024

Darmstadt, Technische Universität Darmstadt

Bitte zitieren Sie dieses Dokument als:

URN: urn:nbn:de:tuda-tuprints-288999

URL: <https://tuprints.ulb.tu-darmstadt.de/id/eprint/28899>

Jahr der Veröffentlichung auf TUprints: 2024

Dieses Dokument wird bereitgestellt von tuprints,

E-Publishing-Service der TU Darmstadt

<https://tuprints.ulb.tu-darmstadt.de>

tuprints@ulb.tu-darmstadt.de

Die Veröffentlichung steht unter folgender Creative Commons Lizenz:

Namensnennung 4.0 International

<https://creativecommons.org/licenses/by/4.0/>

This work is licensed under a Creative Commons License:

Attribution 4.0 International

<https://creativecommons.org/licenses/by/4.0/>

追风赶月莫停留，平芜尽处是春山。

*Pursue the wind and moon, do not stay;
Where plains end, spring mountains lay.*

Erklärungen laut Promotionsordnung

§ 8 Abs. 1 lit. d PromO

Ich versichere hiermit, dass zu einem vorherigen Zeitpunkt noch keine Promotion versucht wurde. In diesem Fall sind nähere Angaben über Zeitpunkt, Hochschule, Dissertationsthema und Ergebnis dieses Versuchs mitzuteilen.

§ 9 Abs. 1 PromO

Ich versichere hiermit, dass die vorliegende Dissertation – abgesehen von den in ihr ausdrücklich genannten Hilfen – selbstständig verfasst wurde und dass die „Grundsätze zur Sicherung guter wissenschaftlicher Praxis an der Technischen Universität Darmstadt“ und die „Leitlinien zum Umgang mit digitalen Forschungsdaten an der TU Darmstadt“ in den jeweils aktuellen Versionen bei der Verfassung der Dissertation beachtet wurden.

§ 9 Abs. 2 PromO

Die Arbeit hat bisher noch nicht zu Prüfungszwecken gedient.

Darmstadt, 18.09.2024

H. Ruan

Acknowledgements

First and foremost, I would like to sincerely thank my advisor Prof. Dr. Bai-Xiang Xu for her guidance and help throughout my doctoral research. This endeavor would have not been possible without her. She teaches and trains me to do research in a scientifically critical way and encourages me to be an independent researcher. I'm impressed by her broad knowledge crossing various disciplines. Her devotion to research and work ethic are also a role model to me.

Meanwhile, I'm deeply grateful to Prof. Dr. Dietmar Gross, who introduced me to this vigorous group and co-supervised my PhD thesis. He is always willing to provide help and support for me whenever needed. I have learned and benefited enormously every time we meet and discuss, both in terms of scientific research and in my personal development. His passion and meticulous attitude towards research have a profound influence on me.

I would like to express my gratitude to Prof. Dr. Karsten Durst for being my second supervisor and reviewer of the thesis. I would like to thank Prof. Dr. Ralf Müller for reviewing this thesis.

My heartfelt thanks go to my colleagues Dr. Shahed Rezaei and Dr. Yangyiwei Yang for their invaluable assistance, especially at the beginning of this journey. Shahed helped me and guided me when I started this research. I enjoyed the discussions with him, from whom I learned a lot. Yang is helpful both in research and daily routines, particularly when I first arrived at Darmstadt. I also appreciate the fruitful discussions with Dr. Xianglong Peng and Dr. Yang Bai.

I would like to thank the members of Mechanics of Functional Materials group. I enjoy the time working with current and former colleagues including Somnath Bharech, Dr. Timileyin David Oyedeji, Mozhdeh Fathidoost, Abdullah Shafqat, Dr. Xiandong Zhou, Dr. Binbin Lin, Dr. Kai Wang, Dr. Christoph Reimuth, Wanxin Chen, Yifan Suo, Dr. Jiajun Sun, Xiangfeng Li, Tiansheng Liu, Junlong Ma, Patrick Kühn, Sebastian Wissel, Aditi Mohadarkar, Eduardo Parma, Cerun Alex Varkey, Jacob Niikoi Okoe-Amon, Armin Asheri,

Youngseon Yeon, Dr. Behnam Sobhaniaragh, Bondi Prasanth, Dr. Da Chen, Zirui Liu, Eren Foya, Nick Finger and others. A big shout to Maren Arnold for all her kind help and administrative support, and equally important, the happy laughter she brings.

I would like to express special thanks to my friends Chuan Yu, Wei Liu, Shuo Wang and Renjie Zheng, as well as Bingzong Wang and Shengran Zhang back in China. Though thousands of miles away, we talk, meet, celebrate and enjoy time together at traditional festivals, which are always full of joy and laughter. I also thank Xin Jin, Honghong Tian, Yaquan Sun, Cheng Chen, Hangxu Li, Junfeng Cai, Jian Zhang, Dr. Wei Li, Dr. Jiongjie Liu, Dr. Yongchao Zhu and others.

I would like to acknowledge highly the China Scholarship Council for the financial support of my whole doctoral studies. The access to the Lichtenberg High-Performance Computer and the technique support from the HHLR, Technische Universität Darmstadt are also appreciated.

Last but not least, I dedicate this work to my parents and sister for their unwavering love, support and encouragement. I would never have made it without you.

Hui Ruan
Darmstadt, September 2024

Abstract

Modeling and prediction of fracture processes remain challenging problems in computational mechanics, particularly in a multiphysics environment. In various practical applications, fracture is coupled with other involved physics which in turn severely influences the damage progression inside the material. Thermal fracture is universal in many branches of engineering applications, and is one of the most devastating defects in the metal additive manufacturing process. Due to the interactive physics involved, the computational simulation of such a process is challenging. This thesis is dedicated to understanding the fracture mechanism of such a complex material system, in particular the thermal cracking mechanisms of the additive manufacturing process, and the fracture behaviors of additively manufactured parts.

This thesis presents a thermodynamically consistent framework for thermo-elastic coupled brittle fracture at small strains using the phase-field model. The coupling mechanisms such as damage-informed thermomechanics and heat conduction, and temperature-dependent fracture properties, as well as different phase-field fracture formulations, are discussed. Numerical examples show that the proposed model is capable of simulating thermal brittle fracture, and the coupling mechanisms are indispensable to the accurate prediction of the thermal fracture process. Moreover, the phase-field model for thermal ductile fracture in thermo-elasto-plastic materials undergoing finite deformation is developed. Thereby the intercoupling mechanisms among elastoplasticity, phase-field crack and heat transfer are considered comprehensively. The finite element implementation of the coupled phase-field model is validated by comparing simulation results of a tensile test of an I-shape specimen, encompassing elastoplasticity, hardening, necking, crack initiation and propagation with experimental results.

The validated models are further employed to simulate the multiphysics hot cracking phenomenon in additive manufacturing in the context of an interpolated temperature solution, the phenomenological model, and the powder-resolved model of powder bed fusion. Thereby not only the classical thermal strain but also the solidification shrinkage are considered to calculate the thermal stress. Simulation results reveal certain key features of hot cracking and its dependency on process parameters like laser power and scan speed. A higher laser power and a lower scanning speed are favorable for keyhole

mode hot cracking while a lower laser power and a higher scanning speed tend to form the conduction mode cracking. These findings provide valuable insights into the fundamental understanding of crack formation mechanisms and process optimization.

Furthermore, a multiscale framework using the cohesive phase-field fracture method is presented to investigate the anisotropic fracture of additively manufactured parts. Herein, the anisotropic properties including anisotropic elasticity and anisotropic fracture resistance are considered, with both effects on crack patterns studied separately and combined. The orientation-dependent elastic moduli are calculated by the computational homogenization approach, while the stress-based spectral decomposition method of stress and strain energy is adopted as a result of anisotropic elasticity. A direction-dependent structural tensor which relates to the printing process is introduced to the phase-field fracture model to include the anisotropic fracture toughness. The simulation results show that it is necessary to consider both anisotropic elasticity and anisotropic fracture properties to accurately capture the fracture behaviors of additively manufactured parts.

Zusammenfassung

Die Modellierung und Vorhersage von Bruchvorgängen ist nach wie vor ein schwieriges Problem in der Computermechanik, insbesondere vor einem multiphysikalischem Hintergrund. In verschiedenen praktischen Anwendungen ist der Bruchmechanik mit anderen beteiligten physikalischen Vorgängen gekoppelt, die ihrerseits den Verlauf der Schädigung im Material stark beeinflussen. Thermischer Bruch ist in vielen Bereichen des Ingenieurwesens allgegenwärtig und gehört zu den verheerendsten Defekten bei der additiven Fertigung von Metallen. Aufgrund der interaktiven Physik ist die rechnerische Simulation eines solchen Prozesses eine Herausforderung. Diese Arbeit widmet sich dem Verständnis der Bruchmechanismen eines solch komplexen Materialsystems, insbesondere der thermischen Rissmechanismen des additiven Fertigungsprozesses und des Bruchverhaltens von additiv gefertigten Teilen.

In dieser Arbeit wird ein thermodynamisch konsistenter Rahmen für thermoelastisch gekoppelten Sprödbruch bei kleinen Dehnungen unter Verwendung des Phasenfeldmodells vorgestellt. Es werden die Kopplungsmechanismen wie schädigungsinformierte Thermomechanik und Wärmeleitung und temperaturabhängige Brucheigenschaften sowie verschiedene Phasenfeld-Bruchformulierungen diskutiert. Numerische Beispiele zeigen, dass das vorgeschlagene Modell in der Lage ist, thermischen Sprödbruch zu simulieren, und dass die Kopplungsmechanismen für die genaue Vorhersage des thermischen Bruchprozesses unerlässlich sind. Darüber hinaus wird das Phasenfeldmodell für thermisch duktilen Bruch in thermoelasto-plastischen Materialien, die einer endlichen Verformung unterworfen sind, entwickelt. Dabei werden die Kopplungsmechanismen zwischen Elastoplastizität, Phasenfeldbruch und Wärmetransport umfassend berücksichtigt. Die Finite-Elemente-Implementierung des gekoppelten Phasenfeldmodells wird durch den Vergleich der Simulationsergebnisse eines Zugversuchs an einer I-förmigen Probe, der Elastoplastizität, Verfestigung, Einschnürung, Rissinitiierung und -ausbreitung umfasst, mit experimentellen Ergebnissen validiert.

Die validierten Modelle werden weiter eingesetzt, um das multiphysikalische Heißrissphänomen in der additiven Fertigung im Kontext einer analytischen Temperaturlösung, des phänomenologischen Modells und des pulveraufgelösten Modells der Pulverbettsschmelze zu simulieren. Dabei wird nicht nur die klassische thermische Dehnung, sondern auch

die Erstarrungsschrumpfung berücksichtigt, um die thermische Belastung zu berechnen. Die Simulationsergebnisse zeigen bestimmte Schlüsselmerkmale der Heißrissbildung und ihre Abhängigkeit von Prozessparametern wie Laserleistung und Scangeschwindigkeit. Eine höhere Laserleistung und eine geringere Scangeschwindigkeit begünstigen die Heißrissbildung im Keyhole-Mode, während eine geringere Laserleistung und eine höhere Scangeschwindigkeit eher zur Bildung von Rissen im Conduction-Mode führen. Diese Ergebnisse liefern wertvolle Einblicke in das grundlegende Verständnis der Rissbildungsmechanismen und der Prozessoptimierung.

Darüber hinaus wird ein multiskaliger Rahmen unter Verwendung der kohäsiven Phasenfeld-Bruchmethode vorgestellt, um den anisotropen Bruch von additiv gefertigten Teilen zu untersuchen. Dabei werden die anisotropen Eigenschaften einschließlich der anisotropen Elastizität und der anisotropen Bruchfestigkeit berücksichtigt, wobei beide Auswirkungen auf die Rissmuster sowohl getrennt als auch kombiniert untersucht werden. Die orientierungsabhängigen Elastizitätsmodule werden mit dem Ansatz der rechnergestützten Homogenisierung berechnet, während die spannungsbasierte spektrale Zerlegungsmethode der Spannungs- und Dehnungsenergie als Ergebnis der anisotropen Elastizität übernommen wird. Ein richtungsabhängiger struktureller Tensor, der sich auf den Druckprozess bezieht, wird in das Phasenfeld-Bruchmodell eingeführt, um die anisotrope Bruchzähigkeit zu berücksichtigen. Die Simulationsergebnisse zeigen, dass es notwendig ist, sowohl die anisotrope Elastizität als auch die anisotropen Brucheigenschaften zu berücksichtigen, um das Bruchverhalten von additiv gefertigten Teilen genau zu erfassen.

Contents

Acknowledgements	i
Abstract	iii
1 Introduction	1
1.1 Motivation and background	1
1.2 Objectives and outline	6
2 Theoretical background	9
2.1 Kinematics	9
2.2 Stress measure and momentum balance	12
2.2.1 Stress measure	12
2.2.2 Balance of linear momentum	13
2.3 Thermodynamic principles and constitutive relations	14
2.3.1 Thermodynamic principles	14
2.3.2 Constitutive laws	17
2.4 Fracture mechanics	19
2.4.1 Griffith's theory	19
2.4.2 Stress intensity factor	20
2.4.3 J-integral	22
2.5 Phase-field modeling of fracture	23
3 Thermo-elastic Phase-field Brittle Fracture at Small Strains	33
3.1 Thermo-elastic phase-field brittle fracture model	33
3.1.1 Energy dissipation inequality	33
3.1.2 Damage informed thermoelasticity	35
3.1.3 Temperature-dependent phase-field fracture model	37
3.1.4 Damaged informed heat conduction	41
3.1.5 Summary of governing equations	42
3.2 Numerical implementation	43
3.2.1 Finite element discretization	43

3.2.2 Staggered solution scheme	44
3.3 Single-edge notched tension test	47
3.4 Quenching test	52
4 Thermo-elasto-plastic Phase-field Ductile Fracture at Finite Strains	57
4.1 Thermo-elasto-plastic phase-field ductile fracture model at finite strains . .	57
4.1.1 Kinematics	57
4.1.2 Thermodynamics: Dissipation inequality	59
4.1.3 Damage informed Elastoplastiy	60
4.1.4 Phase-field modeling of ductile fracture	64
4.1.5 Heat transfer	65
4.1.6 Summary of the coupled model	66
4.2 Numerical implementation	68
4.2.1 Finite element discretization	68
4.2.2 Return-mapping algorithm	70
4.3 I-shape specimen tensile test	71
4.3.1 Benchmark example: tensile test of I-shape specimen	72
4.3.2 characteristic parameters study of the model	75
5 Thermal Cracking in Additive Manufacturing	83
5.1 Solidification shrinkage	84
5.2 Hot cracking with interpolated elliptic temperature profile	85
5.3 Hot cracking in Powder Bed Fusion model	89
5.3.1 Hot cracking in the phenomenological model of PBF	89
5.3.2 Hot cracking in the powder-resolved model of PBF	97
6 Phase-field Anisotropic Fracture of Additively Manufactured Parts	103
6.1 Introduction	103
6.2 Phase-field modeling of anisotropic fracture	106
6.2.1 Phase-field model of anisotropic brittle fracture	106
6.2.2 Effective elastic moduli based on computational homogenization . .	109
6.3 Numerical example: fracture of single-edge notched specimen	111
6.3.1 Mode I fracture with isotropic elasticity	112
6.3.2 Mode I fracture with anisotropic elasticity	112
6.3.3 Mode I fracture with anisotropic fracture toughness	114
6.3.4 Mode I fracture with anisotropic elasticity and fracture toughness .	117
6.4 Anisotropic fracture simulations of additively manufactured parts	119
6.4.1 Homogenization of elastic properties	120



6.4.2	Anisotropic fracture of additively manufactured parts	120
6.5	Conclusions and outlook	122
7	Conclusions and Outlook	123
7.1	Conclusions	123
7.2	Outlook	125
	Bibliography	127
	Curriculum Vitae	143
	List of Publications	145

List of Figures

1.1	Experimental observations of hot cracking in metal additive manufacturing. (a) and (b) cracking in single layer AM process [11]. (c) and (d) for multilayer AM processes [12, 13].	2
1.2	Overview of cracking behavior of AM alloys showing the categories of cracking (inner layer), strategies (intermediate layer) and possible methods (outer layer) to inhibit cracking [17].	4
2.1	Finite deformation of a continuous body.	9
2.2	Stress vector, and Cauchy stress tensor and its components.	12
2.3	An infinite plate with a central crack under tension.	19
2.4	Schematic of three crack modes.	21
2.5	Arbitrary contour around the crack tip.	22
2.6	(a) Sharp crack and (b) diffusive crack modeling at $x = 0$	23
2.7	Diffusive crack interface with different length scale parameter ℓ_0	26
2.8	Crack phase-field profile $d(x)$ with different crack geometric function $\omega(d)$. For $\omega(d) = d^2$, the crack phase-field has infinite support, and for $\omega(d) = d$ and $\omega(d) = 2d - d^2$, the phase-field has finite support.	27
2.9	Plots of quadratic, cubic and quartic degradation function.	29
3.1	(a) Sharp interface and (b) diffusive interface of a crack in a cracked body.	38
3.2	Results of single-edge notched tension test under thermo-mechanical boundary conditions. (a) Comparison of damage level and (b) Reaction force-displacement curve of the AT2 model and the CPF model with different ℓ_0	48
3.3	Single-edge notched tension test under thermo-mechanical loading. Crack patterns and temperature profiles for case 3 with (a and c) and without (b and d) thermal conductivity degradation. (e) Reaction force-displacement curves for different thermal loading and (f) Temperature profiles along A-A for different thermal loading with and without thermal conductivity degradation.	49

3.4	Snapshots of heat flux for cases with degraded (left column) and constant (right column) thermal conductivity for CPF model (a and b) and AT2 model (c and d).	51
3.5	Quenching tests with different initial temperatures θ_0 . Comparison of crack patterns between numerical and experimental results. Reprinted from [120] with permission.	54
4.1	Schematic of the coupling mechanism among elastoplasticity, crack phase-field and heat transfer.	58
4.2	Tensile test of I-shape flat Steel-1.0553 specimen. (a) Geometry and boundary conditions, (b) experimental observations during tensile test [81] and (c) FE discretized mesh with a refined zone in the central regions.	72
4.3	Comparison of load-displacement curves of tensile test of I-shape specimen between simulation and experimental results [122]. The snapshots of simulations of the labeled points ($p1$) - ($p4$), ($q1$) - ($q4$) are shown in Fig. 4.4 and 4.5, respectively.	74
4.4	Elastoplastic response of tensile test of I-shape steel-1.0553 specimen without damage of points ($p1$) - ($p4$). Evolution of ($a1$) - ($a4$) equivalent plastic strain and ($b1$) - ($b4$) Von-Mises stress at displacement $u = [10.0, 12.0, 14.0, 15.0]$ mm.	75
4.5	Fracture process of tensile test of I-shape steel-1.0553 specimen at points ($q1$) - ($q4$). Evolution of ($a1$) - ($a4$) displacement, ($b1$) - ($b4$) damage, ($c1$) - ($c4$) equivalent plastic strain and ($d1$) - ($d4$) Von-Mises stress at displacement $u = [11.0, 12.0, 12.5, 12.9]$ mm.	76
4.6	Influence of length scale parameter on load-displacement curves of tensile test.	77
4.7	Influence of crack driving force on load-displacement curves of tensile test.	78
4.8	Influence of temperature on load-displacement curves of tensile test.	79
4.9	Influence of the threshold for the effective plastic strain α_{cp} in $g(d, \alpha)$ on load-displacement curves of tensile test of I-shape specimen	79
4.10	Influence of the threshold α_{cf} on load-displacement curves of tensile test.	80
4.11	Influence of the parameter a on load-displacement curves of tensile test.	80
5.1	Schematic of AM process and hot cracking phenomenon. Different hot cracking patterns in the melting pool for conduction mode and keyhole mode hot cracking with the increase of energy density	83
5.2	Volume change with temperature [131] and solidification shrinkage between θ_S and θ_L	85

5.3	(a) Schematic of the elliptic temperature field approximation. (b) Linear interpolation of temperature profile.	86
5.4	Hot cracking of single track of PBF with an aspect ratio of 1.0. (a) Normalized temperature field obtained by linear interpolation approximation, Hot cracking patterns with increasing solidification shrinkage strain, (b) $\alpha_{SS}=0$, (c) $4\alpha_t$ and (d) $26.7\alpha_t$, respectively.	87
5.5	Hot cracking of single track of PBF with different power densities in experimental observations. The image is reprinted from [134] under the terms of the Creative Commons CC-BY license.	89
5.6	Hot cracking patterns of a single track of PBF with different shapes of the melting pool. (a) Keyhole mode with an aspect ratio of 1.2. (b) Conduction mode with an aspect ratio of 0.5.	90
5.7	Normalized temperature profiles and hot cracking patterns of a single track of PBF with different temperature gradients c . (a) $c = 20$. (b) $c = 25$	91
5.8	The temperature field and phase indicator evolution of the 3D phenomenological PBF model (top) and the cross-section perpendicular to the scanning direction (bottom).	92
5.9	Hot cracking patterns of a slice of PBF with different laser powers.	93
5.10	Hot cracking patterns of a slice of PBF with different scanning speeds.	93
5.11	Hot cracking patterns of a slice of PBF with temperature-dependent mechanical properties under different laser powers.	94
5.12	Temperature (top) and phase indicator (bottom) evolution of two phenomenological LPBF processes. (a) $P = 200$ W, $v = 1000$ mm s ⁻¹ ; (b) $P = 100$ W, $v = 2000$ mm s ⁻¹ . The melting pool and fused zone are enlarged with higher laser power and slower scanning speed.	96
5.13	Hot cracking patterns of two phenomenological LPBF processes with (a) $P = 200$ W, $v = 1000$ mm s ⁻¹ and (b) $P = 100$ W, $v = 2000$ mm s ⁻¹	96
5.14	Workflow of hot cracking simulations in non-isothermal phase-field model for LPBF, including the powder deposition, the non-isothermal phase-field simulation and the thermo-elasto-plastic ductile fracture simulation.	98
5.15	Evolution of thermal-structure morphology during two non-isothermal phase-field models of LPBF. (a) $P = 30$ W, $v = 75$ mm s ⁻¹ at $t = [3.11, 3.40, 3.70]$ ms and (b) $P = 25$ W, $v = 100$ mm s ⁻¹ at $t = [2.13, 2.40, 2.67]$ ms. The upper rows show the temperature profiles and the lower rows show structural morphology.	99

5.16 Hot cracking patterns for two powder-resolved non-isothermal phase-field models of LPBF (a) $P = 30 \text{ W}$, $v = 75 \text{ mm s}^{-1}$ and (b) $P = 25 \text{ W}$, $v = 100 \text{ mm s}^{-1}$. Crackings are located near the melting pool boundaries due to the solidification shrinkage.	100
6.1 Effect of internal defects on the crack propagation of AM samples. (a) and (c) Influence of orientations of specimens on the interlayer pore distribution, (b) and (d) Defects distribution in 90° and 45° samples, respectively. Figure adapted from [147].	104
6.2 Experimental testing of anisotropic fracture of additively manufactured parts. The crack patterns with layer orientations $0^\circ, 30^\circ, 45^\circ, 60^\circ, 90^\circ$ [148]. Figure reproduced from [148].	105
6.3 Schematic of the additively manufactured specimens with different orientations. The scanning direction in the x - z plane is isotropic, and the building direction is along y axis. Figure adapted from [148].	107
6.4 Single-edge notched tension test. (a) Geometry and boundary conditions of the specimen, (b) Geometry of RVE, (c) Mesh of specimen.	111
6.5 Crack evolution of Mode I fracture of isotropic materials at timesteps $186\mu\text{s}$, $187\mu\text{s}$, $188\mu\text{s}$	112
6.6 Mode I fracture with anisotropic elasticity. (a1)-(a2) Homogenized Young's modulus and Poisson's ratio. (b1)-(b5) Crack patterns with orientation-dependent elasticity tensor. (c) The corresponding load-displacement curves.	113
6.7 Mode I fracture of single-edge notched tension test with anisotropic fracture toughness. Crack patterns of specimens with different preferential directions ($\phi = 0^\circ, 30^\circ, 45^\circ, 60^\circ, 90^\circ$) and degree of anisotropy (a1)-(a5) for $\beta = 5$, (b1)-(b5) for $\beta = 10$, c1-c5 for $\beta = 20$. (d) Load-displacement curves with different preferential orientation with $\beta = 5$, and (e) different β with same orientation $\phi = 0^\circ$	115
6.8 Relation of preferential direction and crack direction for single-notched tension test with anisotropic fracture toughness.	116
6.9 Stress fields at the crack tip.	116
6.10 Mode I fracture of single-edge notched tension test with anisotropic elasticity and fracture toughness. Crack patterns of specimens with different preferential directions ($\phi = 0^\circ, 30^\circ, 45^\circ, 60^\circ, 90^\circ$) and degree of anisotropy (a1)-(a5) for $\beta = 5$, (b1)-(b5) for $\beta = 10$, (c1)-(c5) for $\beta = 20$. (d) Load-displacement curves with different preferential orientation with $\beta = 5$, and (e) different β with same orientation $\phi = 0^\circ$	118

6.11 Tensile test of I-shape specimen with porous structures. (a) Geometry and (b) mesh of I-shape specimen, (c) a porous RVE of AM parts, and (d1)-(d2) Homogenized Young's modulus and Poisson's ratio. 119

6.12 Simulation results of anisotropic fracture of additively manufactured parts. (a1)-(a5) the crack patterns with layer orientation $0^\circ, 30^\circ, 45^\circ, 60^\circ, 90^\circ$, respectively. (b) the corresponding load-displacement curves. 121

List of Tables

2.1	Different crack geometric function $\omega(d)$ and the phase-field profile $d(x)$. . .	27
3.1	Different phase-field fracture models.	38
3.2	Material parameters for single edge notched tension test	47
3.3	Material parameters used for the quenching test.	53
3.4	Quantitative comparison of the quenching test under different initial temperatures.	54
4.1	Summary of the phase-field model of thermo-ductile fracture at finite strains	67
4.2	Material/numerical parameters used in the simulations	73
5.1	Temperature-dependent mechanical properties of SS316L	90
6.1	Material parameters for I-shape specimen tensile test	120

List of Symbols

Ω_0	Reference configuration
Ω_t	Current configuration
\mathbf{u}	Displacement
\mathbf{F}	Deformation gradient
\mathbf{F}^e	Elastic deformation gradient
\mathbf{F}^p	Plastic deformation gradient
\mathbf{F}^θ	Thermal deformation gradient
J	Determinant of deformation gradient
J^e	Determinant of elastic deformation gradient
\mathbf{C}	Right Cauchy–Green deformation tensor
\mathbf{C}^p	Plastic right Cauchy–Green deformation tensor
\mathbf{b}	Left Cauchy–Green deformation tensor
\mathbf{b}^e	Elastic left Cauchy–Green deformation tensor
\mathbf{E}	Green–Lagrangian strain tensor
\mathbf{e}	Euler–Almansi strain tensor
$\boldsymbol{\varepsilon}$	Infinitesimal strain tensor
$\boldsymbol{\varepsilon}_e$	Elastic strain tensor
$\boldsymbol{\varepsilon}_p$	Plastic strain tensor
$\boldsymbol{\varepsilon}_V$	Volumetric part of strain tensor
$\boldsymbol{\varepsilon}_D$	Deviatoric part of strain tensor
$\boldsymbol{\varepsilon}^+$	Tensile part of strain tensor
$\boldsymbol{\varepsilon}^-$	Compressive part of strain tensor
$\boldsymbol{\sigma}$	Cauchy stress tensor
\mathbf{P}	First Piola–Kirchhoff stress
\mathbf{S}	Second Piola–Kirchhoff stress
$\boldsymbol{\tau}$	Kirchhoff stress
\mathbf{s}	Deviatoric part of Kirchhoff stress
\mathbf{q}	Heat flux
Q	Internal heat supply

η	Specific entropy per unit mass
s	Net entropy production
e	Internal energy
ψ	Helmholtz free energy
ψ_e	Elastic energy
ψ_e^+	Tensile part of elastic energy
ψ_e^-	Compressive part of elastic energy
ψ_c	Fracture energy
ψ_p	Plastic hardening energy
Δ_p	Plastic dissipation energy
ψ_θ	Thermal energy
\mathcal{D}	Dissipated energy
θ	Temperature
θ_0	Reference temperature
ρ	Density
c	Specific heat capacity
\mathbf{t}	Surface traction
\mathbf{b}	Body force
\mathbb{C}	Elasticity tensor
λ, μ	Lamé constants
κ	Bulk modulus
f	Yield function
$\bar{\sigma}$	Effective stress
σ_Y	Yield strength
σ_∞	Ultimate strength
H	Hardening modulus
\mathcal{G}	Energy release rate
\mathcal{G}_c	Critical energy release rate
\mathcal{G}_{c0}	Reference critical energy release rate
γ_s	Specific surface energy
E	Young's modulus
K	Stress intensity factor
K_c	Fracture toughness
J	J-integral
d	Phase-field crack
Γ	Crack surface
γ	Crack surface energy density
ℓ_0	Length-scale parameter

$g(d)$	Degradation function
$\omega(d)$	Crack topology function
c_0	Scaling parameter
\mathcal{H}	History variable
ch	Irwin's length
ψ_{th}	Energy threshold for damage
σ_f	Fracture strength
α_t	Thermal expansion coefficient
α_{ss}	Solidification shrinkage coefficient
θ_S	Solidus temperature
θ_L	Liquidus temperature
k	Thermal conductivity
π	Internal microforce
ξ	Microstress
α	Hardening variable
H_p	Hardening function
α_{cp}, α_{cf}	Threshold of equivalent plastic strain
a, b	Profile parameter

Abbreviations

Abbreviation	Full name
AM	Additive Manufacturing
PBF	Powder Bed Fusion
LPBF	Laser Powder Bed Fusion
DED	Direct Energy Deposition
HTBR	High-Temperature Brittleness Range
GB	Grain Boundary
PK1	First Piola-Kirchhoff stress
PK2	Second Piola-Kirchhoff stress
PFM	Phase-field Model
PFF	Phase-field Fracture
CZM	Cohesive Zone Method
CPF	Cohesive Phase-Field
KTT	Karush-Kuhn-Tucker
AT	Ambrosio-Tortorelli
IBVP	Initial Boundary Value Problem
PDE	Partial Differential Equation
BC	Boundary Condition
IC	Initial Condition
HPC	High Performance Computing
SS	Solidification Shrinkage
FEM	Finite Element Method
MOOSE	Multiphysics Object-Oriented Simulation Environment
PETs	Portable Extensible Toolkit for Scientific Computation
AD	Automatic Differentiation
RVE	Representative Volume Element
PLA	Polylactic Acid

1 Introduction

1.1 Motivation and background

In recent decades, additive manufacturing (AM) has garnered significant attention due to its flexibility and ability to freely design and produce complex geometries, facilitating the rapid transformation of 3D digital prototypes into final components. The widespread adoption of AM has fundamentally altered the design and fabrication of mechanical parts, including the development of functionally graded and heterogeneous materials. Consequently, AM has become increasingly popular in industries such as aerospace, automotive, and energy. Among the various AM techniques, powder bed fusion (PBF) stands out as a prominent method for fabricating metal, polymer, and ceramic components. This process involves the precise deposition of thin layers of powder, which are selectively fused by laser or electron beams according to the digital prototype.

AM techniques have their advantages over other traditional manufacturing methods like casting or forging. However, they also suffer from challenges and bottlenecks. Various defects during the process of AM undermine the mechanical properties of additively manufactured components and thus limit their applications, such as porosity, inclusion, unmelting, lack-of-fusion and cracking [1, 2]. Hot cracking, occurring during the period of solidification or liquation of certain alloy systems is one of the most detrimental ones [3, 4]. As shown in Fig. 1.1, hot cracking phenomenon has been observed experimentally in aluminium alloys [5, 6, 2], nickel alloys [1, 7, 8] and steels [9]. The occurrence of hot cracking is a serious challenge for laser powder bed fusion (LPBF) when producing non-weldable nickel-base superalloys or aluminum. For example, while high specific strength series Al alloys are of interest in the aerospace and automotive industries, these alloys are susceptible to hot cracking issues during AM. Therefore, suitable manufacturing processes of LPBF that combine desirable fine microstructure and mechanical properties together with a low cracking susceptibility are a promising way to produce defect-free structures [10].

Hot cracking refers to the cracking phenomena associated with the presence of liquid in the interdendritic spaces during the solidification shrinkage (SS) [14, 15] and is localized in the fusion zone and partially-melted zone region of the heat-affected zone. Hot cracking

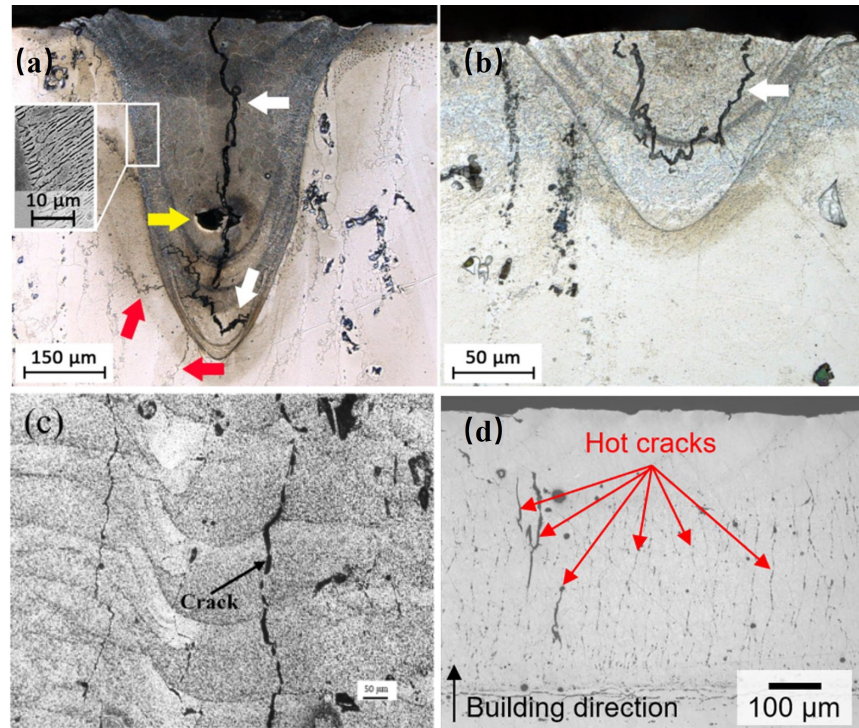


Figure 1.1: Experimental observations of hot cracking in metal additive manufacturing. (a) and (b) cracking in single layer AM process [11]. (c) and (d) for multilayer AM processes [12, 13].

takes two primary forms in metal AM, namely solidification cracking and liquation cracking. In the metal AM process, dendrites form between the molten pool and solid materials. Due to the fast heating and cooling during complex cyclical thermal history, the molten metal is in non-equilibrium solidification condition, prompting the formation of segregation and precipitates at the front of the solidification interface [5, 16]. These elements at the grain boundaries (GBs) decrease the fraction of the solid and form films enriched with solute elements in these regions. As the solidification process proceeds, the stress accumulates in films until the tensile stresses from solidification shrinkage and thermal contraction exceed the strength of the films, as residual stress can be transmitted via solids but not liquids. The lack of sufficient backfilling of liquid metal results in pronounced cracks, often characterized by dendritic protrusions on the crack surface [16, 17, 18]. In contrast, liquation cracking occurs directly outside the fusion zone in the partially melted zone.

The partially melted zone is subjected to temperatures between the liquidus and eutectic temperatures, resulting in localized melting of eutectic and GBs [17].

A lot of research into the hot cracking mechanism during the AM process has been performed in the literature. Chauvet et al. [19] studied the mechanism of cracking in a non-weldable Ni-based superalloy fabricated by selective electron beam melting and concluded that the presence of films is required and the hot cracking susceptibility depends on the GBs misorientation. Similarly, Chandra et al. [20] proposed a hot cracking criterion that considers various process parameters along with the GB inclination for Ni-based superalloys. Therein they concluded that the cracking occurred during the terminal stages of solidification in the form of solidification cracks due to the combined action of thermal strains and solidification shrinkage during rapid solidification. Recently, Li et al. [21] drew a similar conclusion by investigating the cracking initiation mechanism of the LPBF process, and showed that the solidification and thermal shrinkage of adjacent grains are the direct causes of cracking, which are crisscrossed horizontally and propagated through multilayers along the building direction. See also the works [11, 22] on the hot cracking mechanism of aluminum alloys and the influence of process parameters.

Based on the cracking mechanism, several potential strategies have been proposed to reduce or eliminate hot cracking. The first established approach is to modify the composition of the fabricated alloy to increase the amount of eutectic or lower the solidification range or high-temperature brittleness range (HTBR) [2, 10, 23]. In particular, the addition of Silicon to the alloy reduces the melting temperature and the solidification range, thus leading to decreased hot cracking. For example, most studies on AM of aluminum alloys were carried out with casting aluminum alloy (AlSi10Mg, AlSi12, AlSi7Mg0.3) which contains high levels of Silicon and limited HTBR and is thus less susceptible to hot cracking. Similarly, the addition of Nickel can mitigate cracking as well [24]. Meanwhile, grain refinement by the addition of nucleating agents results in better strain accommodation and higher resistance to cracking [5, 25]. Martin et al. [5] showed the addition of Sc and Zr in aluminum alloys enhanced its mechanical properties and reduced the cracking by promoting the formation of an equiaxed microstructure. Recently, David et al. [26] investigated the influence of the TiB₂ additions and process parameters on hot cracking and melt track formation during multi-layer LPBF of Al-2139 using high-speed in-situ synchrotron radiography coupled with synchrotron X-ray computed tomography, SEM imaging and EDS analysis of the as-built samples. Though the addition of TiB₂ reduces the volume fraction and average length of hot cracks, it increases the pore volume. See also similar works with other additions [27, 28, 29, 30, 31]. Moreover, the mitigation of hot cracking is potentially realized by adjustments of the process or pre-/post-treatment parameters, which help lower the thermal gradient and cooling rate. Soffel et al. [32] showed that the increasing substrate temperature by laser preheating and the reducing

specimen size leads to crack-free deposited structures. Recently, Cui et al. [33] employed a novel methodology to mitigate internal stresses and the formation of the films through the control of grain structure via an alternately reduced cooling method, rather than the linear reduction cooling method. Liu et al. [34] combined LPBF and post-hot isostatic pressing to effectively eliminate the crack density and enhance the high-temperature mechanical properties.

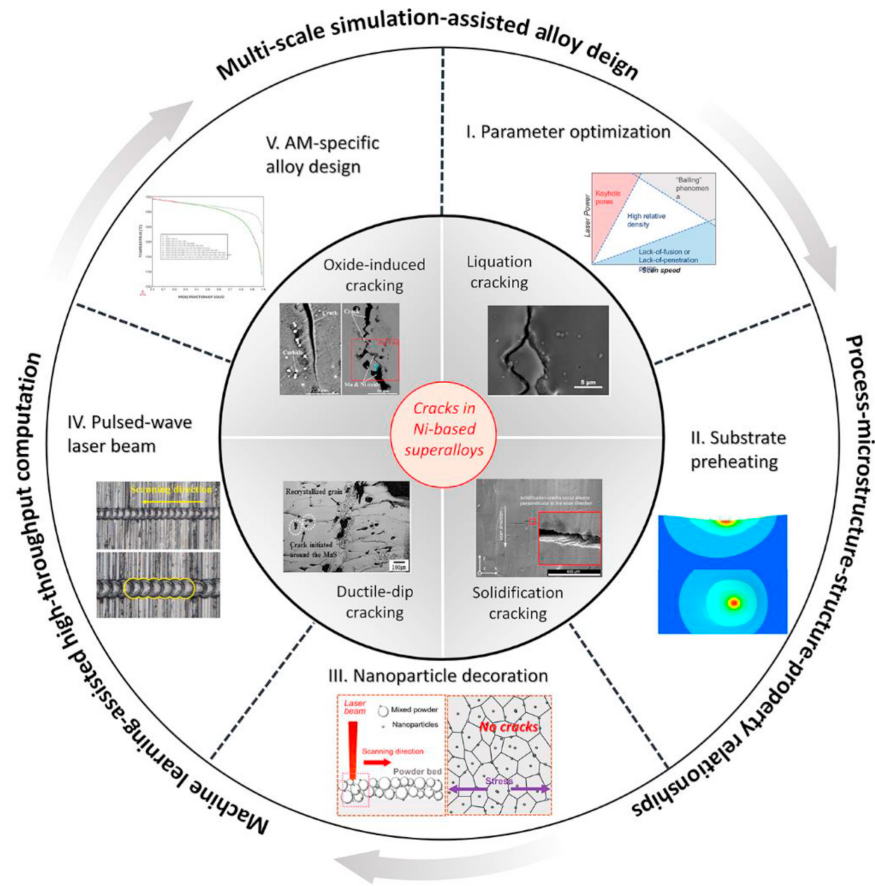


Figure 1.2: Overview of cracking behavior of AM alloys showing the categories of cracking (inner layer), strategies (intermediate layer) and possible methods (outer layer) to inhibit cracking [17].

While extensive studies on hot cracking of AM have been performed, understanding of

cracking mechanisms remains insufficient. Fig. 1.2 shows a comprehensive overview of the cracking behaviors in AM, strategies and possible methods to inhibit cracking [17]. Most research works focus on experimental observations via advanced optical equipment, which lacks transferability to other AM processes and requires high experimental effort and costs [13]. Therefore, to reduce the experimental effort and to achieve a physically based understanding of this phenomenon, a predictive model and effective simulation of the cracking process during AM are needed. Various crack criteria have been proposed for hot cracking, often first for traditional manufacturing methods, e.g., casting and welding. These criteria are mainly classified into two categories: mechanical and nonmechanical criteria [35, 36]. The former type involves stress-based [3, 37], strain-based [3, 38], and strain rate-based criteria [39, 40], while the latter deals with the vulnerable temperature range, phase diagram, and process parameters. Due to the complicated interplay between metallurgical and mechanical factors that influence the cracking, the physical phenomena associated with cracking are not explicitly described in most of these criteria [41, 42]. Recently, Suyitno et al. [43] proposed a micro porosity-related hot tearing criterion called SKK criterion. This criterion works well in considering the change in the deformation rate, cooling rate, grain size, casting speed, and casting recipe. Kou et al. [44] proposed a susceptibility criterion for cracking in a columnar dendritic structure, which only considers the events occurring at grain boundaries. Liu et al. [45] developed a solidification cracking model that incorporates solid-bridge fracture mechanisms and enables quantification of cracking susceptibility under various grain sizes and thermal conditions. Several works couple granular mechanics with the thermomechanical behavior of the solidifying alloys [46, 47, 48, 49], which highlight the hot tearing mechanism at a more microscopic scale.

Computational modeling of fracture has been studied extensively using different approaches. In the last decade, the regularized phase-field modeling of fracture has gained wide interest and tremendous attention in the engineering and applied mathematics communities, establishing itself as a robust, efficient, and versatile tool. In the framework of the phase-field method, the sharp interface is replaced by a continuous field variable, i.e., order parameter to differentiate multiple phases smoothly. Therefore, PFF describes the crack interface continuously and no additional tracking of the surface is needed in the fracture process including crack nucleation, propagation, merging, and branching. It does not need an ad-hoc failure criterion, and is also relatively simple to implement computationally with the advantage of no need to track crack topology explicitly. Moreover, based on the variational framework, it's easy to incorporate multiphysics (e.g. thermal field) in a straightforward manner.

Despite the previously mentioned research effort of numerical investigations of cracking in AM, they mainly focus on the microstructure formation and residual stress/strain and deformation, while do not directly relate the cracking behaviors to the AM process.

Furthermore, the relation between hot cracking and process parameters during AM is not clear. Therefore, it's of interest to develop an effective and efficient physical model to perform reliable numerical simulations of hot cracking during AM. On the other hand, the thermodynamic consistency of the fully coupled cohesive phase-field model for thermal fracture is not investigated in detail. One of the first goals of this work is to discuss the point by taking into account various coupling aspects between different fields. Moreover, the research into phase-field modeling of ductile fracture in a multiphysics environment is still in the early stage, especially when it comes to the coupling between damage, plasticity, and other physics under a multiphysics setting. Specifically, the applications of the phase-field model of thermal fracture are mainly limited to brittle fracture with small strain assumption, while the applications to ductile fracture with large deformation are also of great interest. Therefore, another contribution of this thesis is to extend the previous work to thermo-elasto-plastic coupled ductile fracture at finite strain, so that it can also apply to simulate the fracture process of a broad spectrum of metals/alloys and AM process of metals/alloys.

1.2 Objectives and outline

Based on the reviewed literature, the objectives of the dissertation are to develop a thermodynamically consistent phase-field fracture model to study the thermo-mechanical coupled fracture, including a thermo-elastic coupled brittle fracture model at small strains and thermo-elasto-plastic coupled ductile fracture model at finite strains. Thereafter, the models are used to investigate the hot cracking phenomenon in the AM process with the temperature field obtained from an interpolated temperature solution, a phenomenological PBF model and a non-isothermal phase-field model, respectively. Lastly, the homogenization-based anisotropic phase-field method is developed to study the anisotropic fracture behaviors of AM parts.

The outline of the thesis is organized as follows:

In Chapter 2, the foundations of the continuum mechanics and fracture mechanics are briefly introduced, including kinematics, strain and stress measures, thermodynamical principles, as well as several core concepts of linear elastic fracture mechanics, elastic-plastic fracture mechanics and phase-field modeling of fracture.

In Chapter 3, a thermo-elastic coupled cohesive phase-field (CPF) brittle fracture model at small strains is developed, and several numerical examples are studied. The coupling effects between displacement, heat transfer, and fracture are all taken into account. The length-scale insensitivity of CPF in a multiphysics environment is investigated.

In Chapter 4 the brittle fracture model is extended to thermo-elasto-plastic coupled

ductile fracture at finite strains. The model is validated by the experimental results of the tensile test of an I-shape specimen, and the influence of the model parameters on the fracture process is quantitatively compared.

The applications of the proposed models to study the hot cracking in AM are conducted in Chapter 5. Temperature profiles computed in three different ways including an interpolated temperature profile, the phenomenological model of PBF, and the powder-resolved model of PBF are utilized. The process parameters like the laser power and the scanning speed on the final crack pattern are investigated.

In Chapter 6, the anisotropic phase-field fracture model is developed to study the orientation-dependent fracture behaviors of additively manufactured parts. Thereby both the anisotropic elasticity and anisotropic fracture toughness are considered.

Chapter 7 presents the conclusions and outlook of the thesis.

2 Theoretical background

This thesis studies in the framework of continuum mechanics. Well-known continuum mechanics are used to describe the proposed model. To make the description self-contained and for the sake of clarity, the fundamentals of continuum mechanics and fracture mechanics are formulated in this Chapter.

2.1 Kinematics

Consider a body \mathcal{B} occupying a region Ω with a regular boundary $\partial\Omega$ in the three-dimensional Euclidean space \mathbb{R}^3 . Let $\Omega_0 \subset \mathbb{R}^3$ be the reference configuration with external boundary $\partial\Omega_0$ and $\Omega_t \subset \mathbb{R}^3$ be the current configuration with current boundary $\partial\Omega_t$ at time t .

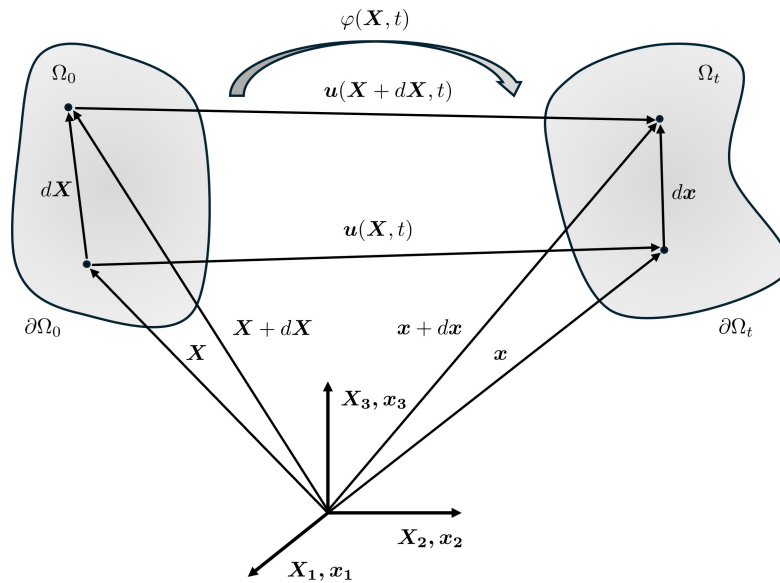


Figure 2.1: Finite deformation of a continuous body.

The deformation of the body, as shown in Fig. 2.1, is described by the deformation mapping

$$\varphi(\mathbf{X}, t) : \mathbf{X} \rightarrow \mathbf{x}, \quad (2.1)$$

which maps the reference material points $\mathbf{X} \in \Omega_0$ at time $t \in [0, \tau]$ onto the current material points $\mathbf{x} \in \Omega_t$ such that

$$\mathbf{x} = \varphi(\mathbf{X}, t), \quad (2.2)$$

where the position vector of a material point of the reference and current configuration can be expressed as

$$\mathbf{X} = [X_1 \ X_2 \ X_3]^T, \quad \mathbf{x} = [x_1 \ x_2 \ x_3]^T. \quad (2.3)$$

The deformation gradient is defined as

$$\mathbf{F} = \varphi_{,\mathbf{X}} = \frac{\partial \varphi(\mathbf{X}, t)}{\partial \mathbf{X}}, \quad (2.4)$$

where \mathbf{F} characterizes the deformation in the neighborhood of material point $d\mathbf{X}$, linearly mapping infinitesimal line element $d\mathbf{X}$ in the reference configuration into an infinitesimal line element $d\mathbf{x}$ in the current configuration. The mapping is unique and reversible, thus the determinant of \mathbf{F} satisfies

$$J = \det \mathbf{F} \neq 0. \quad (2.5)$$

The displacement of the point \mathbf{X} is given as

$$\mathbf{u}(\mathbf{X}, t) = \varphi(\mathbf{X}, t) - \mathbf{X}. \quad (2.6)$$

Consider the length ds of line $d\mathbf{x}$ in the deformed configuration,

$$ds^2 = d\mathbf{x}^T \cdot d\mathbf{x} = (\mathbf{F}d\mathbf{X})^T \cdot (\mathbf{F}d\mathbf{X}) = d\mathbf{X}^T \mathbf{F}^T \mathbf{F} d\mathbf{X} = d\mathbf{X}^T \mathbf{C} d\mathbf{X}, \quad (2.7)$$

where

$$\mathbf{C} = \mathbf{F}^T \mathbf{F} \quad (2.8)$$

is the right Cauchy–Green deformation tensor.

Likewise, in the undeformed configuration,

$$dS^2 = d\mathbf{X}^T \cdot d\mathbf{X} = (\mathbf{F}^{-1}d\mathbf{x})^T \cdot (\mathbf{F}^{-1}d\mathbf{x}) = d\mathbf{x}^T \mathbf{F}^{-T} \mathbf{F}^{-1} d\mathbf{x} = d\mathbf{x}^T \mathbf{b}^{-1} d\mathbf{x}, \quad (2.9)$$

where the left Cauchy–Green deformation tensor is defined as

$$\mathbf{b} = \mathbf{F} \mathbf{F}^T. \quad (2.10)$$

Associated with the undeformed configuration, a measure of the stretch of the line is given

$$\begin{aligned} ds^2 - dS^2 &= d\mathbf{x}^T \cdot d\mathbf{x} - d\mathbf{X}^T \cdot d\mathbf{X} = d\mathbf{X}^T \mathbf{C} d\mathbf{X} - d\mathbf{X}^T \cdot d\mathbf{X} \\ &= d\mathbf{X}^T (\mathbf{C} - \mathbf{I}) d\mathbf{X} = d\mathbf{X}^T (2\mathbf{E}) d\mathbf{X}, \end{aligned} \quad (2.11)$$

where

$$\mathbf{E} = \frac{1}{2}(\mathbf{C} - \mathbf{I}). \quad (2.12)$$

\mathbf{E} is the Green-Lagrangian strain tensor. Substituting Eq 2.4 and 2.8 into Eq 2.12 give

$$\begin{aligned} \mathbf{E} &= \frac{1}{2}(\mathbf{F}^T \mathbf{F} - \mathbf{I}) = \frac{1}{2} \left(\left[\frac{\partial \mathbf{u}}{\partial \mathbf{X}} + \mathbf{I} \right]^T \left[\frac{\partial \mathbf{u}}{\partial \mathbf{X}} + \mathbf{I} \right] - \mathbf{I} \right) \\ &= \frac{1}{2} \left(\frac{\partial \mathbf{u}}{\partial \mathbf{X}} + \left(\frac{\partial \mathbf{u}}{\partial \mathbf{X}} \right)^T + \left(\frac{\partial \mathbf{u}}{\partial \mathbf{X}} \right)^T \frac{\partial \mathbf{u}}{\partial \mathbf{X}} \right). \end{aligned} \quad (2.13)$$

Similarly, relative to the current configuration, the Euler-Almansi strain tensor reads

$$\begin{aligned} \mathbf{e} &= \frac{1}{2}(\mathbf{I} - \mathbf{F}^{-T} \mathbf{F}^{-1}) = \frac{1}{2} \left(\mathbf{I} - \left[\mathbf{I} - \frac{\partial \mathbf{u}}{\partial \mathbf{x}} \right]^T \left[\mathbf{I} - \frac{\partial \mathbf{u}}{\partial \mathbf{x}} \right] \right) \\ &= \frac{1}{2} \left(\frac{\partial \mathbf{u}}{\partial \mathbf{x}} + \left(\frac{\partial \mathbf{u}}{\partial \mathbf{x}} \right)^T - \left(\frac{\partial \mathbf{u}}{\partial \mathbf{x}} \right)^T \frac{\partial \mathbf{u}}{\partial \mathbf{x}} \right). \end{aligned} \quad (2.14)$$

In the case of infinitesimal deformation, the displacement $\|\mathbf{u}\| \ll 1$, the reference and the current configurations are considered to be identical. Hence, the position vector of material point \mathbf{X} is identical to that of \mathbf{x} , which implies

$$\Omega_t \approx \Omega_0, \quad \mathbf{x} = \mathbf{X} + \mathbf{u} \approx \mathbf{X}, \quad (2.15)$$

and the displacement gradients are infinitesimal,

$$\left| \frac{\partial \mathbf{u}}{\partial \mathbf{x}} \right| \ll 1, \quad (2.16)$$

the second-order term can be ignored, and Eq 2.13 and 2.14 reduce to

$$\mathbf{E} \approx \mathbf{e} \approx \boldsymbol{\varepsilon} = \frac{1}{2} \left(\frac{\partial \mathbf{u}}{\partial \mathbf{x}} + \left(\frac{\partial \mathbf{u}}{\partial \mathbf{x}} \right)^T \right), \quad (2.17)$$

where $\boldsymbol{\varepsilon}$ is the infinitesimal strain tensor.

In this thesis, Chapter 3 assumes small deformation, while Chapter 4 is in the context of finite deformation.

2.2 Stress measure and momentum balance

2.2.1 Stress measure

Consider the configuration Ω of the body \mathcal{B} subject to external forces, internal forces will be caused inside the body. A fictitious cross-section cutting the body into two parts is assumed, as schematically shown in Fig. 2.2(a). Let $\Delta \mathbf{f}$ denote the force acting on an infinitesimal area element ΔA at point \mathbf{x} .

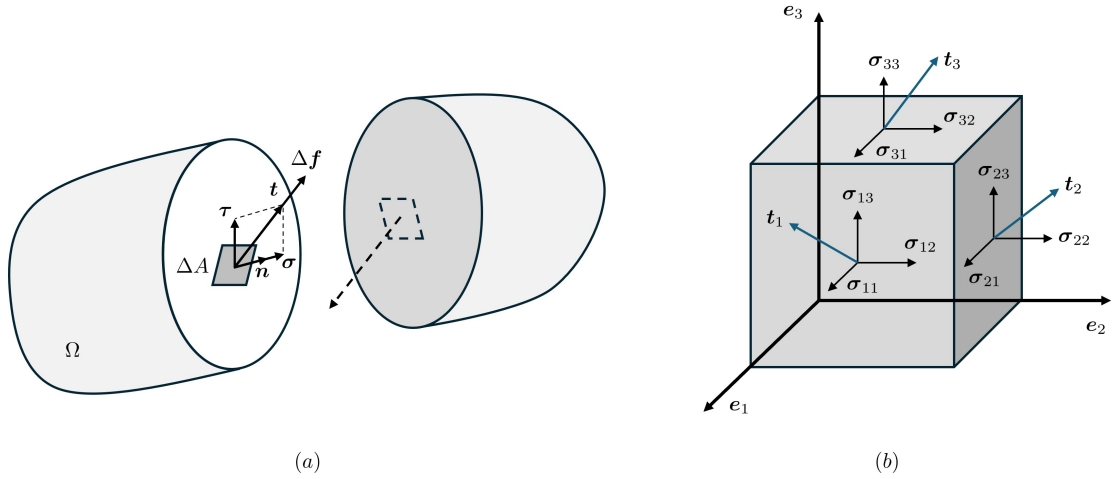


Figure 2.2: Stress vector, and Cauchy stress tensor and its components.

The Cauchy stress vector of a point is defined as

$$\mathbf{t} = \lim_{\Delta A \rightarrow 0} \frac{\Delta \mathbf{f}}{\Delta A} = \frac{\Delta \mathbf{f}}{\Delta A}. \quad (2.18)$$

The stress vector \mathbf{t} depends on the orientation of the normal vector of the surface \mathbf{n} .

According to Cauchy's theorem, which establishes that the traction vector in a point of a body depends linearly on the normal of the surface, i.e., there exists a second-order tensor field $\boldsymbol{\sigma}(\mathbf{x})$ such that

$$\mathbf{t}(\mathbf{x}, \mathbf{n}) = \boldsymbol{\sigma}(\mathbf{x}) \cdot \mathbf{n}, \quad (2.19)$$

where $\boldsymbol{\sigma}(\mathbf{x})$ is called Cauchy's stress tensor, and referred to as the true stress tensor. Using an orthonormal basis $\{\mathbf{e}_1, \mathbf{e}_2, \mathbf{e}_3\}$, the Cauchy stress reads

$$\boldsymbol{\sigma} = \sigma_{ij} \mathbf{e}_i \otimes \mathbf{e}_j, \quad (2.20)$$

where the components σ_{ij} given by

$$\sigma_{ij} = (\boldsymbol{\sigma} \mathbf{e}_i) \cdot \mathbf{e}_j. \quad (2.21)$$

As illustrated in Fig. 2.2(b). The first index i of σ_{ij} represents the direction of the normal vector of the section, while the second index j indicates the direction of the stress component itself. The Cauchy stress is written in matrix form as,

$$\boldsymbol{\sigma} = \begin{bmatrix} \sigma_{11} & \sigma_{12} & \sigma_{13} \\ \sigma_{21} & \sigma_{22} & \sigma_{23} \\ \sigma_{31} & \sigma_{32} & \sigma_{33} \end{bmatrix}, \quad (2.22)$$

where σ_{ii} ($i = 1, 2, 3$) are the normal stress, and σ_{ij} ($i \neq j, i, j = 1, 2, 3$) are the shear stress. The stress tensor fully characterizes the stress state at a point in the body, i.e., it uniquely determines the stress vector for an arbitrary section through the material point. The Cauchy stress is symmetric.

The counterpart stress in the reference configuration is the first Piola-Kirchhoff stress (PK1) \mathbf{P} , which describes the current force with respect to the surface element in the reference configuration,

$$\mathbf{P} = J \boldsymbol{\sigma} \mathbf{F}^{-T}. \quad (2.23)$$

In general, \mathbf{P} is non-symmetric. Further, the second Piola-Kirchhoff stress (PK2) \mathbf{S} is defined solely within the reference configuration,

$$\mathbf{S} = \mathbf{F}^{-1} \mathbf{P} = J \mathbf{F}^{-1} \boldsymbol{\sigma} \mathbf{F}^{-T}, \quad (2.24)$$

which relates the stress in the reference configuration with areas in the reference configuration, and it's a symmetric tensor.

2.2.2 Balance of linear momentum

Subject to body forces b_i which is distributed over the whole volume V and the surface traction t_i acting on the surface S , according to the balance of linear momentum,

$$\int_S t_i dA + \int_V b_i dV = 0. \quad (2.25)$$

In view of Eq. 2.19 and by applying Gauss' theorem, Eq. 2.25 reaches

$$\int_V (\sigma_{ij,j} + b_i) dV = 0. \quad (2.26)$$

Eq. 2.26 holds for any arbitrary volume, and thus,

$$\sigma_{ij,j} + b_i = 0, \quad (2.27)$$

or in the form of tensor notation

$$\nabla \cdot \boldsymbol{\sigma} + \mathbf{b} = \mathbf{0}. \quad (2.28)$$

2.3 Thermodynamic principles and constitutive relations

2.3.1 Thermodynamic principles

Energy conservation law

The first law of thermodynamics represents a detailed balance describing the interplay between the internal energy, the kinetic energy, the rate at which power is expended, and the heat transferred to the solid Ω , which is expressed by

$$\frac{d}{dt}(\mathcal{E} + \mathcal{K}) = \mathcal{W} + \mathcal{Q}, \quad (2.29)$$

where \mathcal{E} , \mathcal{K} , \mathcal{W} and \mathcal{Q} denote the net internal energy, the kinetic energy, the external power, and the heat flow, respectively.

$$\left\{ \begin{array}{l} \mathcal{E} = \int_{\Omega} \rho e dV \\ \mathcal{K} = \int_{\Omega} \frac{1}{2} \rho \dot{\mathbf{u}}^2 dV \\ \mathcal{W} = \int_{\partial\Omega} \mathbf{t} \cdot \dot{\mathbf{u}} dS + \int_{\Omega} \mathbf{b} \cdot \dot{\mathbf{u}} dV \\ \mathcal{Q} = - \int_{\partial\Omega} \mathbf{q} \cdot \mathbf{n} dS + \int_{\Omega} Q dV \end{array} \right. , \quad (2.30)$$

where ρ denotes the material density, e internal energy per unit mass, $\dot{\mathbf{u}}$ is the time derivative of displacement, \mathbf{t} denotes the surface traction, and \mathbf{b} the generalized body force, \mathbf{q} is the heat flux, \mathbf{n} the outward unit normal to $\partial\Omega$ and Q internal heat supply.

Substituting the equations in Eq. 2.30 into energy balance Eq. 2.29 yields

$$\frac{d}{dt} \int_{\Omega} \rho \left(e + \frac{1}{2} \dot{\mathbf{u}}^2 \right) dV = - \int_{\partial\Omega} \mathbf{q} \cdot \mathbf{n} dS + \int_{\Omega} Q dV + \int_{\partial\Omega} \mathbf{t} \cdot \dot{\mathbf{u}} dS + \int_{\Omega} \mathbf{b} \cdot \dot{\mathbf{u}} dV. \quad (2.31)$$

By integrating the balance equation of linear momentum (i.e. Newton's law), multiplied by the derivative of displacement over the domain, one can get

$$-\int_{\Omega} \boldsymbol{\sigma} : \dot{\boldsymbol{\varepsilon}} dV + \int_{\partial\Omega} \mathbf{t} \cdot \dot{\mathbf{u}} dS + \int_{\Omega} \mathbf{b} \cdot \dot{\mathbf{u}} dV = \frac{d}{dt} \int_{\Omega} \frac{1}{2} \dot{\mathbf{u}}^2 dV. \quad (2.32)$$

Substituting Eq. 2.32 into Eq. 2.31 and applying the divergence theorem, we obtain the following energy equilibrium equation

$$\int_{\Omega} (\rho \dot{e} - \boldsymbol{\sigma} : \dot{\boldsymbol{\varepsilon}} + \nabla \cdot \mathbf{q} - Q) dV = 0. \quad (2.33)$$

The identity in Eq. 2.33 is valid for any region, thus the local energy balance equation is obtained

$$\rho \dot{e} = \boldsymbol{\sigma} : \dot{\boldsymbol{\varepsilon}} - \nabla \cdot \mathbf{q} + Q. \quad (2.34)$$

In thermo-mechanical phase-field fracture analysis, besides the temperature θ and the total strain $\boldsymbol{\varepsilon}$, the state variables also include the crack phase-field d . Correspondingly, the external power \mathcal{W} is reformulated as

$$\mathcal{W} = \int_{\partial\Omega} (\mathbf{t} \cdot \dot{\mathbf{u}} + \mathbf{H} \cdot \nabla \dot{d}) dS + \int_{\Omega} (\mathbf{b} \cdot \dot{\mathbf{u}} + K \dot{d}) dV, \quad (2.35)$$

where \mathbf{H} is micro-traction on crack surfaces and K denotes the internal micro-forces, which will be discussed later in the following derivation. Thus the energy balance equation, which accounts for thermal diffusion and power produced by the micro and macro forces, is given

$$\rho \dot{e} = \boldsymbol{\sigma} : \dot{\boldsymbol{\varepsilon}} + K \dot{d} + \mathbf{H} \cdot \nabla \dot{d} - \nabla \cdot \mathbf{q} + Q. \quad (2.36)$$

Energy dissipation inequality

The second law of thermodynamics postulates that the rate of net entropy production \dot{s} in any convecting spatial region Ω is always nonnegative

$$\dot{s} = \int_{\Omega} \rho \dot{\eta} dV - \left(- \int_{\partial\Omega} \frac{\mathbf{q}}{\theta} \cdot \mathbf{n} + \int_{\Omega} \frac{Q}{\theta} \right) dV \geq 0, \quad (2.37)$$

where η is the specific entropy per unit mass, θ is the temperature. The first term on the right hand denotes the internal entropy and the second term denotes entropy flow, which is the rate at which entropy is transferred to Ω .

This inequality is valid for any region of the body and using the divergence theorem leads to the following local form of the irreversibility of the entropy production rate,

$$\rho\dot{\eta} + \nabla \cdot \left(\frac{\mathbf{q}}{\theta} \right) - \frac{Q}{\theta} \geq 0. \quad (2.38)$$

The fundamental inequality containing the first and second principles is obtained by replacing Q with the expression resulting from Eq. 2.36 of conservation of energy:

$$\rho\dot{\eta} + \nabla \cdot \left(\frac{\mathbf{q}}{\theta} \right) - \frac{1}{\theta} \left(\rho\dot{e} - \boldsymbol{\sigma} : \dot{\boldsymbol{\varepsilon}} - K\dot{d} - \mathbf{H} \cdot \nabla\dot{d} + \nabla \cdot \mathbf{q} \right) \geq 0. \quad (2.39)$$

Note that

$$\nabla \cdot \left(\frac{\mathbf{q}}{\theta} \right) = \frac{1}{\theta} \nabla \cdot \mathbf{q} - \frac{1}{\theta^2} \nabla\theta \cdot \mathbf{q}, \quad (2.40)$$

thus,

$$\rho(\theta\dot{\eta} - \dot{e}) + \boldsymbol{\sigma} : \dot{\boldsymbol{\varepsilon}} + K\dot{d} + \mathbf{H} \cdot \nabla\dot{d} - \frac{1}{\theta} \nabla\theta \cdot \mathbf{q} \geq 0. \quad (2.41)$$

Here we introduce the specific free energy ψ defined by the Legendre transform

$$\psi = e - \theta\eta, \quad (2.42)$$

where ψ is the Helmholtz free energy per unit mass, which measures the amount of obtainable work in a closed thermodynamic system. The rate form of the internal energy e is given by

$$\dot{\psi} = \dot{e} - \dot{\theta}\eta - \theta\dot{\eta}. \quad (2.43)$$

Substituting Eq. 2.43 into Eq. 2.41, the internal energy can be eliminated from the energy balance equation, and the local Clausius-Duhem inequality is obtained.

The second law of thermodynamics, expressed in the form of local Clausius-Duhem inequality, is utilized here to derive the thermodynamically consistent constitutive laws of the model. For this thermoelastic coupled problem, the local dissipated energy \mathcal{D} considering the power produced by the micro and macro forces, is given as

$$\mathcal{D} = \boldsymbol{\sigma} : \dot{\boldsymbol{\varepsilon}} + K\dot{d} + \mathbf{H} \cdot \nabla\dot{d} - \rho(\dot{\psi} + \dot{\theta}\eta) - \frac{1}{\theta} \nabla\theta \cdot \mathbf{q} \geq 0. \quad (2.44)$$

Here, $\boldsymbol{\sigma}$ is the Cauchy stress tensor, $\boldsymbol{\varepsilon}$ is the total strain, ψ denotes the Helmholtz free energy, η denotes the entropy, \mathbf{H} is micro-traction on crack surfaces, K is the internal micro-forces, and ρ is the material density.

Depending on the specific definition of Helmholtz free energy, the thermodynamic relations are determined. A detailed description of the thermo-elastic brittle fracture at small strains and thermo-elastoplastic ductile fracture at finite strains are presented in Chapter 3 and Chapter 4, respectively.

2.3.2 Constitutive laws

Elasticity

The constitutive laws are one of the core concepts in continuum mechanics, which are used to relate the stress and the strain measures. In general elastic material modeling in a small strain context, assuming the existence of the elastic strain energy, the constitutive equations can be given

$$\psi = \frac{1}{2} \boldsymbol{\varepsilon} : \mathbb{C} : \boldsymbol{\varepsilon}, \quad (2.45)$$

where \mathbb{C} is the fourth-order elasticity tensor. According to the definition of the Cauchy stress from the thermodynamic derivation in Sec. 2.3.1, the Cauchy stress can be obtained such that

$$\boldsymbol{\sigma} = \frac{\partial \psi}{\partial \boldsymbol{\varepsilon}}. \quad (2.46)$$

The elasticity tensor is defined as

$$\mathbb{C} = \frac{\partial^2 \psi}{\partial \boldsymbol{\varepsilon} \partial \boldsymbol{\varepsilon}}. \quad (2.47)$$

Thus, the constitutive law (generalized Hooke's law) reads

$$\boldsymbol{\sigma} = \mathbb{C} : \boldsymbol{\varepsilon}. \quad (2.48)$$

For isotropic elastic material, the elasticity tensor, expressed in Lamé constant λ and μ takes the form

$$\mathbb{C} = \lambda \mathbf{I} \otimes \mathbf{I} + 2\mu \mathbb{I}, \quad (2.49)$$

where \mathbf{I} and \mathbb{I} are the second-order unit tensor and fourth-order symmetric unit tensor, respectively.

The linear elastic material model is the most simplified one, among many others, for example, the thermo-elastic material model is used in Chapter 3 in the thesis.

Plasticity

Materials obey Hooke's law only in a limited range of small strains. When strained beyond an elastic limit, Hooke's law no longer applies, and the material starts to yield and deform plastically. To characterize the elastic-plastic response, the total strain is additively decomposed into an elastic part $\boldsymbol{\varepsilon}_e$ and a plastic part $\boldsymbol{\varepsilon}_p$,

$$\boldsymbol{\varepsilon} = \boldsymbol{\varepsilon}_e + \boldsymbol{\varepsilon}_p, \quad d\boldsymbol{\varepsilon} = d\boldsymbol{\varepsilon}_e + d\boldsymbol{\varepsilon}_p. \quad (2.50)$$

The constitutive law is thus given

$$\boldsymbol{\sigma} = \mathbb{C} : (\boldsymbol{\varepsilon} - \boldsymbol{\varepsilon}_p). \quad (2.51)$$

Let f be a yield function such that the yield criterion can be expressed by

$$f(\boldsymbol{\sigma}) = 0, \quad (2.52)$$

where α is the hardening variable. Eq. 2.52 defines a surface called yield surface in stress space. A stress state on the yield surface ($f = 0$) means yielding while within the surface ($f < 0$) represents an elastic state. Hence, the yield criterion defines any admissible stress state. The yield criterion takes the form,

$$f = \|\bar{\boldsymbol{\sigma}}\| - \sigma_y(\alpha) = 0, \quad (2.53)$$

where $\bar{\boldsymbol{\sigma}}$ is the effective stress, $\sigma_y(\alpha)$ is the yield stress.

The yield surface may evolve with the plastic deformation, where its shape or location can change. Isotropic hardening characterizes the case where the yield surface is assumed to maintain its shape while its size changes with plastic deformation. The yield criterion is given as

$$f(\boldsymbol{\sigma}, \alpha) = \|\bar{\boldsymbol{\sigma}}\| - (\sigma_y + H\alpha) = 0, \quad (2.54)$$

where H is the hardening modulus. If the yield surface does not change either shape or size but translates its position, this hardening manner is called kinematic hardening. The yield criterion is

$$f(\boldsymbol{\sigma}, \alpha) = \|\bar{\boldsymbol{\sigma}}\| - \sigma_r - \sigma_y = 0, \quad (2.55)$$

where σ_r is called back stress.

According to Drucker's stability postulate, the rate of work done by the stresses during plastic deformation at a point in the material, over a closed cycle involving loading and unloading, is non-negative. It can be expressed as

$$(\boldsymbol{\sigma} - \boldsymbol{\sigma}_0) : d\boldsymbol{\varepsilon}_p \geq 0. \quad (2.56)$$

After materials yield comes plastic flow. The associated flow rule assumes that the increment of the plastic strain is normal to the yield surface at the loading point, i.e.,

$$d\boldsymbol{\varepsilon}_p = d\lambda \frac{\partial f}{\partial \boldsymbol{\sigma}}, \quad \text{or} \quad \dot{\boldsymbol{\varepsilon}}_p = \dot{\lambda} \frac{\partial f}{\partial \boldsymbol{\sigma}}, \quad (2.57)$$

where λ is the plastic multiplier which is non-negative.

In this thesis, the thermo-elasto-plastic constitutive relations are considered in Chapter 4.

2.4 Fracture mechanics

In this section, the basis of classical fracture mechanics including linear elastic fracture mechanics and elasto-plastic fracture mechanics are sketched. The part is referred to the books, e.g., D. Gross [50], T.L. Anderson [51], C.T. Sun [52], et.al.

2.4.1 Griffith's theory

The advent of fracture mechanics is well credited to the pioneering work of Alan Griffith on brittle fracture of glass [53], where he adopted an energy description of the fracture process. He claimed that a crack can form or an existing crack can grow only if the process causes the total energy to decrease or remain constant, and the energy decrease equals the surface energy of the newly created surfaces.

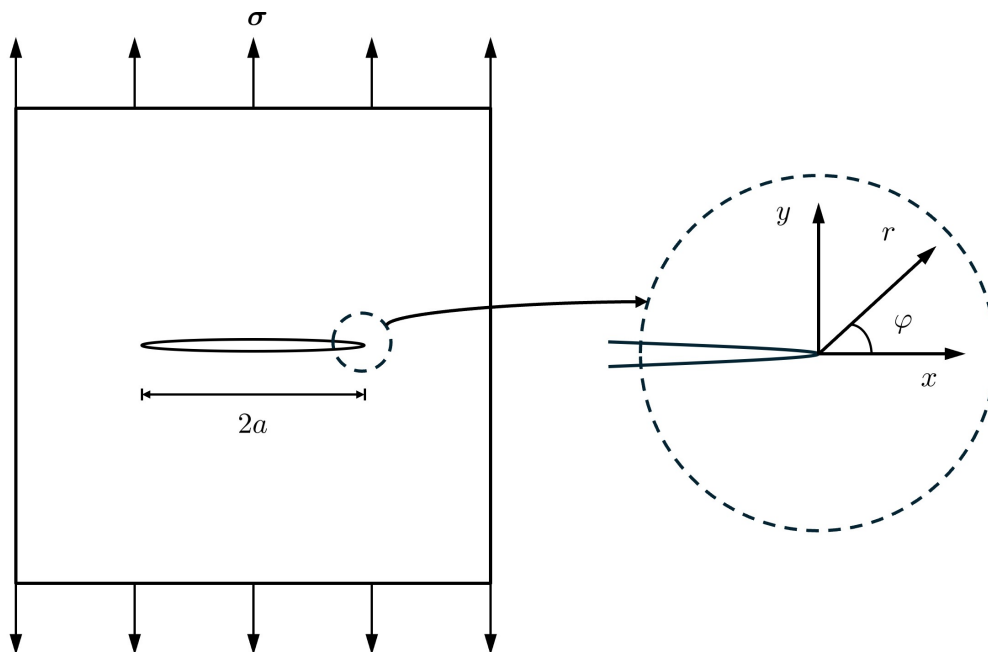


Figure 2.3: An infinite plate with a central crack under tension.

Consider a plate subject to a constant stress σ which contains a predefined crack $2a$ long, as shown in Fig. 2.3. Assume that the plate width $\gg 2a$ and plane stress conditions prevail. For an incremental increase of the crack area dA , the Griffith energy balance can

be expressed as:

$$\frac{d\mathcal{E}}{dA} = \frac{d\Pi}{dA} + \frac{dW}{dA} = 0, \quad (2.58)$$

or

$$-\frac{d\Pi}{dA} = \frac{dW}{dA}, \quad (2.59)$$

where \mathcal{E} denotes the total energy of the system, Π the potential energy and W the work required to create new surfaces. Given the formation of a crack needs to create two surfaces, W is given as

$$\frac{dW}{dA} = 2\gamma_s, \quad (2.60)$$

where γ_s is the specific surface energy of the material.

Irwin [54] further defined energy release rate \mathcal{G} to measure the energy available for an increment of crack growth

$$\mathcal{G} = -\frac{d\Pi}{dA}. \quad (2.61)$$

For an infinite plate with a crack length $2a$ shown in Fig. 2.3, \mathcal{G} is given by

$$\mathcal{G} = \frac{\pi\sigma^2 a}{E}. \quad (2.62)$$

In view of Eq. 2.60, crack grows only if \mathcal{G} reaches a critical value, i.e.,

$$\mathcal{G}_c = \frac{dW}{dA} = 2\gamma_s, \quad (2.63)$$

where \mathcal{G}_c is the critical energy release rate to measure the fracture toughness of the material. The \mathcal{G} criterion for crack growth is written as

$$\mathcal{G} = \mathcal{G}_c. \quad (2.64)$$

2.4.2 Stress intensity factor

Depending on different local loading conditions, there are three types of crack openings, as shown in Fig. 2.4. Mode I, where the load is applied normal to the crack plane, tends to open the crack. Mode II loading denotes in-plane shear and tends to slide the crack surfaces. Mode III refers to out-of-plane shear and tends to tear the crack surfaces apart.

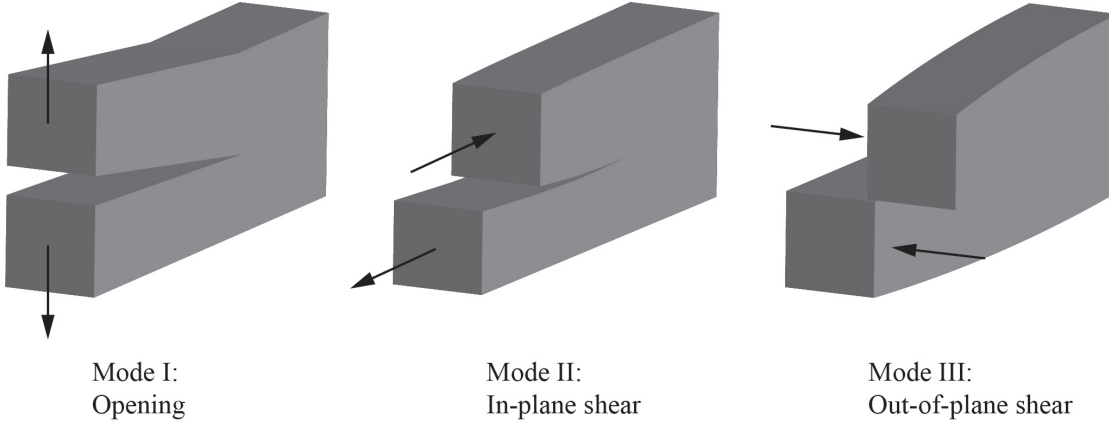


Figure 2.4: Schematic of three crack modes.

For each mode in a linear elastic solid, the stress field at the crack tip in a polar coordinate system $\{r, \varphi\}$ shown in Fig. 2.3 has the $1/\sqrt{r}$ singularity and can be described by

$$\begin{aligned}
 \sigma_{ij}^I(r, \varphi) &= \frac{K_I}{\sqrt{2\pi r}} f_{ij}^I(\varphi), \\
 \sigma_{ij}^{II}(r, \varphi) &= \frac{K_{II}}{\sqrt{2\pi r}} f_{ij}^{II}(\varphi), \\
 \sigma_{ij}^{III}(r, \varphi) &= \frac{K_{III}}{\sqrt{2\pi r}} f_{ij}^{III}(\varphi),
 \end{aligned} \tag{2.65}$$

where K_I, K_{II}, K_{III} denote the stress intensity factor for Mode I, II, and III, respectively [55]. $f_{ij}(\varphi)$ is a function of φ . For a mixed-mode crack, the stress field is superposed

$$\sigma_{ij}(r, \varphi) = \sigma_{ij}^I(r, \varphi) + \sigma_{ij}^{II}(r, \varphi) + \sigma_{ij}^{III}(r, \varphi). \tag{2.66}$$

The stress intensity factor stipulates the magnitude of the stress singularity at the crack tip, i.e., stresses at the crack tip increase proportional to K , and it completely defines the crack-tip fields. The K fracture criterion assumes that the crack propagates when the stress intensity factor reaches a critical value, e.g., for mode I fracture,

$$K_I = K_{Ic}, \tag{2.67}$$

where K_{Ic} is the fracture toughness of the material, which depends on the geometry of the specimen and the loading conditions. K_I for crack in Fig. 2.3 is given by

$$K_I = \sigma\sqrt{\pi a}. \tag{2.68}$$

The stress intensity factor is a local parameter characterizing the stresses near the crack tip, while the energy release rate describes global behavior. Interestingly, for linear elastic materials, they are uniquely related. In view of Eq. 2.62 and Eq. 2.68, the relation between K_I and \mathcal{G} for plane stress is

$$\mathcal{G} = \frac{K_I^2}{E}. \quad (2.69)$$

2.4.3 J-integral

In elasto-plastic fracture mechanics, J -integral is a widely used fracture parameter. Rice [56] presented a contour integral (J -integral) from the potential energy variation with crack extension, and showed that the J -integral equals the energy release rate for nonlinear elastic materials.

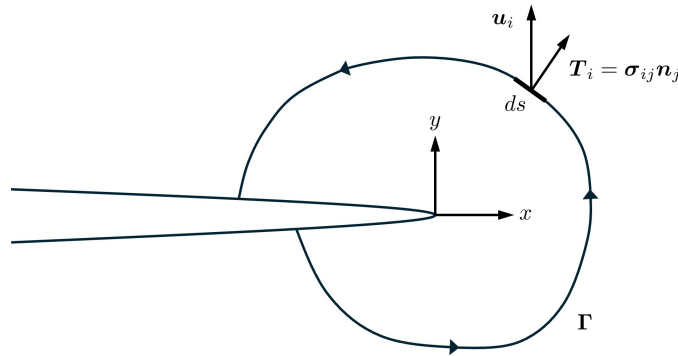


Figure 2.5: Arbitrary contour around the crack tip.

Consider an arbitrary counterclockwise path Γ around the crack tip, as shown in Fig. 2.5. The J integral is expressed as

$$J = \int_{\Gamma} (W dy - T_i \frac{\partial u_i}{\partial x} ds), \quad (2.70)$$

where W denotes the strain energy density, T_i components of the traction vector, ds an length increment on the contour Γ . It showed that the value of J integral is independent of the contour path around the crack tip. Thus, J integral is a path-independent integral. J is a generalized version of the energy release rate. In the case of a linear elastic material,

$$J = \mathcal{G}. \quad (2.71)$$

2.5 Phase-field modeling of fracture

The phase-field modeling of brittle fracture originated from the work by Francfort and Marigo [57], where a phase-field fracture model from the variational approach to brittle fracture by reformulating Griffith's energy criterion [53]. By incorporating a length scale parameter ℓ_0 , the sharp crack interface is smeared by a diffusive crack, where the crack phase-field smoothly changes from the broken state to the unbroken state, as shown in the schematic Fig. 2.6. When ℓ_0 approaches zero, the sharp crack topology is recovered and the energy functional Γ -converges to the original energy functional [58]. Followed by the work of Bourdin et al. [59, 60, 61], Amor et al. [62], and Miehe et al. [63, 64], to name but a few, phase-field fracture model was exploited in a broad spectrum of materials and scenarios, for example, dynamic fracture [65, 66], hydraulic fracture [67, 68], viscoelastic fracture [69], anisotropic fracture [70, 71] and multiphysics fracture problems [72, 73, 74].

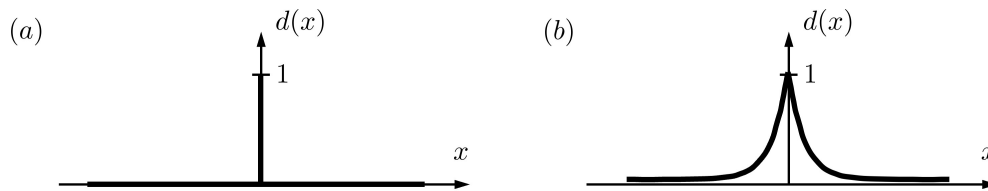


Figure 2.6: (a) Sharp crack and (b) diffusive crack modeling at $x = 0$.

Particularly, phase-field modeling of fracture has been extended to ductile fracture for elastoplastic materials. For brittle materials, in view of Griffith's theory crack growth comes as a result of the competition between bulk elastic energy and crack surface energy. In the case of ductile fracture, however, the dissipation mechanism resulting from plastic deformations comes into play [75]. Correspondingly, the coupling between damage and plasticity plays a crucial role in the fracture process. To date, some phase-field models of ductile fracture have been reported. Notably, the extension from phase-field brittle fracture to ductile fracture was first performed in [76, 77] where the plastic work was introduced to the energy functional in elastoplastic solids. Depending on whether the plastic deformation was additionally included to drive the evolution of crack phase-field, brittle fracture or ductile fracture in elastoplastic solids were investigated, respectively, see the work [78, 79, 80]. The plastic contribution was chosen to be a function of the accumulated plastic strain, the hardening modulus and the material strength. The phase-field ductile fracture was further extended to finite strain, see [81, 82, 83, 84]. Based on the interaction between theoretical models and material response, the phase-field ductile

model can also be classified into uncoupled and coupled categories [85]. In the uncoupled models, the yield surface does not change with damage accumulation. In the coupled approach, however, damage accumulation is incorporated into the yield surface function, which is able to capture the softening behavior experimentally observed. Borden et al. [83] incorporated the damage accumulation into the yield surface function to compensate for the contribution of plastic deformation in the fracture process. Different coupling mechanisms between damage and plasticity have been proposed for various applications. Interestingly, in the work [86], a novel phase-field ductile model was developed based on a characteristic degradation function that couples damage to plasticity. This degradation facilitates fracture where plastic deformation is prominent, in line with the experimental observations. Degradation of fracture toughness with accumulated plastic strain was performed as well, see the works [87, 88, 89]. Recently, Zhang et al. [90] proposed a double-phase-field fracture model for coupled spall and adiabatic shear banding based on a new form of energy decomposition into deviatoric, tensile volumetric and compressive volumetric parts. Matthey et al. [91] developed an anisotropic phase-field fracture model for 3D printed thermoplastics and short fiber reinforced composites.

Phase-field fracture models have also been widely employed to deal with fracture in multiphysics environments, like hydrogen-embrittlement fracture [92, 93], chemical fracture [72, 94] or thermal fracture [95, 96, 97]. When coupled with temperature, the material exhibits thermal softening with the increase of temperature, in addition to the degradation of the damage effect. In particular, for brittle materials like ceramics, concrete or glass, thermal stress induced by non-uniform thermal expansion results in rupture, which is known as thermal shock. This phenomenon has been studied via the phase-field fracture model, see [98, 99]. On the one hand, the thermo-elasto-plastic coupling serves as an additional heat source for the energy balance equation. Ulmer et al. [77] showed temperature rise due to the evolution of plastic strain, see also [79, 100]. On the other hand, the damage influences the heat flux distribution [101, 96], where thermal conductivity is degraded so that no heat flux can pass the fully damaged regions.

The phase-field modeling of brittle fracture originated from the work by [57], where a phase-field model from a variational approach to brittle fracture reformulating Griffith's energy criterion [53] was proposed. They treated the brittle fracture as an energy minimization problem, i.e., the crack area $\Gamma(t)$ is the minimizer of the total energy functional \mathcal{E} ,

$$(\mathbf{u}(t), \Gamma(t)) = \text{Arg}\{\min \mathcal{E}(\mathbf{u}, \Gamma)\}, \quad (2.72)$$

where \mathcal{E} is the summation of internal energy including elastic energy $\Psi_e(\boldsymbol{\varepsilon}(\mathbf{u}))$ and fracture

surface energy Ψ_c , and external potential energy,

$$\mathcal{E}(\mathbf{u}, \Gamma) = \int_{\Omega} \psi dV = \int_{\Omega} \psi_e(\boldsymbol{\varepsilon}(\mathbf{u}), \Gamma) dx + G_c \int_{\Gamma} dA - \int_{\Omega} \mathbf{b} \cdot \mathbf{u} dV - \int_{\partial\Omega} \mathbf{t} \cdot \mathbf{u} dA. \quad (2.73)$$

To numerically implement the model, the regularized form based on elliptic regularization image segmentation [102] was proposed [59]. Therein, the sharp crack interface is diffused within a finite width ℓ_0 in a localized band \mathcal{B} , as shown in Fig. 2.6,

$$\Gamma \approx \Gamma(d) = \int_{\mathcal{B}} \gamma(d, \nabla d) dV, \quad (2.74)$$

where $\gamma(d, \nabla d)$ is the crack surface density function. Therefore, the energy functional takes the form

$$\mathcal{E}(\mathbf{u}, d) = \int_{\Omega} \psi_e(\boldsymbol{\varepsilon}(\mathbf{u}), d) dx + \int_{\mathcal{B}} G_c \gamma(d, \nabla d) dV - \int_{\Omega} \mathbf{b} \cdot \mathbf{u} dV - \int_{\partial\Omega} \mathbf{t} \cdot \mathbf{u} dA. \quad (2.75)$$

The displacement field and crack phase-field (\mathbf{u}, d) are determined by solving the minimization problem as,

$$(\mathbf{u}(t), d(t)) = \text{Arg}\{\min \mathcal{E}(\mathbf{u}, d)\} \quad \text{subject to} \quad \dot{d} \geq 0, \quad d \in [0, 1]. \quad (2.76)$$

Crack geometric function

Consider a diffusive representation of a 1D crack by the following exponential equation [63, 64],

$$d(x) = \exp\left(-\frac{|x|}{\ell_0}\right), \quad (2.77)$$

which fulfills the properties

$$d(x=0) = 1, \quad d(x) \rightarrow 0 : x \rightarrow \pm\infty. \quad (2.78)$$

Fig. 2.7 shows the phase-field profile $d(x)$ for different length scale parameter ℓ_0 . Clearly, Eq. 2.77 is a solution to the ordinary differential equation

$$\frac{1}{\ell_0} d(x) - \ell_0 d''(x) = 0. \quad (2.79)$$

Consistent with the variational approach to fracture, a crack surface functional which yields Eq. 2.79 by minimization can be given as

$$\Gamma(d) = \int \frac{1}{2} \left(\frac{1}{\ell_0} d^2 + \ell_0 d'^2 \right) dx = \int \gamma(d, d') dx. \quad (2.80)$$

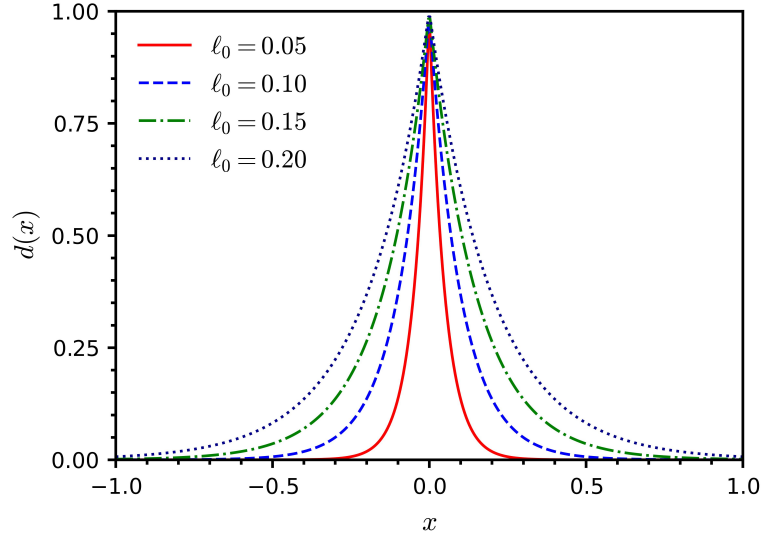


Figure 2.7: Diffusive crack interface with different length scale parameter ℓ_0 .

Therefore, the generalized form of crack surface density is defined as,

$$\gamma(d, \nabla d) = \frac{1}{2} \left(\frac{1}{\ell_0} d^2 + \ell_0 \nabla d \cdot \nabla d \right). \quad (2.81)$$

This leads to a standard phase-field fracture model.

However, there are other models available depending on the definition of crack surface density, which can be generalized as,

$$\gamma(d, \nabla d) = \frac{1}{c_0} \left(\frac{1}{\ell_0} \omega(d) + \ell_0 \nabla d \cdot \nabla d \right), \quad (2.82)$$

where $\alpha(d)$ is the crack geometric function, and $c_0 = 4 \int_0^1 \sqrt{\omega(\beta)} d\beta$ is the scaling parameter. As the name suggests, the crack geometric function defines the profile of the phase-field crack. The commonly used ones are summarized in Table. 2.1 and schematically shown in Fig. 2.8.

Energetic degradation function

To couple the displacement field and the crack phase-field, an energetic degradation function $g(d)$ is added to Eq. 2.75. The evolution of the crack phase-field results in the

Table 2.1: Different crack geometric function $\omega(d)$ and the phase-field profile $d(x)$.

$\omega(d)$	c_0	$d(x)$
d^2	2	$\exp(-\frac{ x }{\ell_0})$
d	$\frac{8}{3}$	$\left(1 - \frac{ x }{2\ell_0}\right)^2$
$2d - d^2$	π	$1 - \sin\left(\frac{ x }{\ell_0}\right)$

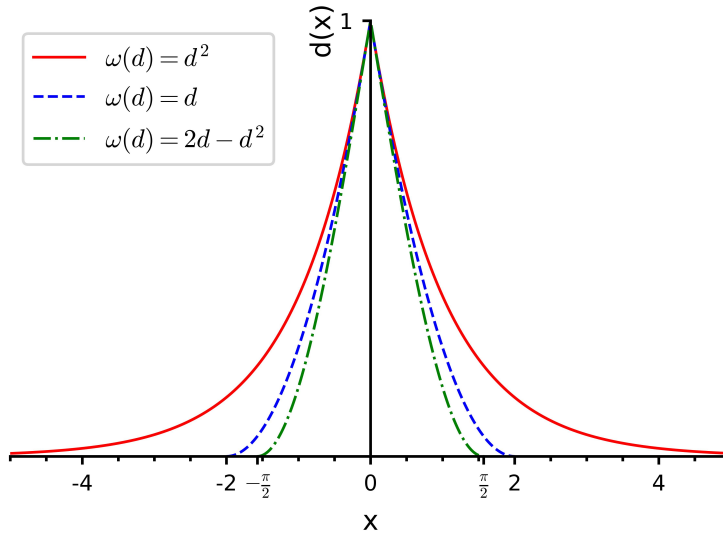


Figure 2.8: Crack phase-field profile $d(x)$ with different crack geometric function $\omega(d)$. For $\omega(d) = d^2$, the crack phase-field has infinite support, and for $\omega(d) = d$ and $\omega(d) = 2d - d^2$, the phase-field has finite support.

degradation of the elastic strain energy. Thus,

$$\mathcal{E}(\mathbf{u}, d) = \int_{\Omega} g(d)\psi_e(\boldsymbol{\varepsilon}(\mathbf{u}))dx + \int_{\mathcal{B}} G_c\gamma(d, \nabla d)dV - \int_{\Omega} \mathbf{b} \cdot \mathbf{u}dV - \int_{\partial\Omega} \mathbf{t} \cdot \mathbf{u}dA. \quad (2.83)$$

The degradation function has the following properties,

$$g(d) \in [0, 1], \quad g(0) = 1, \quad g(1) = 0, \quad g'(d) < 0, \quad g'(1) = 0. \quad (2.84)$$

These conditions ensure $g(d)$ is a monotonically decreasing function, and does not take effect in the intact state ($d = 0$) while degrading elastic energy when the materials are fully cracked ($d = 1$). For the standard phase-field fracture model, i.e., AT1 and AT2 model [59], the degradation function takes the quadratic form as

$$g(d) = (1 - d)^2. \quad (2.85)$$

In [83], a cubic degradation function is proposed to address the nonlinear elastic response prior to yielding in ductile materials,

$$g(d) = (m - 2)(1 - d)^3 + (3 - m)(1 - d)^2, \quad (2.86)$$

where $m > 0$ is a constant determining the slope of $g(d)$ at $d = 0$. [103] proposed a quartic form of $g(d)$ as.

$$g(d) = 4(1 - d)^3 - 3(1 - d)^4. \quad (2.87)$$

The diagram of these functions is shown in Fig. 2.9.

More detailed discussions between different phase-field fracture models are presented in Chapter 3.

Energy decomposition method

The elastic strain energy density in Eq. 2.75 for an undamaged solid,

$$\psi_e(\boldsymbol{\varepsilon}) = \frac{1}{2} \boldsymbol{\varepsilon} : \mathbb{C} : \boldsymbol{\varepsilon} = \frac{1}{2} \lambda \text{tr}^2(\boldsymbol{\varepsilon}) + \mu \text{tr}(\boldsymbol{\varepsilon}^2), \quad (2.88)$$

and the undamaged stress

$$\boldsymbol{\sigma} = \frac{\partial \psi}{\partial \boldsymbol{\varepsilon}} = \lambda \text{tr}(\boldsymbol{\varepsilon}) \mathbf{I} + 2\mu \boldsymbol{\varepsilon}. \quad (2.89)$$

To prevent crack interpenetration and avoid unphysical crack under compression, the tension/compression split is often applied to the total strain energy $\psi_e(\boldsymbol{\varepsilon}(\mathbf{u}))$, where only the tensile/positive part is degraded with crack phase-field. That is,

$$\psi_e(\boldsymbol{\varepsilon}(\mathbf{u})) = g(d)\psi_e^+(\boldsymbol{\varepsilon}(\mathbf{u})) + \psi_e^-(\boldsymbol{\varepsilon}(\mathbf{u})). \quad (2.90)$$

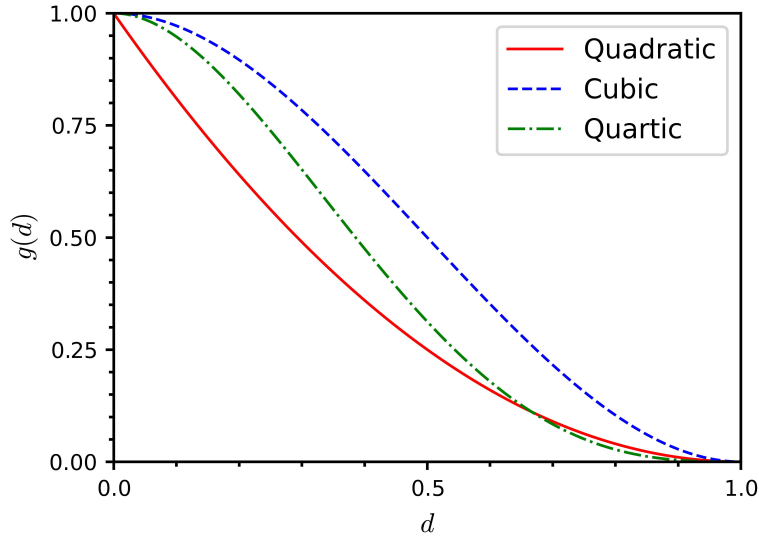


Figure 2.9: Plots of quadratic, cubic and quartic degradation function.

Consequently, the stress is also decomposed,

$$\boldsymbol{\sigma} = g(d)\boldsymbol{\sigma}^+ + \boldsymbol{\sigma}^-. \quad (2.91)$$

Thus, the fracture behavior between tension and compression is distinguished. Two typical approaches to the split are briefly summarized here.

Strain spectral decomposition [63]. The definition is based on the spectral decomposition of the strain tensor,

$$\boldsymbol{\varepsilon} = \boldsymbol{\varepsilon}^+ + \boldsymbol{\varepsilon}^-, \quad \boldsymbol{\varepsilon}^\pm = \sum_{i=1}^3 \langle \varepsilon_i \rangle_\pm \mathbf{n}_i \otimes \mathbf{n}_i. \quad (2.92)$$

where $\varepsilon_{i=1,2,3}$ are the principal strains and $\mathbf{n}_{i=1,2,3}$ the principal strain directions. The bracket operators are defined as $\langle x \rangle_+ = \frac{x + |x|}{2}$, $\langle x \rangle_- = \frac{x - |x|}{2}$, respectively. The positive and negative parts of the energies and stress tensor are defined,

$$\psi_e^+ = \frac{\lambda}{2} \langle \text{tr } \boldsymbol{\varepsilon} \rangle_+^2 + \mu \text{tr } \langle \boldsymbol{\varepsilon} \rangle_+^2, \quad \psi_e^- = \frac{\lambda}{2} \langle \text{tr } \boldsymbol{\varepsilon} \rangle_-^2 + \mu \text{tr } \langle \boldsymbol{\varepsilon} \rangle_-^2, \quad (2.93)$$

$$\boldsymbol{\sigma}^+ = \lambda \langle \text{tr } \boldsymbol{\varepsilon} \rangle_+ \mathbf{I} + 2\mu \langle \boldsymbol{\varepsilon} \rangle_+, \quad \boldsymbol{\sigma}^- = \lambda \langle \text{tr } \boldsymbol{\varepsilon} \rangle_- \mathbf{I} + 2\mu \langle \boldsymbol{\varepsilon} \rangle_-. \quad (2.94)$$

Volumetric-deviatoric decomposition [62]. The elastic energy is additively decomposed into volumetric and deviatoric contributions, and crack only evolves due to positive volumetric (i.e., $\text{tr } \boldsymbol{\varepsilon} \geq 0$) and shear parts.

$$\psi_e^+(\boldsymbol{\varepsilon}) = \frac{1}{2}\kappa\langle\text{tr } \boldsymbol{\varepsilon}\rangle_+^2 + \mu\boldsymbol{\varepsilon}_D : \boldsymbol{\varepsilon}_D, \quad \psi_e^- = \frac{1}{2}\kappa\langle\text{tr } \boldsymbol{\varepsilon}\rangle_-^2. \quad (2.95)$$

Accordingly, the strain is decomposed into volumetric and deviatoric parts,

$$\boldsymbol{\varepsilon} = \boldsymbol{\varepsilon}_V + \boldsymbol{\varepsilon}_D, \quad \boldsymbol{\varepsilon}_V = \frac{1}{3}\text{tr } \boldsymbol{\varepsilon} \mathbf{I}, \quad \boldsymbol{\varepsilon}_D = \boldsymbol{\varepsilon} - \frac{1}{3}\text{tr } \boldsymbol{\varepsilon} \mathbf{I}. \quad (2.96)$$

The stress tensor is thus given as,

$$\boldsymbol{\sigma}^+ = \kappa\langle\text{tr } \boldsymbol{\varepsilon}\rangle_+ \mathbf{I} + 2\mu\boldsymbol{\varepsilon}_D, \quad \boldsymbol{\sigma}^- = \kappa\langle\text{tr } \boldsymbol{\varepsilon}\rangle_- \mathbf{I}, \quad (2.97)$$

where $\kappa = \lambda + \frac{2\mu}{3}$ is the bulk modulus.

Governing equations in strong form

Having defined the energy contribution of ψ_e and ψ_c , the governing equations for the phase-field model can be derived by applying the Euler-Lagrange approach (variational derivative) with respect to the displacement field \mathbf{u} and the crack phase-field d on the total energy functional \mathcal{E} . Note that other approaches, like balance of microforce momentum, can also be used to derive the governing equations.

Considering the general form defined in Eqs. 2.90-2.91, one can obtain the partial differential equations for the displacement field which are basically the same as the balance of linear momentum,

$$\delta_{\mathbf{u}}\psi = \partial_{\mathbf{u}}\psi - \nabla \cdot (\partial_{\nabla\mathbf{u}}\psi) \Rightarrow \begin{cases} \nabla \cdot \boldsymbol{\sigma} + \mathbf{b} = \mathbf{0} & \text{in } \Omega, \\ \boldsymbol{\sigma} \cdot \mathbf{n} = \mathbf{t} & \text{on } \partial\Omega. \end{cases} \quad (2.98)$$

Considering Eq. 2.82, the following equations for the crack field are obtained.

$$\delta_d\psi = \partial_d\psi - \nabla \cdot (\partial_{\nabla d}\psi) \Rightarrow \begin{cases} \frac{G_c}{c_0\ell_0}\omega'(d) - Y - \frac{2G_c\ell_0}{c_0}\nabla^2 d = 0 & \text{in } \Omega, \\ \nabla d \cdot \mathbf{n} = 0 & \text{on } \Gamma, \end{cases} \quad (2.99)$$

where Y is the crack driving force which is defined as,

$$Y = -g'(d)\mathcal{H}. \quad (2.100)$$

To enforce the irreversibility condition of crack upon unloading, the history variable \mathcal{H} is introduced to store the maximum value of the undamaged elastic energy [64], i.e.,

$$\mathcal{H} = \max_t(\psi_e^+(t)). \quad (2.101)$$

The history variable \mathcal{H} ensures that the crack does not heal when the strain energy decreases as the fracture proceeds.

3 Thermo-elastic Phase-field Brittle Fracture at Small Strains

3.1 Thermo-elastic phase-field brittle fracture model

This thesis work focuses on the thermo-elastic coupling and its impact on hot cracking during PBF. To single out the phenomenon, we assume first small deformation, elastostatics and brittle fracture behavior. Such assumptions are applicable to brittle materials, e.g. ceramics or brittle glass. For metallic materials, plasticity and ductile fracture should be addressed. However, it should be noted that in any case, they share some common thermo-mechanical coupling mechanisms, which is the objective of this chapter. After these mechanisms are understood in the linear and brittle scenario, the extension of this framework to the nonlinear deformation and the elastoplastic ductile fracture is presented in Chapter. 4. For thermo-elastic coupled brittle fracture, the primary field variables consist of the displacement field $\mathbf{u}(\mathbf{x}, t)$, the damage field $d(\mathbf{x}, t)$ and the temperature field $\theta(\mathbf{x}, t)$.

3.1.1 Energy dissipation inequality

The second law of thermodynamics, which is expressed in the form of local Clausius-Duhem inequality, is utilized here to derive the thermodynamically consistent constitutive laws of the model. For this thermoelastic coupled problem, the local dissipated energy \mathcal{D} considering the power produced by the micro and macro forces, is given as

$$\mathcal{D} = \boldsymbol{\sigma} : \dot{\boldsymbol{\varepsilon}} + K\dot{d} + \mathbf{H} \cdot \nabla \dot{d} - \rho(\dot{\psi} + \dot{\theta}\eta) - \frac{1}{\theta} \nabla \theta \cdot \mathbf{q} \geq 0. \quad (3.1)$$

Here, $\boldsymbol{\sigma}$ is the Cauchy stress tensor, $\boldsymbol{\varepsilon}$ is the total strain, ψ denotes the Helmholtz free energy, η denotes the entropy, \mathbf{H} is micro-traction on crack surfaces, K is the internal micro-forces, and ρ is the material density.

The Helmholtz free energy ψ is decomposed into elastic energy ψ_e , fracture energy ψ_c and thermal energy ψ_θ parts, as follows

$$\psi = \psi(\boldsymbol{\varepsilon}, d, \nabla d, \theta) = \psi_e(\boldsymbol{\varepsilon}, d, \theta) + \psi_c(d, \nabla d, \theta) + \psi_\theta(\theta). \quad (3.2)$$

The specific energy terms will be explained in the following subsections. For the above equation, the rate of the free energy change is given by

$$\dot{\psi} = \dot{\psi}_e + \dot{\psi}_c + \dot{\psi}_\theta, \quad (3.3)$$

where for the rate of each component we have

$$\begin{cases} \dot{\psi}_e = \frac{\partial \psi_e}{\partial \boldsymbol{\varepsilon}} : \dot{\boldsymbol{\varepsilon}} + \frac{\partial \psi_e}{\partial d} \dot{d} + \frac{\partial \psi_e}{\partial \theta} \dot{\theta} \\ \dot{\psi}_c = \frac{\partial \psi_c}{\partial d} \dot{d} + \frac{\partial \psi_c}{\partial (\nabla d)} \cdot \nabla \dot{d} + \frac{\partial \psi_c}{\partial \theta} \dot{\theta} \\ \dot{\psi}_\theta = \frac{\partial \psi_\theta}{\partial \theta} \dot{\theta} \end{cases} \quad (3.4)$$

Substituting Eq. 3.4 into Eq. 3.3 and regrouping terms, the total free energy rate reads:

$$\dot{\psi} = \frac{\partial \psi_e}{\partial \boldsymbol{\varepsilon}} : \dot{\boldsymbol{\varepsilon}} + \left(\frac{\partial \psi_e}{\partial d} + \frac{\partial \psi_c}{\partial d} \right) \dot{d} + \frac{\partial \psi_c}{\partial (\nabla d)} \cdot \nabla \dot{d} + \left(\frac{\partial \psi_e}{\partial \theta} + \frac{\partial \psi_c}{\partial \theta} + \frac{\partial \psi_\theta}{\partial \theta} \right) \dot{\theta}. \quad (3.5)$$

Therefore, the Clausius-Duhem inequality (Eq. 3.1) is rewritten as

$$\left(\boldsymbol{\sigma} - \rho \frac{\partial \psi}{\partial \boldsymbol{\varepsilon}} \right) : \dot{\boldsymbol{\varepsilon}} + \left(K - \rho \frac{\partial \psi}{\partial d} \right) \dot{d} + \left(\mathbf{H} - \rho \frac{\partial \psi}{\partial (\nabla d)} \right) \cdot \nabla \dot{d} - \left(\rho \eta + \rho \frac{\partial \psi}{\partial \theta} \right) \dot{\theta} - \frac{1}{\theta} \nabla \theta \cdot \mathbf{q} \geq 0. \quad (3.6)$$

Note that here elastostatic and quasi-static fracture are adopted. The inequality in Eq. 3.6 must hold for any arbitrary thermodynamic processes. Hence, the coefficients of the dissipative terms are non-negative while the coefficients of the non-dissipative terms must vanish. Following the Coleman-Noll procedure [104] for a thermodynamically consistent model the thermoelastic laws are

$$\begin{cases} \text{Elastic stress tensor:} & \boldsymbol{\sigma} = \rho \frac{\partial \psi}{\partial \boldsymbol{\varepsilon}} = \rho \frac{\partial \psi_e}{\partial \boldsymbol{\varepsilon}} \\ \text{Micro-traction equation:} & \mathbf{H} = \rho \frac{\partial \psi}{\partial (\nabla d)} = \rho \frac{\partial \psi_c}{\partial (\nabla d)} \\ \text{Internal micro-force equation:} & K = \rho \frac{\partial \psi}{\partial d} = \rho \frac{\partial \psi_e}{\partial d} + \rho \frac{\partial \psi_c}{\partial d} \\ \text{Entropy equation:} & \eta = - \frac{\partial \psi}{\partial \theta} \end{cases} \quad (3.7)$$

Following the above assumptions for the thermodynamic forces, the remaining part of the dissipation inequality reads:

$$-\nabla\theta \cdot \mathbf{q} \geq 0. \quad (3.8)$$

The above relation is also referred to as heat conduction inequality.

3.1.2 Damage informed thermoelasticity

The balance of the linear momentum equation in the tensorial notation and in the absence of the body force reads

$$\nabla \cdot \boldsymbol{\sigma} = \mathbf{0}, \quad (3.9)$$

where $\nabla \cdot$ is the divergence operator. The total strain $\boldsymbol{\varepsilon}$ is additively decomposed into the elastic part and the thermal part:

$$\boldsymbol{\varepsilon} = \boldsymbol{\varepsilon}_e + \boldsymbol{\varepsilon}_\theta = \nabla_s \mathbf{u} := \frac{1}{2} (\nabla \mathbf{u} + \nabla^T \mathbf{u}), \quad (3.10)$$

where $\boldsymbol{\varepsilon}_e$ denotes the elastic strain. The thermal strain $\boldsymbol{\varepsilon}_\theta$ follows a linear expansion law:

$$\boldsymbol{\varepsilon}_\theta = \alpha_t (\theta - \theta_0) \mathbf{I}, \quad (3.11)$$

where α_t is the thermal expansion coefficient, θ_0 is the initial temperature and \mathbf{I} is the second-order identity tensor. The total elastic free energy density for an undamaged body can be expressed as

$$\psi_e = \frac{1}{2} \boldsymbol{\varepsilon}_e : \mathbb{C}^e : \boldsymbol{\varepsilon}_e = \frac{\lambda}{2} (\text{tr } \boldsymbol{\varepsilon}_e)^2 + \mu \text{tr}(\boldsymbol{\varepsilon}_e^2). \quad (3.12)$$

The fourth-order elastic stiffness tensor is denoted by \mathbb{C}^e , and is expressed for isotropic elastic materials in terms of Lamé constant λ and μ as

$$\mathbb{C}^e = \lambda \mathbf{I} \otimes \mathbf{I} + 2\mu \mathbb{I}_S, \quad (3.13)$$

where \mathbb{I}_S is the symmetric fourth-order identity tensor, \otimes denotes the dyadic product of two second-order tensors. In the indicial notation, the symmetric fourth-order identity tensor is expressed $(\mathbb{I}_S)_{ijkl} = \frac{1}{2} (\delta_{ik}\delta_{jl} + \delta_{il}\delta_{jk})$, where δ_{ij} is the Kronecker symbol, and the second-order identity tensor is defined as $I_{ij} = \delta_{ij}$.

To differentiate degradation in tension from compression, we additively decompose elastic strain energy density ψ_e into a positive (tensile) part ψ_e^+ and a negative (compressive) part ψ_e^- :

$$\psi_e = \psi_e^- + f(d)\psi_e^+. \quad (3.14)$$

Here the function $f(d)$ is the so-called degradation function, which has the following properties:

$$f(d) \in [0, 1], f(0) = 1, f(1) = 0; f'(d) < 0, f'(1) = 0. \quad (3.15)$$

The choice of $f(d)$ will be discussed in detail in the following. For the decomposition method, the spectral decomposition of the strain tensor is utilized:

$$\boldsymbol{\varepsilon}_e = \boldsymbol{\varepsilon}_e^+ + \boldsymbol{\varepsilon}_e^-, \quad \boldsymbol{\varepsilon}_e^\pm = \sum_{i=1}^3 \langle \varepsilon_i \rangle^\pm \mathbf{n}_i \otimes \mathbf{n}_i. \quad (3.16)$$

Here, $\varepsilon_{i=1,2,3}$ are the principal strains and $\mathbf{n}_{i=1,2,3}$ denote the principal strain directions. The bracket operators are defined as $\langle x \rangle^+ = \frac{x + |x|}{2}$, $\langle x \rangle^- = \frac{x - |x|}{2}$, respectively. Therefore, for the different parts of the elastic energy we have

$$\psi_e^\pm = \frac{\lambda}{2} (\langle \text{tr } \boldsymbol{\varepsilon}_e \rangle^\pm)^2 + \mu \text{tr } \langle \boldsymbol{\varepsilon}_e \rangle^\pm{}^2. \quad (3.17)$$

In this formulation, only the tensile component contributes to fracture. Similarly, the degraded stress tensor can be derived as

$$\boldsymbol{\sigma} = \frac{\partial \psi_e}{\partial \boldsymbol{\varepsilon}} = f(d) \frac{\partial \psi_e^+}{\partial \boldsymbol{\varepsilon}} + \frac{\partial \psi_e^-}{\partial \boldsymbol{\varepsilon}} = f(d) \boldsymbol{\sigma}^+ + \boldsymbol{\sigma}^-, \quad (3.18)$$

where the stress tensile part $\boldsymbol{\sigma}^+$ and the compressive part $\boldsymbol{\sigma}^-$ are expressed as

$$\boldsymbol{\sigma}^\pm = \lambda \langle \text{tr } \boldsymbol{\varepsilon}_e \rangle^\pm + 2\mu \langle \boldsymbol{\varepsilon}_e \rangle^\pm. \quad (3.19)$$

In this chapter, we explore also the applicability of the very promising cohesive phase-field (CPF) fracture model [105, 106, 66], which characterizes itself by two main features: the threshold for damage initiation and insensitivity to the length scale ℓ_0 . Thereby the degradation function for elastic energy is defined as

$$f(d) = \frac{(1-d)^2}{(1-d)^2 + a_1 d(1 + a_2 d + a_3 d^2)}. \quad (3.20)$$

In the equation above, $a_1 = \frac{4 l_{ch}}{\pi \ell_0}$, $a_2 = -\frac{1}{2}$ and $a_3 = 0$ are selected to represent the cohesive nature of fracture in the process zone. Furthermore, $l_{ch} = \frac{EG_c}{\sigma_u^2}$ is Irwin's length of isotropic materials which measures the size of the fracture process zone. The smaller

this length scale is, the more brittle the material behaves. The parameters a_2 and a_3 are the shape parameters and can be tuned to represent the different softening curves [106].

To prevent cracks from healing when ψ_e^+ decreases, the irreversibility condition is enforced. A history variable \mathcal{H} is introduced [64], which must satisfy the Karush-Kuhn-Tucker (KKT) conditions:

$$\psi_e^+ - \mathcal{H} \leq 0, \quad \dot{\mathcal{H}} \geq 0, \quad \dot{\mathcal{H}} (\psi_e^+ - \mathcal{H}) = 0. \quad (3.21)$$

Thus, the history variable can be written as

$$\mathcal{H} = \max\left\{\max_{t \in [0, \tau]} \psi_e^+(\boldsymbol{\varepsilon}_e, t), \psi_{th}\right\}. \quad (3.22)$$

where the damage threshold ψ_{th} is defined as

$$\psi_{th} = \frac{\sigma_u^2}{2E}. \quad (3.23)$$

where σ_u denotes the material tensile strength and E the Young's modulus. Eq. 3.22 implies that before the onset of any damage the material is characterized by an elastic domain, until ψ_{th} is reached.

3.1.3 Temperature-dependent phase-field fracture model

Consider a cracked solid Ω with an external boundary denoted by $\partial\Omega$ and a crack set Γ , as shown schematically in Fig. 3.1. Starting from Griffith's theory in fracture mechanics, the total fracture energy is given by

$$\Psi_c = \int_{\Gamma} G_c(\theta) dA = \int_{\Omega} G_c(\theta) \gamma(d, \nabla d) dV. \quad (3.24)$$

In the above relation, the surface integral is substituted with a volumetric integral which yields an approximation of the fracture energy [62, 64]. Here, γ is the crack surface density function and is defined as

$$\gamma(d, \nabla d) = \frac{1}{c_0} \left(\frac{1}{\ell_0} \omega(d) + \ell_0 |\nabla d|^2 \right), \quad c_0 = 4 \int_0^1 \sqrt{\omega(\beta)} d\beta. \quad (3.25)$$

In the above equation, the geometric function $\omega(d)$ characterizes the homogeneous evolution of the phase-field crack, which has the properties

$$\omega(d) \in [0, 1], \omega(0) = 0, \omega(1) = 1; \omega'(d) > 0. \quad (3.26)$$

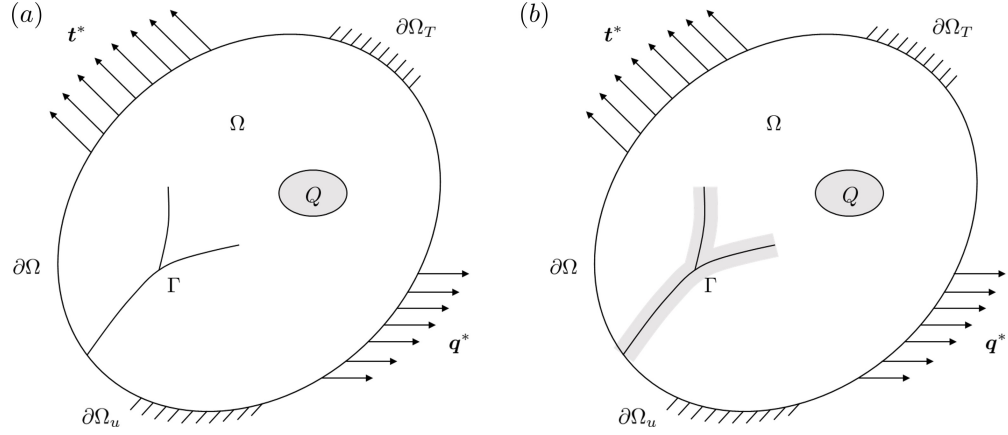


Figure 3.1: (a) Sharp interface and (b) diffusive interface of a crack in a cracked body.

ℓ_0 is the length scale parameter regularizing the sharp crack, which is related to the diffusive crack width, and finally, $c_0 > 0$ is a scaling parameter (see also [64, 106]).

Different choices of the geometric function and degradation function result in different phase-field fracture models. The three most commonly used models are listed in Table 3.1. In the following session, the AT2 model is chosen to compare with the CPF model.

Table 3.1: Different phase-field fracture models.

Models	AT1	AT2	CPF
Features			
$\omega(d)$	d	d^2	$2d - d^2$
c_0	$8/3$	2	π
$f(d)$	$(1 - d)^2$	$(1 - d)^2$	$\frac{(1 - d)^2}{(1 - d)^2 + a_1 d(1 + a_2 d + a_3 d^2)}$

For the AT2 model, the geometric function and degradation function take the quadratic form, with which the predicted material strength shows a strong dependence on ℓ_0 [107]. In the work of Lorentz et al. [107, 105] and Wu et al. [106], a rational degradation function was proposed. It is shown that the material response for this formulation converges to the sharp interface behavior (cohesive zone) as ℓ_0 decreases [108]. The specific form of the length-scale insensitive model is taken in this chapter. One advantage thereby lies in the

fact that it allows to prescribe the ultimate strength σ_u , in addition to the fracture energy value G_c . As a result, the model takes the cohesive nature of the fracture into account and can produce numerical results which converge with respect to the internal length scale parameter. The latter point can be an interesting option for problems containing multiphysics fracture since the influence of the length scale on the results can be omitted.

For quasi-static fracture assuming that micro-inertia is negligible, the micro-force momentum balance equation is given by

$$\nabla \cdot \mathbf{H} = K, \quad (3.27)$$

where \mathbf{H} and K are defined in Eq. 3.7. Employing the micro-force balance equation and using the fracture free energy given in Eq. 3.24, the phase-field governing equation reads:

$$\frac{G_c}{c_0 \ell_0} \omega'(d) - Y - \frac{2G_c \ell_0}{c_0} \nabla^2 d = 0, \quad (3.28)$$

where the driving force of the phase-field is defined as

$$-Y = \frac{\partial \psi_e}{\partial d} = f'(d) \mathcal{H}. \quad (3.29)$$

A simple one-dimensional bar analysis is carried out for clarification of the damage threshold. Consider the situation before the onset of any damage ($d = 0$) and a uniform distribution for the damage variable ($\partial d / \partial x = 0$) in the bar, the governing equation for phase-field crack Eq. 3.28 simplifies to

$$\frac{G_c}{\pi \ell_0} (2 - 2d) + f'(d) \mathcal{H} = 0. \quad (3.30)$$

Thus, damage takes the value one if there is no damage threshold ψ_{th} , which is not physical. However, by introducing ψ_{th} in $\mathcal{H} = \max\{\max_{t \in [0, \tau]} \psi_e^+(\epsilon_e, t), \psi_{th}\}$, one can simplify Eq. 3.28 to

$$\frac{G_c}{\pi \ell_0} (2 - 2d) - a_1 \frac{\sigma_u^2}{2E} = 0. \quad (3.31)$$

With $a_1 = \frac{4 l_{ch}}{\pi \ell_0}$, one can guarantee that the damage value remains zero before the threshold is met. After passing the threshold (i.e. $\max_{t \in [0, \tau]} \psi_e^+(\epsilon_e, t) > \psi_{th}$), the history parameter \mathcal{H} in Eq. 3.28 is replaced by $\psi_e^+(\epsilon_e, t)$ which derives the damage to further develop.

In thermo-mechanical problems, the temperature range can be considerable. Consequently, the variation of G_c with the temperature near the crack tip cannot be ignored, which affects both the initiation of crack onset for a non-isothermal quasi-brittle fracture and the dynamics of crack propagation [109]. Thus the temperature-dependency of G_c needs to be taken into account to capture the crack patterns more accurately. For brittle materials, the dependency of G_c on temperature in this work is based on the description in [110]. For quasi-brittle materials, the experimental relations of G_c with temperature can be found in [111]. In this work, G_c is considered temperature-dependent and takes the form as

$$G_c = G_{c0} \left[1 - b_1 \frac{\theta - \theta_{ref}}{\theta_{max}} + b_2 \left(\frac{\theta - \theta_{ref}}{\theta_{max}} \right)^2 \right]. \quad (3.32)$$

Here, b_1 and b_2 are constant model parameters, θ_{ref} and θ_{max} are the reference temperature and the maximum temperature, respectively, and G_{c0} is the value of G_c at θ_{ref} . In this work, $b_1 = 1.80$, $b_2 = 1.10$, θ_{ref} and θ_{max} are 300 K and 1000 K, respectively.

Note that incorporating temperature-dependent elastic properties like Young's modulus into the model can be more physical. For the current work, the main focus is to investigate the temperature influence on fracture, thus we neglect the temperature-dependent Young's modulus for now. However, the simulation with temperature-dependent elastic properties can readily be done within the developed framework. The readers are also referred to [112] for studies on the temperature-dependent Young's modulus.

Interestingly enough, the temperature-dependency of the material properties affects not only the elastic performance but also the fracture behavior. Notice that in the degradation function in Eq. 3.20, $a_1 = \frac{4 l_{ch}}{\pi \ell_0}$. When E , G_c and σ_u are all treated as temperature-dependent as,

$$E(\theta) = \phi_1(\theta) E_0, \quad G_c(\theta) = \phi_2(\theta) G_{c0}, \quad \sigma_u(\theta) = \phi_3(\theta) \sigma_{u0}, \quad (3.33)$$

where ϕ_i ($i = 1, 2, 3$) is the generic degradation function, then l_{ch} becomes

$$l_{ch} := \frac{E G_c}{\sigma_u^2} = \beta_l(\theta) l_{ch0} \quad \text{with} \quad \beta_l(\theta) = \frac{\phi_1(\theta) \phi_2(\theta)}{\phi_3^2(\theta)}. \quad (3.34)$$

Therefore, a_1 in the degradation function in Eq. 20 becomes

$$a_1(\theta) = \beta_l(\theta) \frac{4 l_{ch0}}{\pi \ell_0}. \quad (3.35)$$

Then, different choices of the degradation function result in a constant or temperature-dependent Irwin's internal length l_{ch} or a_1 , which further affects the fracture behavior of the materials. See also the work of [113] on hydrogen-assisted cracking with hydrogen-dependent material properties.

3.1.4 Damaged informed heat conduction

The energy balance equation, derived from Eq. 2.36 is written as

$$\rho \dot{e} = \boldsymbol{\sigma} : \dot{\boldsymbol{\varepsilon}} + K \dot{d} + H \cdot \nabla \dot{d} - \nabla \cdot \mathbf{q} + Q. \quad (3.36)$$

Given the relation $e = \psi + \theta \eta$ one can write:

$$\dot{e} = \dot{\psi} + \dot{\theta} \eta + \theta \dot{\eta}. \quad (3.37)$$

Considering $\psi = \psi(\boldsymbol{\varepsilon}, d, \nabla d, \theta)$ and the thermodynamic relations obtained in Eq. 3.7, we can obtain

$$\dot{\psi} = \frac{1}{\rho} \left(\boldsymbol{\sigma} : \dot{\boldsymbol{\varepsilon}} + K \dot{d} + H \cdot \nabla \dot{d} - \rho \dot{\theta} \eta \right). \quad (3.38)$$

Substituting Eq. 3.38 into Eq. 3.37, we have

$$\rho \dot{e} = \boldsymbol{\sigma} : \dot{\boldsymbol{\varepsilon}} + K \dot{d} + H \cdot \nabla \dot{d} + \rho \theta \dot{\eta}. \quad (3.39)$$

Comparing Eqs. 3.36 and 3.39, one can conclude

$$\rho \theta \dot{\eta} = -\nabla \cdot \mathbf{q} + Q. \quad (3.40)$$

Note that $\eta(\boldsymbol{\varepsilon}, d, \nabla d, \theta) = -\frac{\partial \psi}{\partial \theta}$. Therefore for the specific entropy rate we have

$$\begin{aligned} \dot{\eta} &= - \left(\frac{\partial^2 \psi}{\partial \theta \partial \boldsymbol{\varepsilon}} : \dot{\boldsymbol{\varepsilon}} + \frac{\partial^2 \psi}{\partial \theta \partial d} \dot{d} + \frac{\partial^2 \psi}{\partial \theta \partial (\nabla d)} \cdot \nabla \dot{d} + \frac{\partial^2 \psi}{\partial \theta^2} \dot{\theta} \right) \\ &= -\frac{1}{\rho} \left(\frac{\partial \boldsymbol{\sigma}}{\partial \theta} : \dot{\boldsymbol{\varepsilon}} + \frac{\partial K}{\partial \theta} \dot{d} + \frac{\partial H}{\partial \theta} \cdot \nabla \dot{d} - \rho \frac{\partial \eta}{\partial \theta} \dot{\theta} \right). \end{aligned} \quad (3.41)$$

Next, we consider the Fourier's law by means of which the inequality relation in Eq. 3.8 is automatically satisfied:

$$\mathbf{q} = -k(d) \nabla \theta. \quad (3.42)$$

Here $k(d)$ is the degraded thermal conductivity affected by the phase-field d and it is expressed as

$$k(d) = g(d) k_0. \quad (3.43)$$

In the above relation, k_0 is the thermal conductivity of the undamaged material, and $g(d)$ is a thermal degradation function which ensures that no heat flux exists across the crack. Though there are other forms of thermal degradation proposed in the work of [101, 96], an isotropic conductivity degradation $g(d) = (1 - d)^2 + \xi$ is adopted here, where ξ is

a small number for numerical and physical purposes. Substituting Eq. 3.41 into Eq. 3.40 we have

$$-\theta \left(\frac{\partial \boldsymbol{\sigma}}{\partial \theta} : \dot{\boldsymbol{\varepsilon}} + \frac{\partial K}{\partial \theta} \dot{d} + \frac{\partial H}{\partial \theta} \cdot \nabla \dot{d} - \rho \frac{\partial \eta}{\partial \theta} \dot{\theta} \right) = k(d) \nabla^2 \theta + Q. \quad (3.44)$$

By introducing the specific heat defined as

$$c = \theta \frac{\partial \eta}{\partial \theta}, \quad (3.45)$$

the complete form of the heat equation reads:

$$\rho c \dot{\theta} = k(d) \nabla^2 \theta + \theta \left(\frac{\partial \boldsymbol{\sigma}}{\partial \theta} : \dot{\boldsymbol{\varepsilon}} + \frac{\partial K}{\partial \theta} \dot{d} + \frac{\partial H}{\partial \theta} \cdot \nabla \dot{d} \right) + Q. \quad (3.46)$$

Eq. 3.46 can degenerate to the conventional heat conduction equation for heat conduction with an internal heat source. At this point, we adopt the formulation for the quasi-static crack propagation where the transient coupling terms $\dot{\boldsymbol{\varepsilon}}$ and \dot{d} vanish. Thereby, in the current implementation, the heat equation takes the form as

$$\rho c \dot{\theta} = k(d) \nabla^2 \theta + Q. \quad (3.47)$$

3.1.5 Summary of governing equations

With the energy terms of the multiphysics problem being defined, the strong form of the quasi-static fracture problem, following the balance laws and constitutive relations described above, can be summarized as follows

$$\text{Momentum balance: } \nabla \cdot \boldsymbol{\sigma} = 0 \quad (3.48a)$$

$$\text{Phase-field equation: } \frac{G_c}{c_0 \ell_0} \omega'(d) - \frac{2G_c \ell_0}{c_0} \nabla^2 d - Y = 0 \quad (3.48b)$$

$$\text{Heat equation: } \rho c \dot{\theta} = k(d) \nabla^2 \theta + Q \quad (3.48c)$$

with the Dirichlet boundary conditions and the Neumann boundary conditions

$$\begin{cases} \mathbf{u}(\mathbf{x}, t) = \mathbf{u}^*(\mathbf{x}, t) & \mathbf{x} \in \partial\Omega_{\mathbf{u}}, \\ d(\mathbf{x}, t) = d^*(\mathbf{x}, t) & \mathbf{x} \in \Gamma, \\ \theta(\mathbf{x}, t) = \theta^*(\mathbf{x}, t) & \mathbf{x} \in \partial\Omega_{\theta}. \end{cases} \quad (3.49)$$

$$\begin{cases} \boldsymbol{\sigma} \cdot \mathbf{n} = \mathbf{t}^* & \mathbf{x} \in \partial\Omega_{\mathbf{t}}, \\ \mathbf{q} \cdot \mathbf{n} = q^* & \mathbf{x} \in \partial\Omega_{\mathbf{q}}. \end{cases} \quad (3.50)$$

Here, the boundary is partitioned into Dirichlet and Neumann-type conditions. Specifically, the boundary is split as follows

$$\partial\Omega = \partial\Omega_{\mathbf{u}} \cup \partial\Omega_t, \quad \partial\Omega_{\mathbf{u}} \cap \partial\Omega_t = \emptyset, \quad \partial\Omega = \partial\Omega_\theta \cup \partial\Omega_q, \quad \partial\Omega_\theta \cap \partial\Omega_q = \emptyset, \quad (3.51)$$

where $\partial\Omega^{\mathbf{u}}$, $\partial\Omega^t$, $\partial\Omega^\theta$ and $\partial\Omega^q$ are the parts of boundary on which the prescribed displacement \mathbf{u}^* , traction \mathbf{t}^* , temperature θ^* and heat flux \mathbf{q}^* are imposed, respectively. Lastly, the governing equations are supplemented with the following initial conditions. The initial state of the system is considered to be undeformed, undamaged, and unstressed with temperature $\theta_0(\mathbf{x})$.

$$\begin{cases} \mathbf{u}(\mathbf{x}, 0) = \mathbf{0} & \mathbf{x} \in \Omega, \\ d(\mathbf{x}, 0) = 0 & \mathbf{x} \in \Omega, \\ \theta(\mathbf{x}, 0) = \theta_0(\mathbf{x}) & \mathbf{x} \in \Omega. \end{cases} \quad (3.52)$$

3.2 Numerical implementation

3.2.1 Finite element discretization

This section presents the finite element implementation of the model. The weak form is constructed by multiplying the equations in Eq. 3.48(a-c) by a corresponding arbitrary test function and integrating them over the domain of the problem. With integration by parts, the corresponding weak forms are:

$$\int_{\Omega} \boldsymbol{\sigma} : \nabla \delta_u dV - \int_{\Omega_t} \mathbf{t}^* \delta_u dS = 0, \quad (3.53a)$$

$$\int_{\Omega} \frac{G_c}{\ell_0 c_0} \omega'(d) \delta_d dV + \int_{\Omega} \frac{2G_c \ell_0}{c_0} \nabla d \cdot \nabla \delta_d dV + \int_{\Omega} g'(d) \mathcal{H} \delta_d dV = 0, \quad (3.53b)$$

$$\int_{\Omega} k \nabla \theta \cdot \nabla \delta_\theta dV - \int_{\Omega_q} k \nabla \theta \delta_\theta dS + \int_{\Omega} \rho c \dot{\theta} \delta_\theta dV - \int_{\Omega} Q \delta_\theta dV = 0. \quad (3.53c)$$

Utilizing the standard finite element method, the displacement field \mathbf{u} , the phase-field d and the temperature field θ , as well as their first spatial derivatives, are approximated as

$$\begin{cases} \mathbf{u} = \sum N_u^i u_i = \mathbf{N}_u \mathbf{u}_e, & \boldsymbol{\varepsilon} = \sum B_u^i u_i = \mathbf{B}_u \mathbf{u}_e, \\ d = \sum N_d^i d_i = \mathbf{N}_d \mathbf{d}_e, & \nabla d = \sum B_d^i d_i = \mathbf{B}_d \mathbf{d}_e, \\ \theta = \sum N_\theta^i \theta_i = \mathbf{N}_\theta \boldsymbol{\theta}_e, & \nabla \theta = \sum B_\theta^i \theta_i = \mathbf{B}_\theta \boldsymbol{\theta}_e. \end{cases} \quad (3.54)$$

Here, u_i , d_i and θ_i are the nodal values of the displacement, damage and temperature fields of node i of element e , respectively. N_u , N_d , N_θ and B_u , B_d , B_θ denote the shape

functions and their derivatives for the displacement, damage field and temperature, respectively. N_u, N_d, N_θ and B_u, B_d, B_θ are the corresponding shape function matrices and derivatives. For a quadrilateral 2D element they are written as

$$\mathbf{N}_u = \begin{bmatrix} N_1 & 0 & \cdots & N_4 & 0 \\ 0 & N_1 & \cdots & 0 & N_4 \end{bmatrix}, \quad \mathbf{B}_u = \begin{bmatrix} N_{1,x} & 0 & \cdots & N_{4,x} & 0 \\ 0 & N_{1,y} & \cdots & 0 & N_{4,y} \\ N_{1,y} & N_{1,x} & \cdots & N_{4,y} & N_{4,x} \end{bmatrix}, \quad (3.55)$$

$$\mathbf{N}_d = [N_1 \quad \cdots \quad N_4], \quad \mathbf{B}_d = \begin{bmatrix} N_{1,x} & \cdots & N_{4,x} \\ N_{1,y} & \cdots & N_{4,y} \end{bmatrix}, \quad (3.56)$$

$$\mathbf{N}_\theta = [N_1 \quad \cdots \quad N_4], \quad \mathbf{B}_\theta = \begin{bmatrix} N_{1,x} & \cdots & N_{4,x} \\ N_{1,y} & \cdots & N_{4,y} \end{bmatrix}. \quad (3.57)$$

With the above finite element discretization, we obtain the following equations for the residuals of different fields:

$$\mathbf{r}_u = \int_{\Omega} [\mathbf{B}_u]^T \boldsymbol{\sigma} dV - \int_{\Omega_t} [\mathbf{N}_u]^T \mathbf{t}^* dS, \quad (3.58a)$$

$$\mathbf{r}_d = \int_{\Omega} \frac{G_c}{\ell_0 c_0} \omega'(d) [\mathbf{N}_d]^T \mathbf{N}_d dV + \int_{\Omega} \frac{2G_c \ell_0}{c_0} [\mathbf{B}_d]^T \mathbf{B}_d dV + \int_{\Omega} g'(d) [\mathbf{N}_d]^T \mathcal{H} dV, \quad (3.58b)$$

$$\mathbf{r}_\theta = \int_{\Omega} [\mathbf{B}_\theta]^T k \mathbf{B}_\theta dV - \int_{\Omega_q} [\mathbf{B}_\theta]^T k \mathbf{N}_\theta dS + \int_{\Omega} \rho c \dot{\theta} [\mathbf{N}_\theta]^T dV - \int_{\Omega} [\mathbf{N}_\theta]^T Q dV. \quad (3.58c)$$

3.2.2 Staggered solution scheme

In general, the energy functional of the thermal fracture problem is non-convex with respect to its variables when all the field variables are considered simultaneously. Therefore it is challenging to solve all the unknown variables at the same time utilizing the conventional Newton-Raphson method. However, the problem is convex with respect to the variables \mathbf{u} and d separately when the other is fixed. The approach which is also known as the staggered minimization algorithm improves the convergence of the numerical solver.

In this work, the thermo-elastic coupled problem is first solved in a monolithic way with a fixed crack field. Then, the phase-field fracture problem is solved with the updated displacement and temperature values. For the $(n + 1)$ th time step, first, we solve for the nodal displacements and temperature fields from the coupled thermo-elastic problem. At this point, the crack is fixed as d_n obtained in the previous time step n . Therefore, we

first solve for

$$\begin{cases} \mathbf{r}_{u,n+1} = \int_{\Omega} [\mathbf{B}_u]^T \boldsymbol{\sigma} dV - \int_{\Omega_t} [\mathbf{N}_u]^T \mathbf{t}^* dS, \\ \mathbf{r}_{\theta,n+1} = \int_{\Omega} [\mathbf{B}_{\theta}]^T k \mathbf{B}_{\theta} dV - \int_{\Omega_q} [\mathbf{B}_{\theta}]^T k \mathbf{N}_{\theta} dS + \int_{\Omega} \rho c \dot{\theta} [\mathbf{N}_{\theta}]^T dV - \int_{\Omega} [\mathbf{N}_{\theta}]^T Q dV, \end{cases} \quad (3.59)$$

where $\boldsymbol{\sigma} = \boldsymbol{\sigma}(\mathbf{u}_{n+1}, d_n, \theta_{n+1})$, $k = k(d_n)$ and $G_c = G_c(\theta_{n+1})$. This standard thermo-elastic problem can be solved by the Newton method, with the letter i denoting the iteration number.

$$\begin{bmatrix} \mathbf{K}_{uu,n+1}^{(i+1)} & \mathbf{K}_{u\theta,n+1}^{(i+1)} \\ \mathbf{K}_{\theta u,n+1}^{(i+1)} & \mathbf{K}_{\theta\theta,n+1}^{(i+1)} \end{bmatrix} \begin{bmatrix} \mathbf{u}_{n+1}^{(i+1)} - \mathbf{u}_{n+1}^{(i)} \\ \theta_{n+1}^{(i+1)} - \theta_{n+1}^{(i)} \end{bmatrix} = \begin{bmatrix} \mathbf{R}_{u,n+1}^{(i+1)} \\ \mathbf{R}_{\theta,n+1}^{(i+1)} \end{bmatrix}. \quad (3.60)$$

Next, we solve the nodal unknowns for the fracture problem with the updated nodal displacement and nodal temperature $\mathbf{u}_{n+1}^{(i+1)}, \theta_{n+1}^{(i+1)}$ i.e.,

$$\mathbf{r}_{d,n+1} = \int_{\Omega} \frac{G_c}{\ell_0 c_0} \omega'(d) [\mathbf{N}_d]^T \mathbf{N}_d dV + \int_{\Omega} \frac{2G_c \ell_0}{c_0} [\mathbf{B}_d]^T \mathbf{B}_d dV + \int_{\Omega} g'(d) [\mathbf{N}_d]^T \mathcal{H} dV. \quad (3.61)$$

The linearization of the above relation yields

$$\mathbf{K}_{dd,n+1}^{(i+1)} (d_{n+1}^{(i+1)} - d_{n+1}^{(i)}) = \mathbf{R}_{d,n+1}^{(i+1)}. \quad (3.62)$$

In Eq. 3.60 and 3.62, \mathbf{R}_u , \mathbf{R}_{θ} and \mathbf{R}_d denote the assembled global residual vectors for each variable; \mathbf{K}_{uu} , $\mathbf{K}_{\theta\theta}$, $\mathbf{K}_{u\theta}$ and \mathbf{K}_{dd} denote the assembled global stiffness matrix, respectively. The total assembled global residual is denoted by $\mathbf{R} = [\mathbf{R}_u; \mathbf{R}_{\theta}; \mathbf{R}_d]$.

Based on the above explanations, the algorithm for the phase-field thermal fracture model is summarized in Algorithm 1.

Algorithm 1 Staggered minimization algorithm at time interval $[t_n, t_{n+1}]$

- 1: Inputs: solutions of temperature field θ_n , displacement field \mathbf{u}_n , crack phase-field d_n at former time step t_n .
 - 2: Outputs: temperature field θ_{n+1} , displacement field \mathbf{u}_{n+1} , crack field d_{n+1} at current time step t_{n+1} .
 - 3: Set $i = 0$, Tolerance = $1e-8$.
 - 4: Set $\theta_{n+1}^{(0)} \leftarrow \theta_n$, $\mathbf{u}_{n+1}^{(0)} \leftarrow \mathbf{u}_n$, $d_{n+1}^{(0)} \leftarrow d_n$
 - 5: **repeat**
 - 6: Compute $\theta_{n+1}^{(i+1)}$, $\mathbf{u}_{n+1}^{(i+1)}$ and fix $d_{n+1}^{(i)}$
 - 7: Compute $d_{n+1}^{(i+1)}$ and fix $\theta_{n+1}^{(i+1)}$, $\mathbf{u}_{n+1}^{(i+1)}$
 - 8: subject to irreversibility constraint $d_{n+1}^{(i+1)} \geq d_n$
 - 9: $i \leftarrow i+1$
 - 10: **until** $|\mathbf{R}_{n+1}^{(i+1)} - \mathbf{R}_{n+1}^{(i)}| \leq \text{Tolerance}$
 - 11: Update solutions $\theta_{n+1} \leftarrow \theta_{n+1}^{(i+1)}$, $\mathbf{u}_{n+1} \leftarrow \mathbf{u}_{n+1}^{(i+1)}$, and $d_{n+1} \leftarrow d_{n+1}^{(i+1)}$
-

The model is numerically implemented by the Finite Element Method within the framework of Multiphysics Object-Oriented Simulation Environment (MOOSE) [114]. It is worth noting that the Automatic Differentiation (AD) capabilities in MOOSE are utilized here, which is a symbolic differentiation method [115]. It applies the chain rule and propagates derivatives to elementary operations at every step. AD offers a very accurate Jacobian at a relatively small overhead cost. Thus, there is no need to compute Jacobian by hand which is arduous and prone to errors in the context of multiphysics problems. Therefore, it helps shift the burden of computing the derivatives of the complex known expressions for the free energies from the user to the software. MOOSE employs the DualNumber class from the MetaPhysicL package to enable forward-mode AD capabilities [116]. The staggered solution scheme is implemented by the MultiApp system in MOOSE. For transient problems, the TransientMultiApp is utilized, which performs coupled simulations with sub-applications that progress in time and iterate with the main application. Within each iteration, the applications are required to transfer data from and to the others. In this case, the main application computes θ and \mathbf{u} in a monolithic way, then transfers the results to the sub-application which calculates d . After d is updated, it's transferred back to the main application for further steps.

3.3 Single-edge notched tension test

We start by investigating the single-edge notched tension test, which has become canonical in the phase-field models for fracture. Consider a square plate of $1\text{mm} \times 1\text{mm}$ with an initially horizontal edge crack extending to the middle of the specimen. The geometry and boundary conditions are shown in Fig. 3.2(a). The bottom edge is fixed while a vertical displacement is applied to the top edge. To include the temperature field in the thermal fracture model, the initial temperature of the plate is set as 300 K. The outer boundaries are treated as adiabatic. The domain is discretized into the unstructured mesh, and the mesh is refined along the anticipated crack path to ensure the fracture phase-field variable in the localized band is well resolved. This point is essential to accurately capture the evolution of the crack phase-field in the simulations.

Table 3.2: Material parameters for single edge notched tension test

E (GPa)	ν	G_{c0} (J/m ²)	σ_u (MPa)	ρ (kg/m ³)	k (W/mK)	c_p (J/kgK)	α
340	0.22	42.47	180	2450	300	0.775	$8e-6$

To compare the difference between the AT2 model and the CPF model and the ℓ_0 insensitivity of the latter model, three different length scale parameters $\ell_0 = 0.010$ mm, 0.015 mm, and 0.020 mm are used, both for the AT2 model and the CPF model. The refined mesh size is set to be 0.005 mm. Thus the ratio of length scale to mesh size is 2, 3, and 4 respectively. The fixed time step is 0.010 ms and the total simulation time is 1.0 ms. The material properties used for these examples are listed in Table. 3.2.

The AT2 model and CPF model are compared here to check the convergence of the results concerning the length scale parameter ℓ_0 . In Fig. 3.2(a), the crack patterns calculated using the CPF model and AT2 model with $\ell_0 = 0.020$ mm are shown, respectively. As ℓ_0 controls the width of the diffusive zone, with the increase of ℓ_0 the damaged zone becomes wider. Fig. 3.2(a) also shows that the damaged zones of the CPF model are more compact compared with the AT2 model, as the half bandwidth of the former model is $\pi\ell_0/2$ while for the latter is infinity [106, 117]. This result also verifies there is a threshold of damage initiation for the CPF model. The corresponding load versus displacement curves are plotted in Fig. 3.2(b). The results show that the global responses of the CPF model are almost independent of ℓ_0 while for the AT2 model the peak load decreases with the increase of the length scale. The former observation confirms the insensitivity of the results from the CPF model concerning the length scale parameter under thermo-mechanical conditions.

We further study the effect of thermal loading on crack patterns and temperature

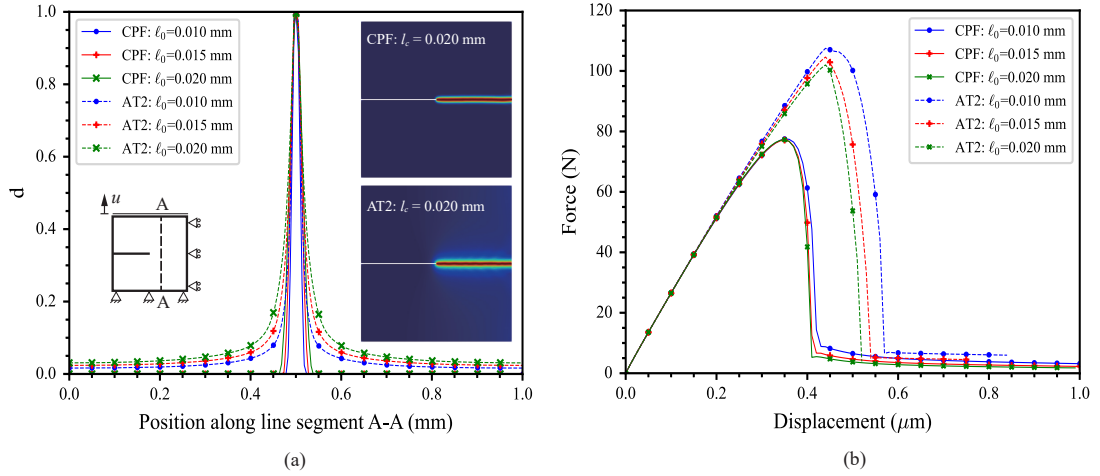


Figure 3.2: Results of single-edge notched tension test under thermo-mechanical boundary conditions. (a) Comparison of damage level and (b) Reaction force-displacement curve of the AT2 model and the CPF model with different l_0 .

distributions. Three cases are considered here. In case 1, we keep the temperature of the bottom and the top edges at 300 K. In case 2, we cool down the top edge from the beginning to 0.25 ms at a ratio of $1.0e5$ K/s to 275 K and then keep the temperature constant. Finally, in case 3, we heat up the top edge with the same speed to 325 K and then keep it constant. Other settings of the simulations are the same as before. The comparisons of these results are shown in Fig. 3.3. It is observed that compared with case 1 where the constant thermal loading is included and the crack propagates horizontally to the right edge of the specimen, the crack develops slightly downwards when the temperature is increased on the top edge, while upwards when the temperature is decreased.

Take case 3 for illustration here. Fig. 3.3(a) and (b) show the crack patterns of case 3 with degraded and constant thermal conductivity. The reaction force-displacement curves are plotted in Fig. 3.3(e). From the curves, it is apparent the onset of the crack is delayed when the top edge is heated up compared with the fixed temperature while the crack propagates earlier when cooling down the top edge. When the temperature goes up, the specimen expands and the thermal strain is positive, which leads to a smaller elastic strain with fixed displacement and a smaller driving force for crack propagation compared with a uniform temperature field.

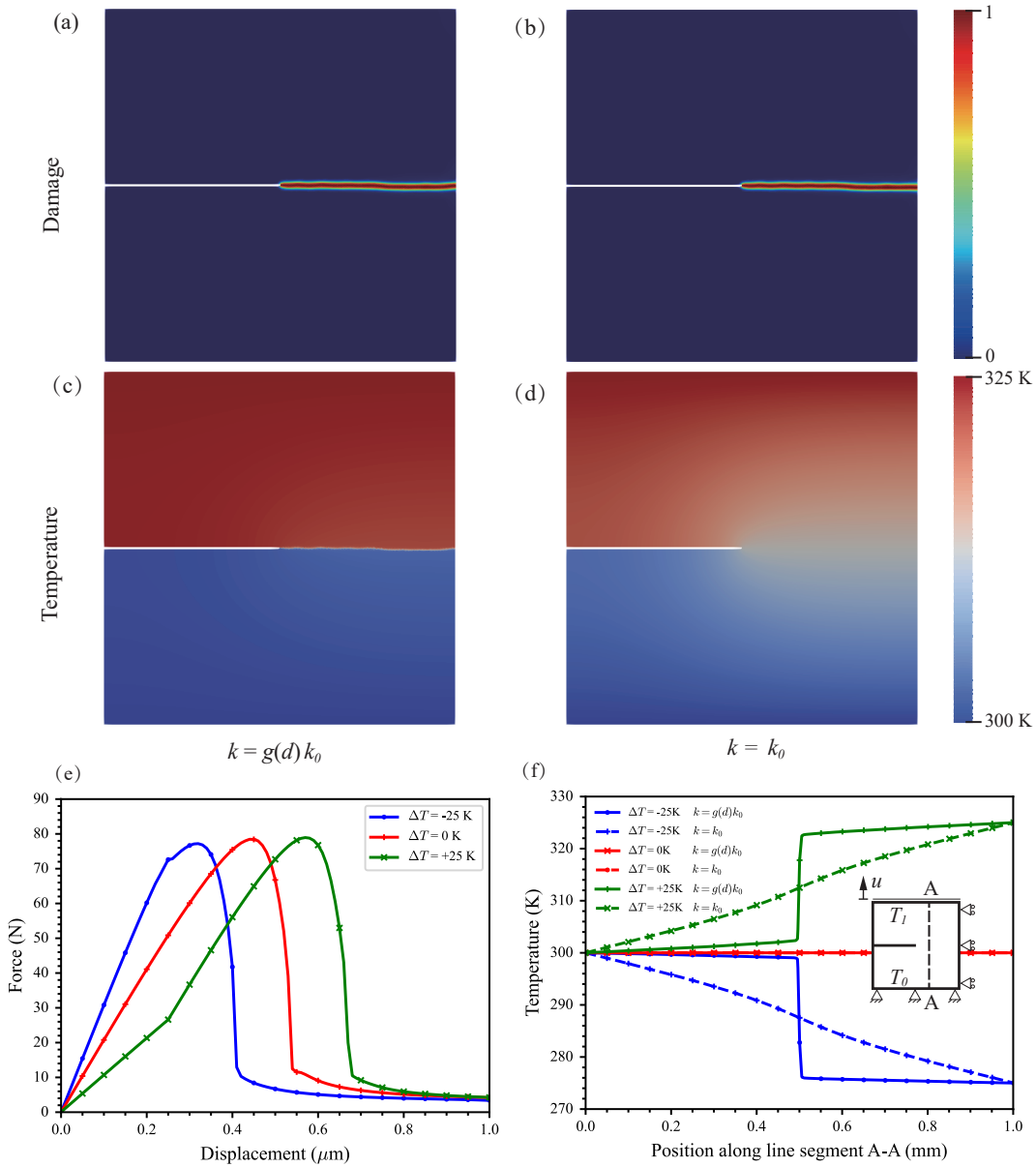


Figure 3.3: Single-edge notched tension test under thermo-mechanical loading. Crack patterns and temperature profiles for case 3 with (a and c) and without (b and d) thermal conductivity degradation. (e) Reaction force-displacement curves for different thermal loading and (f) Temperature profiles along A-A for different thermal loading with and without thermal conductivity degradation.

In case 3, the temperature of the top region is higher than that of the bottom region, thus G_c is lower at the top. Though G_c is temperature-dependent, its value does not change much in the temperature range of interest [275 K, 325 K], according to Eq. 3.32. At the same time, the thermal expansion at the top also takes effect during the tensile test, and it in fact takes a dominant role. The phenomenon can also be demonstrated in case 2 ($\Delta\theta = -25$ K) as well. Compared with the uniform temperature field ($\Delta\theta = 0$ K) and the crack propagates horizontally, in case 2 we cool down the top edge and the crack propagates slightly upwards, just contrary to case 3 ($\Delta\theta = +25$ K). These results are also seen in the work of [118].

Meanwhile, according to Griffith's theory [53], the fracture strength of material for plane strain problem is defined as

$$\sigma_f = \sqrt{\frac{2E\gamma_s}{\pi l(1-\nu^2)}} = \sqrt{\frac{EG_c}{\pi l(1-\nu^2)}}, \quad (3.63)$$

where γ_s is the fracture surface energy density. Therefore, the decreasing G_c also leads to the decreasing σ_f for case 3. However, the value changes very slightly and cannot compensate for the influence of thermal strain. Therefore, a larger displacement is needed for the onset of crack initiation. While for case 2 with decreasing temperature, the contraction of the specimen results in negative thermal strain. Correspondingly, the elastic strain and the driving force are greater. Therefore the onset of the crack only needs a smaller displacement, despite that G_c and σ_f increase slightly.

Note that the thermal conductivity is degraded as the crack develops. This effect is considered to avoid non-physical heat transfer happening in the fully-cracked region. The comparisons of the temperature profile of case 3 with degraded and constant thermal conductivity are depicted in Fig. 3.3(c) and (d). It shows that when there is no thermal conductivity degradation with the phase-field crack, the temperature field changes smoothly even in the cracked regions. However, as the thermal conductivity is degraded with cracks, the temperature is not continuous across the cracked regions. The phenomenon can also be observed in Fig. 3.3(f), the temperature profiles along the line segment A-A at the final time step for the three cases are depicted. Interestingly enough, when the thermal conductivity is degraded with the phase-field crack, a sharp temperature jump is observed for case 2 and case 3. For case 1, because the temperature at the top edge and bottom edge are both fixed at 300K, the temperature does not change. In contrast, the smooth temperature field change is observed when no thermal conductivity degradation is considered.

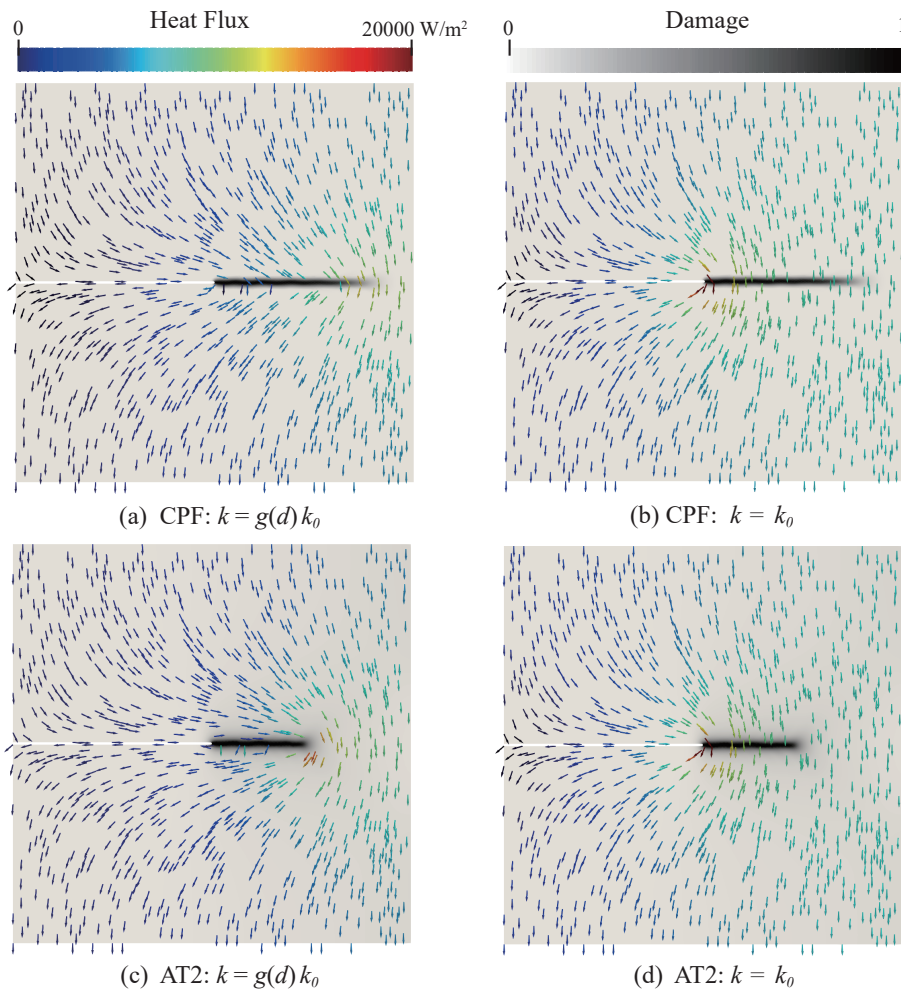


Figure 3.4: Snapshots of heat flux for cases with degraded (left column) and constant (right column) thermal conductivity for CPF model (a and b) and AT2 model (c and d).

To further illustrate the influence of the degraded thermal conductivity, Fig. 3.4 depicts the heat flux magnitudes and directions for case 3 with degraded and constant thermal conductivity. The initial heat flux directions are identical for the two scenarios. Because of the temperature gradient between the top edge and the bottom edge, heat flux goes from high-temperature regions to lower-temperature regions. In the right half of the specimen

containing no crack, the heat flux goes almost vertically downwards and perpendicular to the pre-crack direction, while for the other half the heat flux tries to bypass the notch tip. However, with different thermal conductivity being considered, the heat flux becomes different when the crack propagates forward, as shown in Fig. 3.4(a) and (b). It is observed that when thermal conductivity is degraded with the crack (see Eq. 3.43), the heat flux directions change at the crack tip while it is still perpendicular to the crack for the constant thermal conductivity case. Because of the cohesive nature of the CPF model, the damage level at the crack tip is more diffusive. And also the residual conductivity still exists for the parameter ξ , so the thermal conductivity is not fully degraded. Thus there is still some residual heat flux crossing the crack tip. This degradation phenomenon is also observed when the AT2 model is used, see Fig. 3.4(c) and (d). When the degraded thermal conductivity is considered, its value approaches zero as soon as the crack is fully developed, meaning the material is not continuous physically. Thus there is no heat transfer happening in the fully cracked regions, and no heat flux across these regions either. Instead, the heat flux arrows circumvent the crack tip (Fig. 3.4(a) and (c)). On the contrary, when the thermal conductivity is not degraded with crack, i.e. constant crack, the heat flux directions don't change at all and the flux still crosses the cracked regions (Fig. 3.4(b) and (d)), which is not physically correct. It is also observed that the magnitudes of the heat flux increase at the crack tip since the flux concentrates at this region. Note that one can also consider other sources of heat transfer (e.g. convection or even radiation) at the damaged zone or where we have the discontinuity in the displacement field. In the current work, we are first restricted to heat transfer through conduction in solids.

3.4 Quenching test

In this section, the quenching tests are presented to further verify the phase-field fracture model. In the experimental side of this test, a ceramic plate with an initially high temperature is subjected to a cool water bath, and a series of parallel cracks are formed in the ceramics [119, 120].

In the numerical example, a ceramic slab of $50 \text{ mm} \times 10 \text{ mm}$ with a high initial temperature θ_0 is considered. The ambient temperature θ_a is lower, so there is a temperature difference $\Delta\theta$. For computational efficiency, only a quarter of the whole rectangle plate is modeled here. The symmetry boundary conditions are therefore applied on the corresponding edges, where the adiabatic condition is applied (i.e. no flux goes through these edges). The horizontal displacement is fixed on the right edge and the vertical displacement on the top edge is fixed, respectively. The remaining edges are subjected to quenching through heat conduction. The material properties are taken from [98] and are

listed in the Table. 3.3. In this quenching test, $\theta_0 = 300 \text{ }^\circ\text{C}$, $\theta_a = 20 \text{ }^\circ\text{C}$ and thus $\Delta\theta = 280 \text{ }^\circ\text{C}$. The length scale here $\ell_0 = 0.10 \text{ mm}$ with the fine mesh size $h = \ell_0/4$. The fixed time step is $\Delta t = 0.10 \text{ ms}$ and the total simulation time is 200 ms.

Table 3.3: Material parameters used for the quenching test.

E (GPa)	ν	G_{c0} (J/m ²)	σ_u (MPa)	ρ (kg/m ³)	k (W/mK)	c_p (J/kgK)	α
370	0.3	42.47	180	3980	31	880	$7.5e - 6$

The temperature field and crack development of the quenching test are simulated. At the beginning of quenching, the outer boundaries of ceramics are suddenly cooled down and tend to contract due to high temperature variations, which leads to tensile stress on the surface, while the inner materials are in compression for balance. When the thermal stress exceeds the fracture strength, damage starts to initiate. Following the direction of the temperature gradient, cracks initiate and propagate almost perpendicularly to the boundaries, and uniformly with equal spacing. Initially, the cracks propagate quite rapidly. As they propagate to the inner of the specimen, the propagation speed decreases gradually with the release of the thermal stress. Some cracks get arrested at a short length because the declining strain energy is unable to support all the cracks to further propagate simultaneously. Therefore, the remaining cracks gain more driving force to keep propagating further. The process repeats once again until the final crack pattern forms. For a more detailed description of the experimental quenching process, readers are referred to [120].

The comparison between the numerical result and experimental result of the quenching test for the whole specimen with an initial temperature of $300 \text{ }^\circ\text{C}$ is shown in the first row in Fig. 3.5. The crack pattern for the whole ceramic specimen is obtained by using symmetry conditions at the top edge and right edge of the quarter plate in post-processing. From the comparison, it is apparent that the results obtained from the proposed thermal fracture model show good agreement with the experiment results.

To further study the influence of the initial temperature of the ceramics on the final crack pattern, more quenching tests with different initial temperatures, i.e. $350 \text{ }^\circ\text{C}$, $400 \text{ }^\circ\text{C}$, $500 \text{ }^\circ\text{C}$ and $600 \text{ }^\circ\text{C}$ are conducted. The material parameters and model settings are the same as before. The comparison of the simulation results with the experimental observations [120] with different initial temperatures θ_0 is shown in Fig. 3.5. To quantitatively compare the results of the quenching test, we calculate the cracks that are approximately longer than the 10% of the width of the specimen. According to the work of [120], the regions within 10mm to the ends are excluded in order to remove the effects of the end boundaries. The number of cracks and the average crack spacing under different initial temperatures θ_0

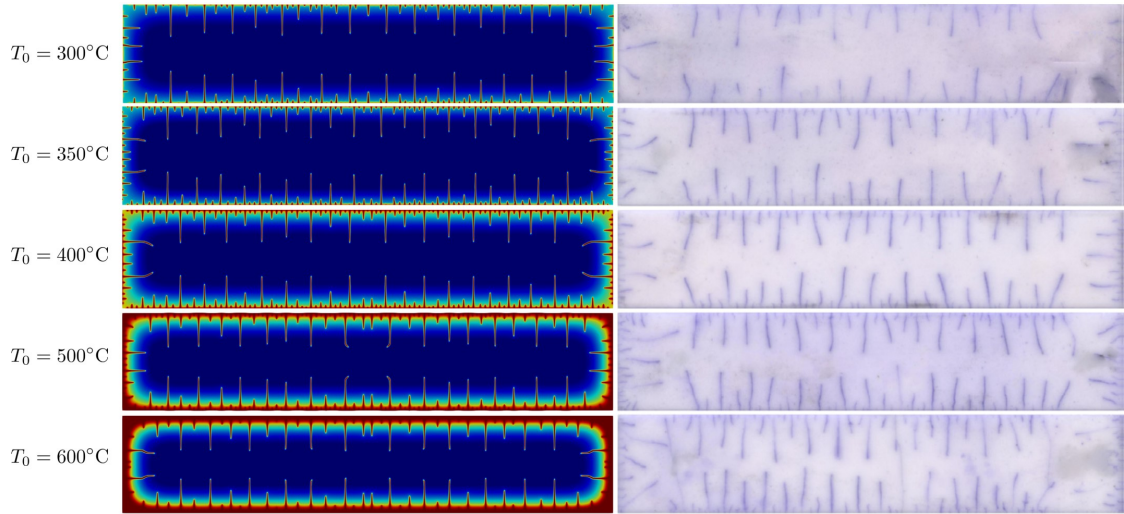


Figure 3.5: Quenching tests with different initial temperatures θ_0 . Comparison of crack patterns between numerical and experimental results. Reprinted from [120] with permission.

are summarized in the Table. 3.4. Note that for $\theta_0 = 500^\circ\text{C}$ and 600°C , because a large amount of diffusive damage accumulates near the boundaries which cannot be clearly detected, they are not compared here. Also one should note that the PF fracture model is by nature a smeared approach to fracture. As a result, by choosing a finite length scale parameter, we might end up with a continuous damage zone when there are so many cracks near each other. In other words, the continuous damage zone near the boundary can also be physically interpreted as many micro-cracks which are not easily visible in the experimental picture.

Table 3.4: Quantitative comparison of the quenching test under different initial temperatures.

θ_0 ($^\circ\text{C}$)	Numerical		Experimental	
	Number	Spacing	Number	Spacing
300	21	1.42	18	1.66
350	26	1.15	25	1.20
400	30	1.00	32	0.94

From the comparison, the thermal shock crack patterns (spacing, height hierarchy, and

periodicity) are similar for different initial temperatures θ_0 . The crack mechanism like crack initiation and propagation follows the same pattern as described before. However, the crack pattern still keeps evolving with the increase of θ_0 . The crack number increases with the higher initial temperature, and the crack becomes denser. The boundaries of the ceramics have a higher level of damage with increasing θ_0 . More cracks at the boundaries are formed as a result of higher thermal stress. In addition, the crack spacing also gets smaller and the longer cracks propagate even longer to the central part of the specimen. The experimental observations can also be reflected by the simulation results.

4 Thermo-elasto-plastic Phase-field Ductile Fracture at Finite Strains

4.1 Thermo-elasto-plastic phase-field ductile fracture model at finite strains

In this work, the framework for finite strain elastoplasticity based on the multiplicative decomposition of the deformation gradient and the principle of maximum plastic dissipation developed by [121] is adopted. Well-known continuum mechanical formalisms are used to describe the proposed model. To make the description self-contained and for the sake of clarity, we will formulate it in detail here. For the thermo-ductile problem, the primary field variables are the displacement field $\mathbf{u}(\mathbf{x}, t)$, the damage field $d(\mathbf{x}, t)$ and the temperature field $\theta(\mathbf{x}, t)$. The coupling mechanisms of the proposed model are shown in Fig. 4.1.

We use the notation common in continuum mechanics. Scalars, first-order tensors, second-order tensors and fourth-order tensors are represented by a , \mathbf{a} , \mathbf{A} , \mathbb{A} , respectively. Single and double contractions between two tensors are denoted as \mathbf{AB} and $\mathbf{A} : \mathbf{B}$. The operators $\nabla(\cdot)$ and $\nabla \cdot (\cdot)$ denote the gradient and divergence, and $\text{tr}(\mathbf{A})$, $\text{dev}(\mathbf{A})$, $\|\mathbf{A}\|$ represent the trace, the deviatoric part and the norm of second-order tensors, respectively.

4.1.1 Kinematics

Let $\Omega_0 \subset \mathbb{R}^d (d \in \{2, 3\})$ be the reference configuration with external boundary $\partial\Omega_0$ and $\Omega_t \subset \mathbb{R}^d$ be the current configuration with current boundary $\partial\Omega_t$ at time t . The deformation of the body is described by the deformation mapping $\varphi(\mathbf{X}, t) : \mathbf{X} \rightarrow \mathbf{x}$, which maps the reference material points $\mathbf{X} \in \Omega_0$ at time $t \in [0, \tau]$ onto the current material points $\mathbf{x} \in \Omega_t$ such that $\mathbf{x} = \varphi(\mathbf{X}, t)$. The deformation gradient is defined as

$$\mathbf{F} = \varphi_{,\mathbf{X}} = \frac{\partial \varphi(\mathbf{X}, t)}{\partial \mathbf{X}}, \quad (4.1)$$

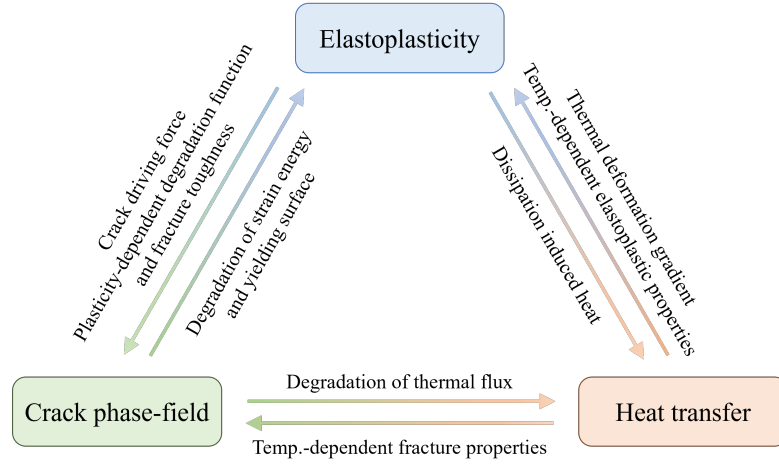


Figure 4.1: Schematic of the coupling mechanism among elastoplasticity, crack phase-field and heat transfer.

and the displacement of the point \mathbf{X} is given as

$$\mathbf{u}(\mathbf{X}, t) = \varphi(\mathbf{X}, t) - \mathbf{X}. \quad (4.2)$$

For finite strain plasticity, the stress-free intermediate configuration is assumed. The multiplicative decomposition of total deformation gradient \mathbf{F} into its elastic part \mathbf{F}^e and plastic part \mathbf{F}^p is assumed as $\mathbf{F} = \mathbf{F}^e \mathbf{F}^p$. For thermo-mechanical problems, a third configuration is introduced accounting for the thermal deformation. To this end, the total deformation gradient is multiplicatively decomposed as

$$\mathbf{F} = \mathbf{F}^m \mathbf{F}^\theta = \mathbf{F}^e \mathbf{F}^p \mathbf{F}^\theta, \quad (4.3)$$

where \mathbf{F}^m and \mathbf{F}^θ represent the mechanical and thermal part of the deformation gradient. For a general anisotropic thermal expansion, the corresponding thermal deformation gradient is defined as

$$\mathbf{F}^\theta = \mathbf{I} + \boldsymbol{\alpha}_t(\theta - \theta_0), \quad (4.4)$$

where θ_0 is the reference temperature, and $\boldsymbol{\alpha}_t = \text{diag}(\alpha_1, \alpha_2, \alpha_3)$ is a diagonal tensor of anisotropic thermal expansion coefficients with α_i ($i=1,2,3$) being the thermal expansion coefficients along the principal crystallographic directions. By assuming isotropic thermal expansion, \mathbf{F}^θ is simplified to be

$$\mathbf{F}^\theta = (1 + \alpha_t(\theta - \theta_0)) \mathbf{I}. \quad (4.5)$$

The right Cauchy–Green deformation tensor and the plastic right Cauchy–Green deformation tensor are defined as

$$\mathbf{C} = \mathbf{F}^T \mathbf{F}, \quad \mathbf{C}^p = \mathbf{F}^{pT} \mathbf{F}^p. \quad (4.6)$$

Similarly, associated with the current configuration, the total left Cauchy–Green strain tensor and the elastic left Cauchy–Green strain tensor are given as

$$\mathbf{b} = \mathbf{F} \mathbf{F}^T, \quad \mathbf{b}^e = \mathbf{F}^e \mathbf{F}^{eT}. \quad (4.7)$$

In view of Eq. 4.3 and Eq. 4.6,

$$\mathbf{b}^e = \mathbf{F}^m \mathbf{C}^{p-1} \mathbf{F}^{mT}, \quad (4.8)$$

with its Lie derivative as

$$\mathcal{L}_v \mathbf{b}^e = \mathbf{F}^m \dot{\mathbf{C}}^{p-1} \mathbf{F}^{mT}. \quad (4.9)$$

4.1.2 Thermodynamics: Dissipation inequality

To derive the constitutive equations in a thermodynamically consistent manner, the second law of thermodynamics, expressed in the form of local Clausius-Duhem inequality with respect to the reference configuration is shown in Eq. 4.10. The extension of the microforce balance acting on the fracture surface is incorporated.

$$\mathcal{D} = \mathbf{S} : \frac{1}{2} \dot{\mathbf{C}} - \pi \dot{d} + \boldsymbol{\xi} \cdot \nabla \dot{d} - (\dot{\psi} + \dot{\theta} \eta) - \frac{1}{\theta} \nabla \theta \cdot \mathbf{q} \geq 0, \quad (4.10)$$

where \mathbf{S} is the second Piola-Kirchhoff stress, π is the internal microforce and $\boldsymbol{\xi}$ is the microstress, ψ and η are the free energy and the entropy, respectively, \mathbf{q} is the heat flux.

For the thermo-mechanically coupled fracture problem, the energy functional is assumed as a functional of the variables $\psi = \psi(\mathbf{C}, \mathbf{C}^p, \alpha, d, \nabla d, \theta)$, and decomposed as the following parts

$$\psi(\mathbf{C}, \mathbf{C}^p, \alpha, d, \nabla d, \theta) = \underbrace{\psi_e(\mathbf{C}, \mathbf{C}^p, \theta)}_{\text{elastic energy}} + \underbrace{\psi_p(\alpha, \nabla \alpha, \theta)}_{\text{plastic hardening}} + \underbrace{\Delta_p(\alpha, \theta)}_{\text{plastic dissipation}} + \underbrace{\psi_c(d, \nabla d, \theta)}_{\text{fracture energy}} + \underbrace{\psi_\theta(\theta)}_{\text{thermal energy}} \quad (4.11)$$

where the specific expressions of these energy terms are to be discussed later. According to the energy balance, the internal energy e per unit reference volume is defined as

$$\dot{e} = \mathbf{S} : \frac{1}{2} \dot{\mathbf{C}} - \pi \dot{d} + \boldsymbol{\xi} \cdot \nabla \dot{d} - \nabla \mathbf{q} + Q, \quad (4.12)$$

where Q is the external heat source. Using the Legendre transformation, the internal energy expressed by the Helmholtz free energy and entropy η as

$$e = \psi + \theta\eta. \quad (4.13)$$

Substituting Eq. 4.11 - Eq. 4.13 into Eq. 4.10 yields

$$\left(\mathbf{S} - 2 \frac{\partial \psi}{\partial \mathbf{C}} \right) : \frac{1}{2} \dot{\mathbf{C}} - \frac{\partial \psi}{\partial \mathbf{C}^p} : \dot{\mathbf{C}}^p - \frac{\partial \psi}{\partial \alpha} \dot{\alpha} - \left(\pi + \frac{\partial \psi}{\partial d} \right) \dot{d} + \left(\boldsymbol{\xi} - \frac{\partial \psi}{\partial \nabla d} \right) \nabla \dot{d} - \left(\eta + \frac{\partial \psi}{\partial \theta} \right) \dot{\theta} - \frac{1}{\theta} \mathbf{q} \cdot \nabla \theta \geq 0 \quad (4.14)$$

The inequality must hold for arbitrary thermodynamic processes, which leads to the following thermodynamic relations:

$$\left\{ \begin{array}{l} \text{Second Piola-Kirchhoff stress: } \mathbf{S} = 2 \frac{\partial \psi}{\partial \mathbf{C}} \\ \text{Microstress: } \boldsymbol{\xi} = \frac{\partial \psi}{\partial \nabla d} \\ \text{Internal microforce: } \pi = - \frac{\partial \psi}{\partial d} \\ \text{Entropy: } \eta = - \frac{\partial \psi}{\partial \theta}. \end{array} \right. \quad (4.15)$$

The Fourier's law reads,

$$\mathbf{q} = -k \nabla \theta. \quad (4.16)$$

The specific expression of the terms above will be present in the following sections, according to the choice of the energy functional. Then the Clausius-Duhem inequality is reduced to

$$- \frac{\partial \psi}{\partial \mathbf{C}^p} : \dot{\mathbf{C}}^p - \frac{\partial \psi}{\partial \alpha} \dot{\alpha} \geq 0, \quad (4.17)$$

which is satisfied on the condition of appropriate choice of evolution functions.

4.1.3 Damage informed Elastoplastiy

Consistent with the assumption of isotropy and the notion of an intermediate stress-free configuration, for the compressible Neo-Hookean hyperelastic material model, the

damaged elastic strain energy is decomposed as [83, 122, 123]

$$\begin{aligned}\psi_e &= g(d, \alpha)W^+ + W^- \\ W^+ &= \begin{cases} U(J^e) + \bar{W}(\bar{\mathbf{b}}^e), & J^e \geq 1 \\ \bar{W}(\bar{\mathbf{b}}^e) & J^e < 1 \end{cases} \\ W^- &= \begin{cases} 0, & J^e \geq 1 \\ U(J^e) & J^e < 1, \end{cases}\end{aligned}\quad (4.18)$$

where $U(J^e)$ and $\bar{W}(\bar{\mathbf{b}}^e)$ are the volumetric and deviatoric parts of ψ_e , and expressed as

$$\begin{aligned}U(J^e) &= \frac{1}{2}\kappa(\theta) \left[\frac{1}{2}(J^{e2} - 1) - \ln J^e \right] \\ \bar{W}(\bar{\mathbf{b}}^e) &= \frac{1}{2}\mu(\theta) (\text{tr}[\bar{\mathbf{b}}^e] - 3).\end{aligned}\quad (4.19)$$

Here, $\kappa(\theta)$ and $\mu(\theta)$ are the temperature-dependent bulk modulus and shear modulus, respectively.

Assuming the plastic flow is isochoric, we have

$$\det \mathbf{F}^p = 1 \Rightarrow J^m = J^e = \det \mathbf{F}^e. \quad (4.20)$$

The volume-preserving left Cauchy-Green strain is defined as

$$\bar{\mathbf{b}}^e := J^{e-2/3} \mathbf{F}^e \mathbf{F}^{eT} \equiv J^{e-2/3} \mathbf{b}^e. \quad (4.21)$$

Then, the second Piola-Kirchhoff stress tensor is derived from Eq. 4.15

$$\mathbf{S} = 2g(d, \alpha) \frac{\partial W^+}{\partial \mathbf{C}} + 2 \frac{\partial W^-}{\partial \mathbf{C}} = g(d, \alpha) \mathbf{S}^+ + \mathbf{S}^-, \quad (4.22)$$

and the Kirchhoff stress tensor is

$$\begin{aligned}\boldsymbol{\tau} &= \mathbf{F}^e \mathbf{S} \mathbf{F}^{eT} = g(d, \alpha) \boldsymbol{\tau}^+ + \boldsymbol{\tau}^- \\ \boldsymbol{\tau}^+ &= \begin{cases} J^e p \mathbf{I} + \mathbf{s} & J^e \geq 1 \\ \mathbf{s} & J^e < 1 \end{cases} \\ \boldsymbol{\tau}^- &= \begin{cases} \mathbf{0} & J^e \geq 1 \\ J^e p \mathbf{I} & J^e < 1, \end{cases}\end{aligned}\quad (4.23)$$

where $J^e p \mathbf{1}$ and \mathbf{s} are the volumetric and deviatoric part of the Kirchhoff stress and are defined as follows,

$$\begin{aligned} p &:= U'(J^e) = \frac{\kappa(\theta)}{2} (J^{e2} - 1) / J^e \\ \mathbf{s} &:= \text{dev}[\boldsymbol{\tau}] = \mu(\theta) \text{dev}[\bar{\mathbf{b}}^e]. \end{aligned} \quad (4.24)$$

Finally, the Cauchy stress tensor is obtained by the push-forward of the second Piola-Kirchhoff stress from the intermediate stress-free configuration to the current configuration

$$\begin{aligned} \boldsymbol{\sigma} &= g(d, \alpha) \boldsymbol{\sigma}^+ + \boldsymbol{\sigma}^- \\ \boldsymbol{\sigma}^+ &= \begin{cases} p \mathbf{I} + J^{e-1} \mathbf{s} & J^e \geq 1 \\ J^{e-1} \mathbf{s} & J^e < 1 \end{cases} \\ \boldsymbol{\sigma}^- &= \begin{cases} \mathbf{0} & J^e \geq 1 \\ p \mathbf{I} & J^e < 1. \end{cases} \end{aligned} \quad (4.25)$$

Considering the body force \mathbf{b} , the momentum balance equation reads

$$\nabla \cdot \boldsymbol{\sigma} + \mathbf{b} = 0. \quad (4.26)$$

The degraded Mises-Huber yield surface function is

$$f(\boldsymbol{\tau}, d, \alpha, \theta) = \|\mathbf{s}\| - g(d, \alpha) \sqrt{\frac{2}{3}} H_p(\alpha, \theta), \quad (4.27)$$

where α is the hardening variable, $H_p(\alpha, \theta)$ is the hardening function, the commonly-used ones are

$$H_p(\alpha, \theta) = \begin{cases} \sigma_Y(\theta) & \text{(Perfect plasticity)} \\ \sigma_Y(\theta) + H(\theta)\alpha & \text{(Linear hardening)} \end{cases} \quad (4.28)$$

where $\sigma_Y(\theta)$ and $H(\theta)$ are the temperature-dependent yield strength and hardening modulus. Note that for the materials with a strong hardening effect, like steel 1.0553, the saturation-type hardening function is often used [122, 87].

$$H_p(\alpha, \theta) = \sigma_Y(\theta) + H(\theta)\alpha + (\sigma_\infty(\theta) - \sigma_Y(\theta)) (1 - \exp(-\delta\alpha)), \quad (4.29)$$

where $\sigma_\infty(\theta)$ is the temperature-dependent ultimate tensile strength, and δ is the saturation coefficient. For thermal fracture problems, the thermal softening effect plays a significant role. In line with [100, 124], the temperature-dependency of the material

parameters is considered as $f(\theta) = (1 - \omega(\theta - \theta_0))$, where ω and θ_0 are the softening parameter and reference temperature, respectively. Then it leads to

$$\begin{aligned}\sigma_Y(\theta) &= \sigma_{Y0}(1 - \omega_0(\theta - \theta_0)), \\ \sigma_\infty(\theta) &= \sigma_{\infty 0}(1 - \omega_h(\theta - \theta_0)), \\ H(\theta) &= H_0(1 - \omega_h(\theta - \theta_0)).\end{aligned}\tag{4.30}$$

For the general plastic hardening, ψ_p takes a complex form, here only the linear hardening contribution is considered

$$\psi_p(\alpha, \theta) = \frac{1}{2}H(\theta)\alpha^2.\tag{4.31}$$

The plastic dissipation can be expressed as

$$\Delta_p(\alpha, \theta) = \sigma_Y(\theta)\alpha.\tag{4.32}$$

The elastoplastic constitutive model is completed by the plasticity flow rule. The associative flow rule, defined by the principle of maximum plastic dissipation, takes the form as

$$\begin{aligned}\text{dev}[\mathcal{L}_v \mathbf{b}^e] &= -\frac{2}{3}\dot{\gamma} \text{tr}[\mathbf{b}^e] \mathbf{n} \\ \mathbf{n} &= \frac{\mathbf{s}}{\|\mathbf{s}\|}.\end{aligned}\tag{4.33}$$

Note that Eq. 4.33 only defines the deviatoric part of $[\mathcal{L}_v \mathbf{b}^e]$. The evolution of the spherical part is determined by the isochoric assumption Eq. 4.20.

For isotropic hardening, the evolution of internal hardening variable α follows

$$\dot{\alpha} = \sqrt{\frac{2}{3}}\dot{\gamma},\tag{4.34}$$

where $\dot{\gamma}$ is the plastic multiplier that follows the principle of maximum plastic dissipation and is subject to the standard Karush-Kuhn–Tucker (KKT) loading/unloading conditions

$$\dot{\gamma} \geq 0, \quad f(\boldsymbol{\tau}, d, \alpha, \theta) \leq 0, \quad \dot{\gamma} f(\boldsymbol{\tau}, d, \alpha, \theta) = 0.\tag{4.35}$$

The discrete form of KTT conditions is discussed in Sec. 4.2.2.

4.1.4 Phase-field modeling of ductile fracture

Consider a cracked solid Ω with an external boundary denoted by $\partial\Omega$ and a crack set Γ . Starting from Griffith's theory in fracture mechanics, the total fracture energy is given by

$$\psi_c = \int_{\Gamma} G_c(\alpha, \theta) \, dA = \int_{\Omega} G_c(\alpha, \theta) \gamma_c(d, \nabla d) dV, \quad (4.36)$$

where $G_c(\alpha, \theta)$ is the critical energy release rate. In the relation above, we substitute the surface integral with a volumetric integral which yields an approximation of the fracture energy [62, 64, 106]. Here, γ_c is the crack surface density function defined as

$$\gamma_c(d, \nabla d) = \frac{1}{c_0} \left(\frac{1}{\ell_0} \omega(d) + \ell_0 |\nabla d|^2 \right), \quad c_0 = 4 \int_0^1 \sqrt{\omega(\beta)} d\beta, \quad (4.37)$$

where the length scale parameter ℓ_0 is used to regularize the sharp crack to the diffusive crack width. The crack geometric function $\omega(d)$ characterizes the homogeneous evolution of the phase-field crack, which has the properties

$$\omega(d) \in [0, 1], \omega(0) = 1, \omega(x) \rightarrow 0 : x \rightarrow \pm\infty, \quad (4.38)$$

and it takes the form as

$$\omega(d) = 2d - d^2. \quad (4.39)$$

To include the plastic contribution to the fracture process, the degradation function is modified to be [122]

$$g(d, \alpha) = (1 - d)^{2\frac{\alpha}{\alpha_{cp}}} + \eta, \quad (4.40)$$

where α_{cp} is the threshold value for the equivalent plastic strain, η is a small parameter to guarantee a residual stiffness even in fully-cracked regions to avoid numerical convergence issues.

For quasi-static fracture assuming that micro-inertia is negligible, the microforce momentum balance equation is given by

$$\nabla \cdot \boldsymbol{\xi} + \pi = 0, \quad (4.41)$$

where $\boldsymbol{\xi}$ and π are defined in Eq. 4.15. Employing the microforce balance equation and substituting the fracture energy given in Eq. 4.36, the governing equation of the phase-field evolution is obtained

$$\frac{2G_c(\alpha, \theta)\ell_0}{c_0} \nabla^2 d - g'(d, \alpha)\mathcal{H} - \frac{G_c(\alpha, \theta)}{c_0\ell_0} \omega'(d) = 0, \quad (4.42)$$

where \mathcal{H} is the history variable introduced in [64] to enforce the irreversibility of the crack field, and expressed as

$$\mathcal{H} = \max_{t \in [0, \tau]} W^+(\mathbf{C}, \mathbf{C}^p). \quad (4.43)$$

It is worth noting that to include the contribution of the plastic work in ductile fracture, the driving force can be modified to be [83]

$$\mathcal{H} = \max_{t \in [0, \tau]} (\beta_e W^+(\mathbf{C}, \mathbf{C}^p) + \beta_p (\psi_p - \psi_{p0})), \quad (4.44)$$

where $\beta_e \in [0, 1]$ and $\beta_p \in [0, 1]$ are used to weigh the contribution to the crack field from elastic energy and plastic work, respectively. Moreover, ψ_{p0} is the threshold for plastic work, introduced to control the point when the plastic work starts to take effect.

To incorporate the influence of the plastic flow on the ductile fracture process, here the fracture toughness is degraded by the plastic internal variable, where the relation $f_c(\alpha)$ has the properties as,

$$0 < f_c(\alpha) \leq 1; \quad \partial_\alpha f_c(\alpha) \leq 0. \quad (4.45)$$

As the plasticity is irreversible, the degradation function decreases monotonically with the increase of the plastic variable. The degradation mechanism is often utilized in the phase-field modeling of fatigue fracture [125, 126, 127]. In line with [89], the following form is adopted.

$$G_c = f_c(\alpha) G_{c0}$$

$$f_c(\alpha) = \begin{cases} 1, & \alpha < \alpha_{cf} \\ \frac{1-b}{a^2} (\alpha - \alpha_{cf} - a)^2 + b, & \alpha_{cf} \leq \alpha < \alpha_{cf} + a \\ b, & \alpha \leq \alpha_{cf} + a, \end{cases} \quad (4.46)$$

where α_{cf} is the threshold of plasticity from which the degradation mechanism is triggered, a and b are the softening parameters defining the profile of the degradation function.

4.1.5 Heat transfer

Derived in a thermodynamically consistent manner from the energy balance, the heat transfer equation is given as

$$c\dot{\theta} = k(d)\nabla^2\theta + \theta \left(\frac{\partial \mathcal{S}}{\partial \theta} : \frac{1}{2}\dot{\mathbf{C}} + \frac{\partial \pi}{\partial \theta} \dot{d} + \frac{\partial \boldsymbol{\xi}}{\partial \theta} \nabla d + \frac{\partial^2 \psi}{\partial \alpha \partial \theta} \dot{\alpha} + \frac{\partial^2 \psi}{\partial \mathbf{C}^p \partial \theta} \dot{\mathbf{C}}^p \right) + \frac{\partial \psi}{\partial \alpha} \dot{\alpha} + \frac{\partial \psi}{\partial \mathbf{C}^p} \dot{\mathbf{C}}^p, \quad (4.47)$$

where c is the heat capacity. The derivative terms in Eq. 4.47 are due to thermo-elastoplastic coupling and dissipation mechanism, which serve as the additional heat source generation. By assuming quasi-static crack propagation, the heat equation reduces to

$$c\dot{\theta} = k(d)\nabla^2\theta, \quad (4.48)$$

where the thermal conductivity is considered to be degraded by damage such that

$$k(d) = ((1 - d)^2 + \eta)k_0. \quad (4.49)$$

This form ensures that there is no heat flux across the crack to avoid nonphysical phenomena. The thermal contribution to the energy functional takes the following form

$$\psi_\theta(\theta) = c \left(\theta - \theta_0 - \theta \ln \left(\frac{\theta}{\theta_0} \right) \right), \quad (4.50)$$

where θ_0 is the reference temperature.

4.1.6 Summary of the coupled model

With the introduction of the previous sections, the formulations of the initial/boundary value problem (IBVP) are presented. The governing equations and related constitutive relations are summarized in Table. 4.1, with intercoupling mechanisms among elastoplasticity, phase-field crack and heat transfer being comprehensively considered. The schematic of them is shown in Fig. 4.1. Notably, the damage-plasticity coupling is threefold, which exhibits the yield surface Eq. 4.27, the degradation function Eq. 4.40, and the fracture toughness Eq. 4.46, respectively.

As formulated in the sections above, there are complex coupling mechanisms for this thermo-elastoplastic-ductile fracture model. To make it clear, the coupling terms between different physics in this work are summarized below.

- elasticity with phase-field crack

$$\begin{aligned} \psi_e &= g(d, \alpha)W^+ + W^- \\ \boldsymbol{\sigma} &= g(d, \alpha)\boldsymbol{\sigma}^+ + \boldsymbol{\sigma}^- \end{aligned} \quad (4.51)$$

- plasticity with phase-field crack

$$\begin{aligned} g(d, \alpha) &= (1 - d)^{\frac{2\alpha}{\alpha_{cp}}} + \eta \\ f(\boldsymbol{\tau}, d, \alpha) &= \|\boldsymbol{s}\| - g(d, \alpha)\sqrt{\frac{2}{3}}H(\alpha) \\ G_c &= f(\alpha)G_{c0} \end{aligned} \quad (4.52)$$

Table 4.1: Summary of the phase-field model of thermo-ductile fracture at finite strains

Variables	Governing equations	Constitutive relations	Coupled parameters
Crack phase-field	$\nabla \cdot \boldsymbol{\xi} + \pi = 0$	$\boldsymbol{\xi} = \frac{2G_c(\alpha, \theta)l_c}{c_0} \nabla d$ $\pi = -g'(d, \alpha)\mathcal{H} - \frac{G_c(\alpha, \theta)\omega'(d)}{c_0 l_0}$ $\mathcal{H} = \max_{t \in [0, \tau]} (\beta_e W^+ + \beta_p (\psi_p - \psi_{p0}))$ $g(d, \alpha) = (1-d)^{2-\frac{\alpha}{\alpha_{cp}}} + \eta$ $\omega(d) = 2d - d^2$ $c_0 = 4 \int_0^1 \sqrt{\omega(\beta)} d\beta$	$G_c(\alpha, \theta)$: plast. & temp.-dependent fracture toughness $g(d, \alpha)$: damage & plast.-dependent degradation function
Displacement	$\nabla \cdot \boldsymbol{\sigma} + \mathbf{b} = 0$	$\mathbf{F} = \varphi, X = \mathbf{F}^e \mathbf{F}^p \mathbf{F}^\theta$ $\boldsymbol{\sigma} = g(d, \alpha)\boldsymbol{\sigma}^+ + \boldsymbol{\sigma}^-$ $\boldsymbol{\sigma}^+ = \begin{cases} p\mathbf{I} + J^{e-1}\mathbf{s} \\ J^{e-1}\mathbf{s}, \end{cases} \quad \boldsymbol{\sigma}^- = \begin{cases} 0, J^e \geq 1 \\ p\mathbf{I}, J^e < 1 \end{cases}$ $p = \frac{\kappa(\theta)}{2} (J^{e2} - 1) / J^e, \quad \mathbf{s} = \mu(\theta) \operatorname{dev} [\bar{\mathbf{b}}^e]$ $J^e = \det \mathbf{F}^e, \quad \mathbf{b}^e = \mathbf{F}^e \mathbf{F}^{eT}$ $f(\boldsymbol{\tau}, d, \alpha, \theta) = \ \mathbf{s}\ - g(d, \alpha) \sqrt{\frac{2}{3}} H_p(\alpha, \theta)$ $H_p(\alpha, \theta) = \sigma_Y(\theta) + H(\theta)\alpha + (\sigma_\infty(\theta) - \sigma_Y(\theta))(1 - \exp(-\delta\alpha))$ $\operatorname{dev} [\mathcal{L}_v \mathbf{b}^e] = -\frac{2}{3} \dot{\gamma} \operatorname{tr} [\mathbf{b}^e] \mathbf{n}$ $\dot{\alpha} = \sqrt{\frac{2}{3}} \dot{\gamma}, \quad \mathbf{n} = \frac{\mathbf{s}}{\ \mathbf{s}\ }$ $\dot{\gamma} \geq 0, \quad f \leq 0, \quad \dot{\gamma} f = 0$	$\kappa(\theta)$: temp.-dependent bulk modulus $\mu(\theta)$: temp.-dependent shear modulus $\sigma_Y(\theta)$: temp.-dependent yield strength $\sigma_\infty(\theta)$: temp.-dependent ultimate strength $H(\theta)$: temp.-dependent hardening modulus
Temperature	$\nabla \cdot \mathbf{q} + c\dot{\theta} = 0$	$\mathbf{q} = -k(d)\nabla\theta$ $k(d) = (1-d)^2 + \eta$	$k(d)$: damage-dependent thermal conductivity

- heat transfer with elastoplasticity

$$\begin{aligned}
H_p(\alpha, \theta) &= \sigma_Y(\theta) + H(\theta)\alpha + (\sigma_\infty(\theta) - \sigma_Y)(1 - \exp(-\delta\alpha)) \\
\sigma_Y(\theta) &= \sigma_{Y0}(1 - \omega_0(\theta - \theta_0)) \\
\sigma_\infty(\theta) &= \sigma_{\infty0}(1 - \omega_h(\theta - \theta_0)) \\
H(\theta) &= H_0(1 - \omega_h(\theta - \theta_0)) \\
\mathbf{F} &= \mathbf{F}^e \mathbf{F}^p \mathbf{F}^\theta
\end{aligned} \tag{4.53}$$

- heat transfer with phase-field crack

$$k(d) = g(d)k_0 \tag{4.54}$$

4.2 Numerical implementation

4.2.1 Finite element discretization

In this session, the finite element implementation of the model is presented. The spatial discretization is formulated using the Galerkin method. According to the strong form of the governing equations in Table. 4.1, by multiplying corresponding arbitrary test functions and considering the divergence theorem and the boundary conditions, the weak form is established.

$$\int_{\Omega} \boldsymbol{\sigma} : \nabla \delta_u dV - \int_{\Omega_t} \mathbf{t}^* \delta_u dS = 0, \tag{4.55a}$$

$$\int_{\Omega} \frac{G_c}{\ell_0 c_0} \omega'(d) \delta_d dV + \int_{\Omega} \frac{2G_c \ell_0}{c_0} \nabla d \nabla \delta_d dV + \int_{\Omega} g'(d) \mathcal{H} \delta_d dV = 0, \tag{4.55b}$$

$$\int_{\Omega} c \dot{\theta} \delta_\theta dV + \int_{\Omega} k \nabla \theta \nabla \delta_\theta dV - \int_{\Omega_t} k \nabla \theta \delta_\theta dS = 0. \tag{4.55c}$$

With the standard finite element method, the field variables \mathbf{u} , d and θ , as well as their first spatial derivatives, are approximated as

$$\begin{cases}
\mathbf{u} = \sum N_u^i u_i = \mathbf{N}_u \mathbf{u}_e, & \boldsymbol{\varepsilon} = \sum B_u^i u_i = \mathbf{B}_u \mathbf{u}_e, \\
d = \sum N_d^i d_i = \mathbf{N}_d \mathbf{d}_e, & \nabla d = \sum B_d^i d_i = \mathbf{B}_d \mathbf{d}_e, \\
\theta = \sum N_\theta^i \theta_i = \mathbf{N}_\theta \boldsymbol{\theta}_e, & \nabla \theta = \sum B_\theta^i \theta_i = \mathbf{B}_\theta \boldsymbol{\theta}_e.
\end{cases} \tag{4.56}$$

Here, u_i , d_i and θ_i are the nodal values of the displacement, damage and temperature field of node i of element e , respectively. N_u , N_d , N_θ and B_u , B_d , B_θ denote the shape functions

and their derivatives for the displacement, damage field and temperature, respectively. \mathbf{N}_u , \mathbf{N}_d , \mathbf{N}_θ and \mathbf{B}_u , \mathbf{B}_d , \mathbf{B}_θ are the corresponding shape function matrix and derivatives. For a quadrilateral 2D element they are written as

$$\mathbf{N}_u = \begin{bmatrix} N_1 & 0 & \cdots & N_4 & 0 \\ 0 & N_1 & \cdots & 0 & N_4 \end{bmatrix}, \quad \mathbf{B}_u = \begin{bmatrix} N_{1,x} & 0 & \cdots & N_{4,x} & 0 \\ 0 & N_{1,y} & \cdots & 0 & N_{4,y} \\ N_{1,y} & N_{1,x} & \cdots & N_{4,y} & N_{4,x} \end{bmatrix}, \quad (4.57)$$

$$\mathbf{N}_d = \mathbf{N}_\theta = [N_1 \quad \cdots \quad N_4], \quad \mathbf{B}_d = \mathbf{B}_\theta = \begin{bmatrix} N_{1,x} & \cdots & N_{4,x} \\ N_{1,y} & \cdots & N_{4,y} \end{bmatrix}. \quad (4.58)$$

Similarly, the test functions and their spatial derivatives are discretized as

$$\begin{cases} \delta_u = \mathbf{N}_u \delta_u^i, & \nabla \delta_u = \mathbf{B}_u \delta_u^i, \\ \delta_d = \mathbf{N}_d \delta_d^i, & \nabla \delta_d = \mathbf{B}_d \delta_d^i, \\ \delta_\theta = \mathbf{N}_\theta \delta_\theta^i, & \nabla \delta_\theta = \mathbf{B}_\theta \delta_\theta^i. \end{cases} \quad (4.59)$$

Inserting the discretization relations above, we obtain the following equations for the residuals of different fields

$$\mathbf{r}_u = \int_{\Omega} \mathbf{B}_u^T \boldsymbol{\sigma} dV - \int_{\Omega_t} \mathbf{N}_u^T \mathbf{t}^* dS, \quad (4.60a)$$

$$\mathbf{r}_d = \int_{\Omega} \frac{G_c}{\ell_0 c_0} \omega'(d) \mathbf{N}_d^T \mathbf{N}_d dV + \int_{\Omega} \frac{2G_c \ell_0}{c_0} \mathbf{B}_d^T \mathbf{B}_d dV + \int_{\Omega} g'(d) \mathbf{N}_d^T \mathcal{H} dV, \quad (4.60b)$$

$$\mathbf{r}_\theta = \int_{\Omega} c \dot{\theta} \mathbf{N}_\theta dV + \int_{\Omega} \mathbf{B}_\theta^T k \mathbf{B}_\theta dV - \int_{\Omega_t} \mathbf{B}_\theta^T k \mathbf{N}_\theta dS. \quad (4.60c)$$

For this thermo-elasto-plastic coupled fracture problem, the energy functional is non-convex with respect to the two unknowns displacement and crack phase-field simultaneously. Therefore it is challenging to solve all the unknown variables at the same time utilizing the conventional Newton-Raphson method. However, the energy functional is convex with respect to each of the two variables separately when the other is fixed, which is the so-called staggered or alternative minimization algorithm.

The theoretical model is numerically implemented by the Finite Element Method within the framework of Multiphysics Object-Oriented Simulation Environment (MOOSE) [128]. The coupled sets of partial differential equations (PDEs) of the bulk element are solved by `Portable, Extensible Toolkit for Scientific Computation (PETSc)` [129]. The staggered solution scheme is implemented with the `MultiApp` [130] system in MOOSE, by which individual physics systems can be solved simultaneously. For transient problems, `TransientMultiApp` is utilized, which performs coupled simulations with

sub applications that progress in time and iterate with the main application. Within each iteration, the applications are required to transfer data from and to the others. In this work, the thermo-elasto-plastic couple problem is solved monolithically as the main application while keeping the phase-field crack frozen. Sequentially, the phase-field crack evolution equation is solved in the sub application with the updated displacements and temperature. The irreversibility constraint $\dot{d} \geq 0$ is enforced during this calculation. After the phase-field crack is updated, it is transferred back to the main application for further steps until the simulation ends.

4.2.2 Return-mapping algorithm

The procedure of the return-mapping scheme for the finite-strain elastoplasticity using the backward Euler scheme is summarized in this section. The algorithm follows the algorithm proposed by [121] for elastoplasticity and modified by [83] for fracture problems. Readers interested are referred to them for more details.

For the current time interval $[t_n, t_{n+1}]$, assume the states $\varphi_n, \mathbf{F}_n, \mathbf{b}_n^e, \alpha_n, d_n, \theta_n$ at the previous timestep are known. The configuration at the current timestep t_{n+1} is updated by the incremental displacement field \mathbf{u}_n as

$$\mathbf{x}_{n+1} = \varphi_{n+1}(\mathbf{X}) = \varphi_n(\mathbf{X}) + \mathbf{u}_n[\varphi_n(\mathbf{X})]. \quad (4.61)$$

Then, the deformation gradient and the relative deformation gradient are obtained as

$$\mathbf{F}_{n+1} = [\mathbf{1} + \nabla_{\mathbf{x}_n} \mathbf{u}_n] \mathbf{F}_n, \quad (4.62)$$

$$\mathbf{f}_{n+1} = \mathbf{F}_{n+1} \mathbf{F}_n^{-1} = \mathbf{1} + \nabla_{\mathbf{x}_n} \mathbf{u}_n. \quad (4.63)$$

From Eq. 4.63, the volume-preserving part reads

$$\bar{\mathbf{f}}_{n+1} = \det[\mathbf{f}_{n+1}]^{-1/3} \mathbf{f}_{n+1}. \quad (4.64)$$

Assuming a pure elastic trial response and no plasticity evolution, i.e., $\alpha_{n+1}^{trial} = \alpha_n$, the trial deformation is given as

$$\bar{\mathbf{b}}_{n+1}^{e \text{ trial}} = \bar{\mathbf{f}}_{n+1} \bar{\mathbf{b}}_n^e \bar{\mathbf{f}}_{n+1}^T, \quad (4.65)$$

with the trial damaged deviatoric part of Kirchhoff stress as

$$\mathbf{s}_{n+1}^{trial} = g(d_n, \alpha_n) \mu(\theta_n) \text{dev} \left[\bar{\mathbf{b}}_{n+1}^e \right]. \quad (4.66)$$

The discrete Karush-Kuhn-Tucker loading/unloading conditions are

$$f(\boldsymbol{\tau}_{n+1}, d_n, \alpha_{n+1}, \theta_n) \leq 0, \quad \Delta\gamma \geq 0, \quad \Delta\gamma f(\boldsymbol{\tau}_{n+1}, d_n, \alpha_{n+1}, \theta_n) = 0. \quad (4.67)$$

The yield function at the trial stress state is defined as

$$f_{n+1}^{\text{trial}} = f\left(\boldsymbol{\tau}_{n+1}^{\text{trial}}, d_n, \alpha_n, \theta_n\right) = \left\| \mathbf{s}_{n+1}^{\text{trial}} \right\| - g(d_n, \alpha_n) \sqrt{\frac{2}{3}} H_p(\alpha_n). \quad (4.68)$$

If $f_{n+1}^{\text{trial}} \leq 0$, then the trial elastic state with $\Delta\gamma = 0$ satisfies conditions, Thus, the trial elastic step is the solution at time t_{n+1} ,

$$(\cdot)_{n+1} = (\cdot)_{n+1}^{\text{trial}}. \quad (4.69)$$

Alternatively, if $f_{n+1}^{\text{trial}} > 0$, it means the trial state is not admissible, and $\Delta\gamma > 0$ needs to be updated to satisfy $f_{n+1}^{\text{trial}} = 0$.

$$\bar{\mathbf{b}}_{n+1}^e = \bar{\mathbf{b}}_{n+1}^{\text{trial}} - \frac{2}{3} \Delta\gamma \text{tr} \left[\bar{\mathbf{b}}_{n+1}^e \right] \mathbf{n}_{n+1}, \quad (4.70)$$

$$\alpha_{n+1} = \alpha_n + \sqrt{\frac{2}{3}} \Delta\gamma, \quad (4.71)$$

$$\mathbf{n}_{n+1} = \mathbf{s}_{n+1} / \left\| \mathbf{s}_{n+1} \right\|. \quad (4.72)$$

Then, the stress is updated as

$$\mathbf{s}_{n+1} = \mathbf{s}_{n+1}^{\text{trial}} - 2\bar{\mu} \Delta\gamma \mathbf{n}_{n+1}, \quad (4.73)$$

where

$$\bar{\mu} = \frac{1}{3} g(d_n, \alpha_n) \mu \text{tr} \left[\bar{\mathbf{b}}_{n+1}^{\text{trial}} \right]. \quad (4.74)$$

Then the $\Delta\gamma$ is obtained by solving the scalar-type yield function

$$f(\Delta\gamma) = \left\| \mathbf{s}_{n+1}^{\text{trial}} \right\| - g(d_n, \alpha_n) \sqrt{\frac{2}{3}} H_p \left(\alpha_n + \sqrt{\frac{2}{3}} \Delta\gamma \right) - 2\bar{\mu} \Delta\gamma = 0. \quad (4.75)$$

4.3 I-shape specimen tensile test

In this section, one of the canonical benchmark examples, i.e., the tensile test of the I-shape specimen is simulated. The simulation results are compared with experimental ones to validate the proposed model. Afterward, the influence of the characteristic parameters of the model and the temperature are studied.

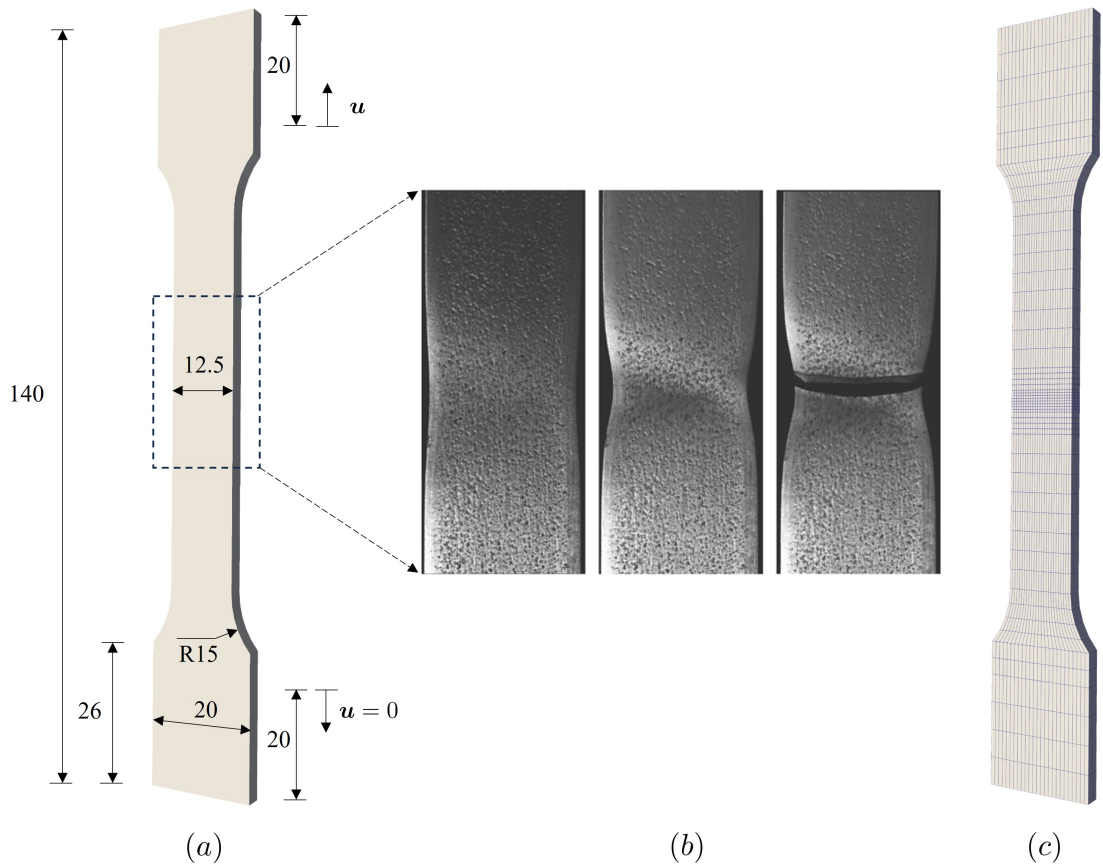


Figure 4.2: Tensile test of I-shape flat Steel-1.0553 specimen. (a) Geometry and boundary conditions, (b) experimental observations during tensile test [81] and (c) FE discretized mesh with a refined zone in the central regions.

4.3.1 Benchmark example: tensile test of I-shape specimen

In this section, the phase-field ductile fracture model is validated with the experimental tensile test of an I-shape specimen made of steel 1.0553. The geometry of the I-shape specimen (unit: mm) with 3mm-thickness is shown in Fig. 4.2(a). In the test, the lower end is fixed while the upper end is clamped and subject to external displacement. The experimental observations of the tensile test [122] are shown in Fig.4.2(b). The mesh used in the simulation is shown in Fig.4.2(c). In the central regions where the plastic strain is expected to accumulate and the necking and cracking are expected to initiate and

propagate, the meshes are refined so that the phase-field is well-resolved. The material properties of Steel-1.0553 and numerical parameters used in the simulations in this section are listed in Table. 4.2. Note that Steel-1.0553 is a material with a strong hardening effect. Thus, the saturation-type hardening function Eq. 4.29 is adopted.

Table 4.2: Material/numerical parameters used in the simulations

symbol	material/numerical parameters	value
K	bulk modulus	150 (GPa)
G	shear modulus	73.255 (GPa)
σ_{Y0}	yield strength	343 (MPa)
σ_{∞}	ultimate strength	680 (MPa)
H	hardening modulus	300 (MPa)
G_{c0}	fracture toughness	1000 (KJ/m ²)
θ_0	reference temperature	293 (K)
ℓ_0	length scale parameter	0.5 (mm)
δ	saturation coefficient	26
α_{cp}	threshold in $g(d, \alpha)$	1.0
α_{cf}	threshold in $f_c(\alpha)$	1.0
ω_0	softening parameter	2e-3
ω_h	softening parameter	1e-3
a	profile parameter $f(\alpha)$	0.1
b	profile parameter $f(\alpha)$	1e-6

To validate the elastoplastic constitutive model, the crack phase-field is deactivated first, and the pure mechanical response of the tensile test at constant temperature is simulated. The load-displacement curve of the elastoplastic response is shown in Fig. 4.3. Fig. 4.4 depicts the evolution of the equivalent plastic strain and the Von-Mises stress of loading stages ($p1$) - ($p4$) at displacement $\mathbf{u} = [10.0, 12.0, 14.0, 15.0]$ mm. The specimen behaves purely elastically till the yield point is reached. As the deformation progresses, the plasticity starts to accumulate in the necking regions. The load-displacement curve agrees with the experiment in the elastoplastic scope.

Afterward, the crack phase-field is activated and the complete ductile fracture model is simulated. The evolution of the displacement along the loading direction, the crack phase-field, the equivalent plastic strain and the Von-Mises stress of loading stages ($q1$) - ($q4$) at displacement $\mathbf{u} = [11.0, 12.0, 12.5, 12.9]$ mm are shown in Fig. 4.5. The response behaves similarly to the pure elastoplastic one at the beginning. At the plastic state, as

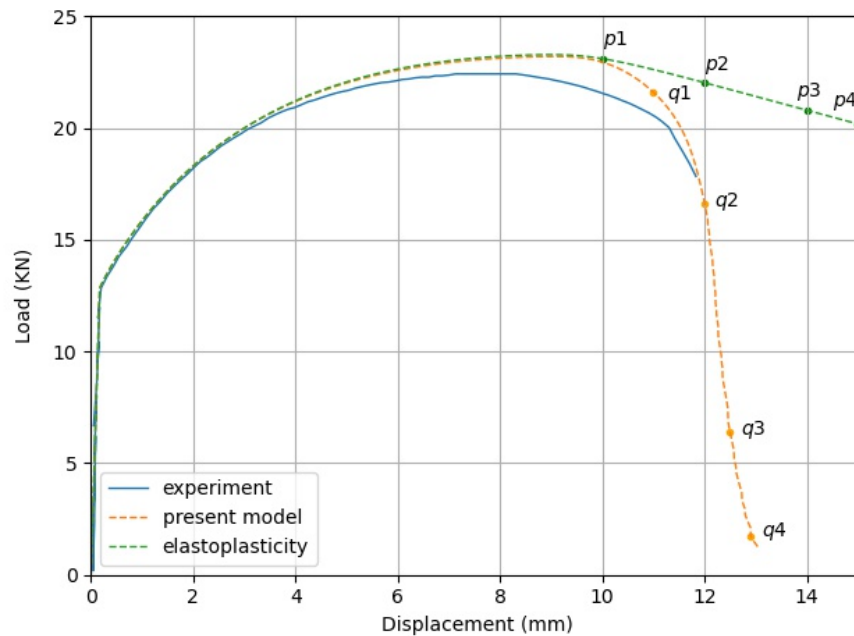


Figure 4.3: Comparison of load-displacement curves of tensile test of I-shape specimen between simulation and experimental results [122]. The snapshots of simulations of the labeled points ($p1$) - ($p4$), ($q1$) - ($q4$) are shown in Fig. 4.4 and 4.5, respectively.

a result of large deformation and corresponding crack drive force in the middle of the specimen, damage accumulates and concentrates in the regions. With the increase of the plastic deformation, the threshold for equivalent plastic strain is reached. Consequently, the fracture toughness is degraded and accelerates the crack propagation till the final fracture.

The load-displacement curve of the process is compared to the experimental results in Fig. 4.3. From the comparison, the simulation result agrees well with the experiment result [122] in the elastic regime and the initial plastic hardening regime. As the externally applied displacement further increases, the damage accumulates, and the coupling between elasto-plastic-damage plays a more significant role. The experimental load-displacement exhibits a stronger softening behavior than the numerical counterpart. The deviation can be attributed to multiple reasons. One reason could be that the specimen in the experiment is not perfect, which undermines the properties of the specimen. Moreover, as

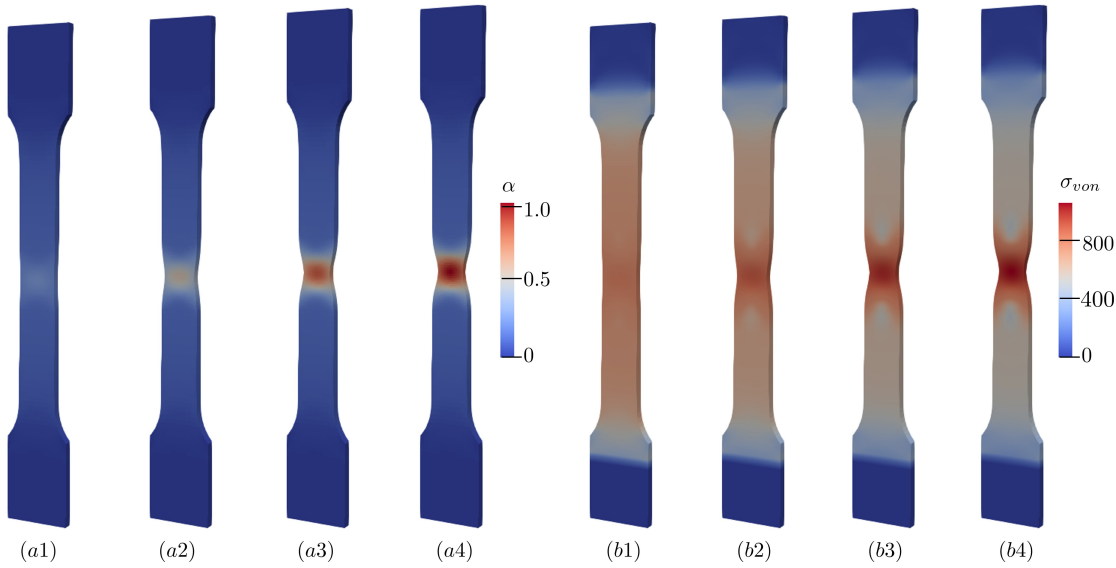


Figure 4.4: Elastoplastic response of tensile test of I-shape steel-1.0553 specimen without damage of points $(p_1) - (p_4)$. Evolution of $(a_1) - (a_4)$ equivalent plastic strain and $(b_1) - (b_4)$ Von-Mises stress at displacement $u = [10.0, 12.0, 14.0, 15.0]$ mm.

expressed in Eq. 4.47, the couplings between elastoplasticity-damage serve as an additional heat source, resulting in the thermal softening of the material parameter. However, this softening behavior is neglected for quasi-static assumption in the current model. The coupling between damage and plasticity is still an open question, and more potential damage-plasticity coupling mechanisms are worthy of further study. Nevertheless, the overall response of the ductile fracture process of the simulation agrees well with the experimental results. It demonstrates that the proposed model is able to capture the whole ductile fracture process, including elastoplasticity, yielding, necking, crack initiation, and propagation.

4.3.2 characteristic parameters study of the model

For the phase-field model, the length-scale parameter ℓ_0 plays an important role. For the standard phase-field model for brittle fracture, i.e., AT1 and AT2 models, the fracture process is significantly dependent on the length-scale parameter [65]. For example, the peak stress of the load-displacement curve of the pure tensile test is decreasing with the

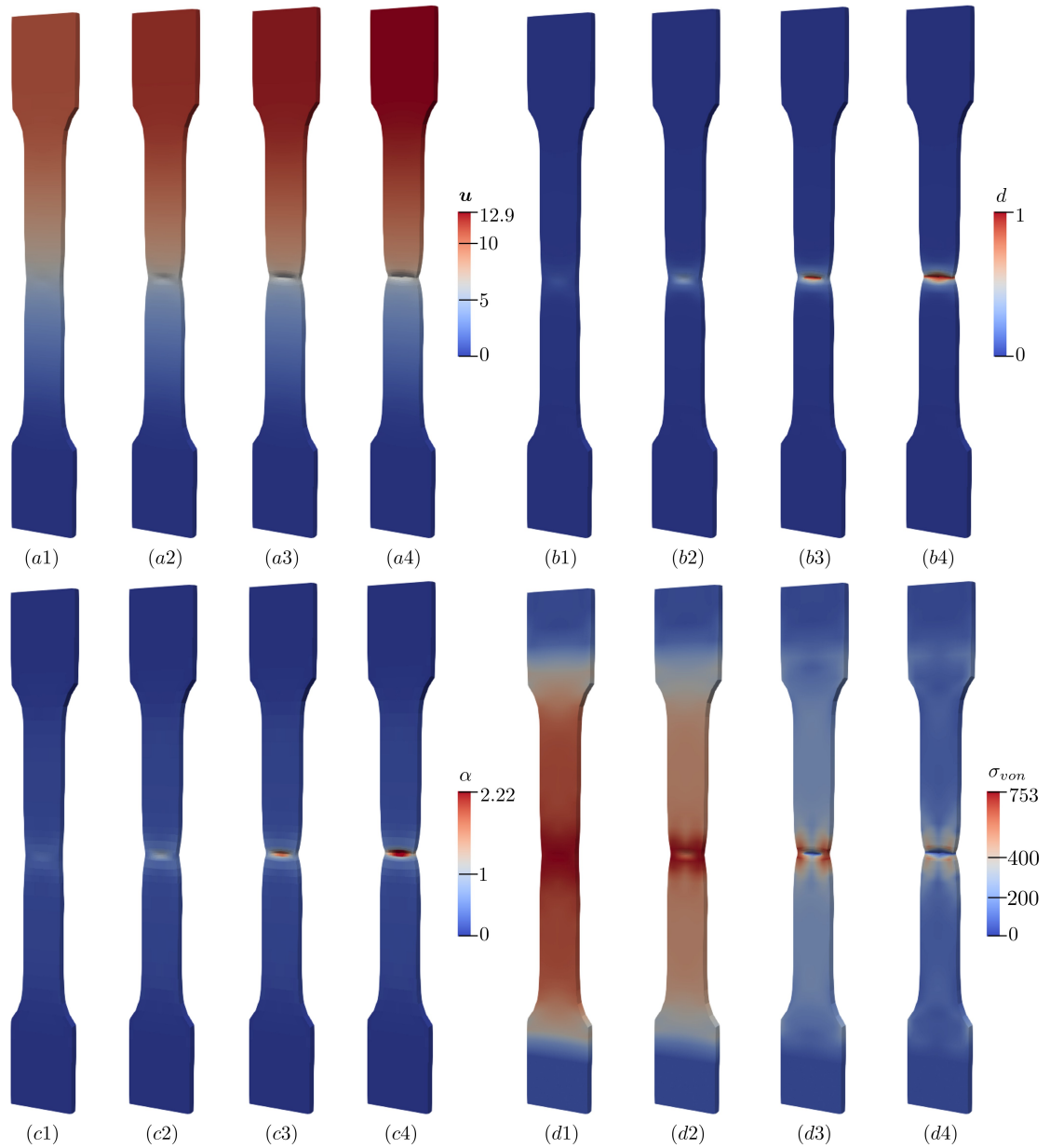


Figure 4.5: Fracture process of tensile test of I-shape steel-1.0553 specimen at points (q1) - (q4). Evolution of (a1) - (a4) displacement, (b1) - (b4) damage, (c1) - (c4) equivalent plastic strain and (d1) - (d4) Von-Mises stress at displacement $u = [11.0, 12.0, 12.5, 12.9]$ mm.

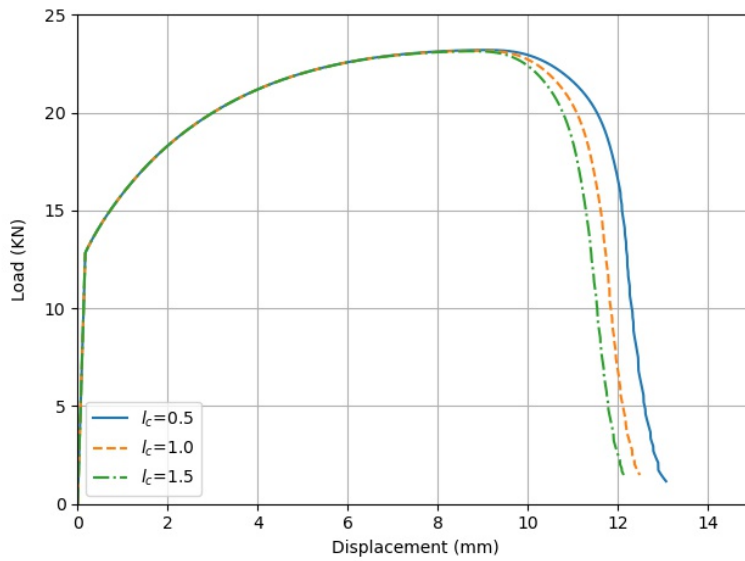


Figure 4.6: Influence of length scale parameter on load-displacement curves of tensile test.

increase of ℓ_0 . For the cohesive-phase-field model, it incorporates material parameters like Young's modulus, yield strength and fracture toughness into the degradation function, so the response is relatively insensitive to ℓ_0 . For the proposed ductile fracture model, the simulations with different ℓ_0 are performed to study the influence, and the load-displacement curves are compared in Fig.4.6. It shows that with different ℓ_0 the peak load of the curves keeps almost the same, but the crack develops earlier when bigger ℓ_0 is used.

As described in Eq. 4.44, the driving force for ductile fracture can be varied from the brittle fracture considering the contribution of the plastic work and the threshold. Herein, the influence of different driving forces is also studied, with the results shown in Fig. 4.7. Compared with pure elastic energy, the inclusion of the plastic contribution to the driving force facilitates the fracture process. The larger threshold of plastic contribution corresponds to the larger effective plastic strain from which the plastic contribution is triggered. Consequently, the fracture process is relatively delayed. In the case that the threshold is too large to exceed, the plastic energy cannot exceed and then the plastic part would not make any contribution to the crack driving force throughout the fracture process.

Moreover, the comparison of the fracture process at different temperatures is performed,

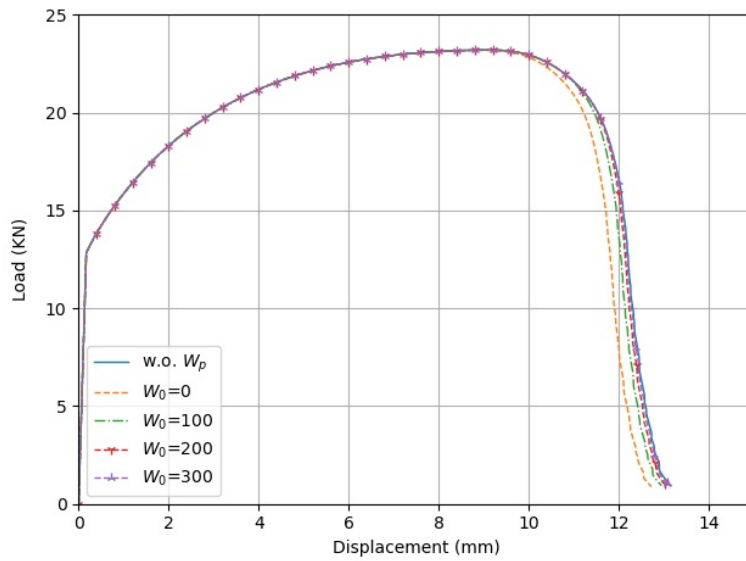


Figure 4.7: Influence of crack driving force on load-displacement curves of tensile test.

showing the influence of the temperature. Because of the thermal softening effect Eq. 4.30, the initial yield strength decreases with increasing temperature, as shown in Fig. 4.8. The hardening effects are also relatively weaker as the ultimate strength and the hardening modulus are also smaller compared with those at room temperature. These simulations show the capability of the proposed model to predict thermo-ductile fracture in the thermo-elasto-plastic solids.

To study the influence of the critical threshold for the effective plastic strain in the degradation function $g(d, \alpha)$ and $f(\alpha)$ on the fracture process, a series of simulations are conducted.

In Eq. 4.40, α_{cp} controls from which point the plasticity has a more significant effect in the degradation function of the fracture process. The smaller α_{cp} is, the easier for the effective plastic strain to overpass the threshold, thus the earlier severe degradation takes effect, and eventually the earlier fracture happens. The analysis corresponds to the trend shown in Fig. 4.9.

Meanwhile, the parameter α_{cf} in Eq. 4.46 controls when the fracture toughness starts to be degraded by the plastic flow. The comparison of the influence of α_{cf} on the load-displacement curve is shown in Fig. 4.10. It is apparent that fracture happens earlier with a smaller α_{cf} .

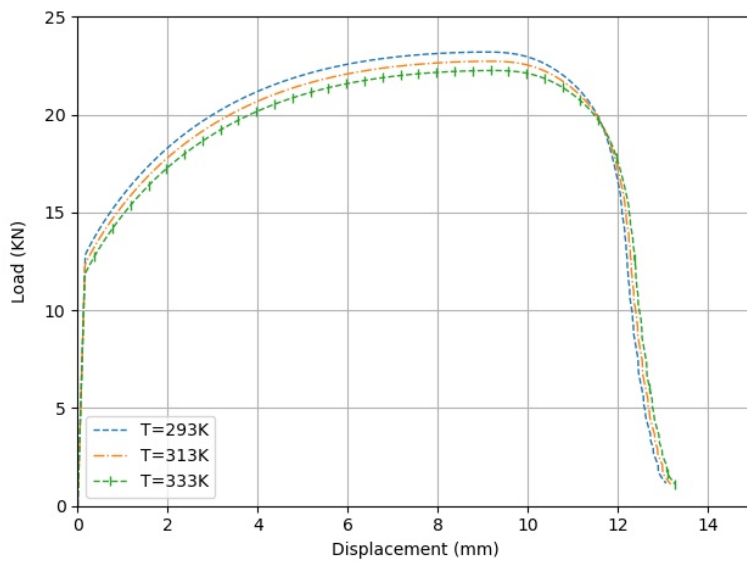


Figure 4.8: Influence of temperature on load-displacement curves of tensile test.

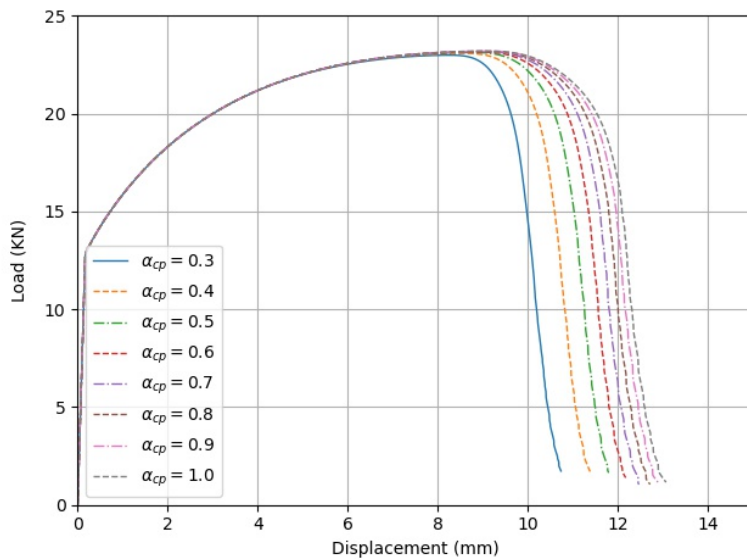


Figure 4.9: Influence of the threshold for the effective plastic strain α_{cp} in $g(d, \alpha)$ on load-displacement curves of tensile test of I-shape specimen

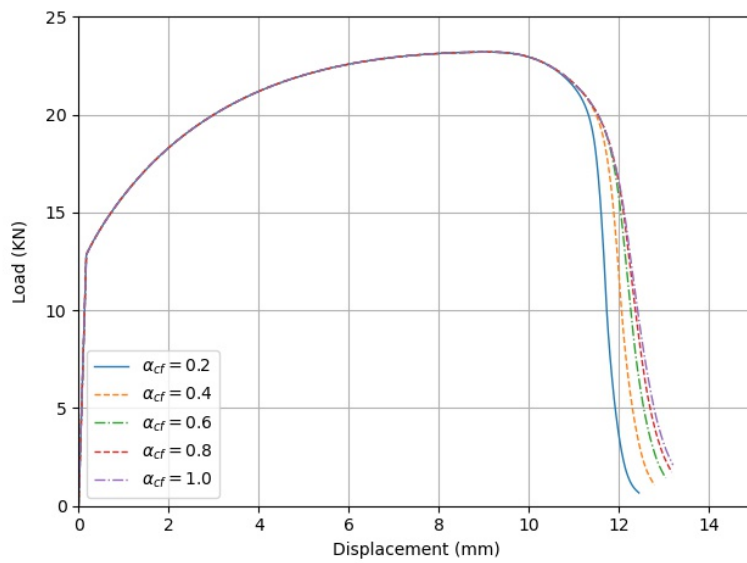


Figure 4.10: Influence of the threshold α_{cf} on load-displacement curves of tensile test.

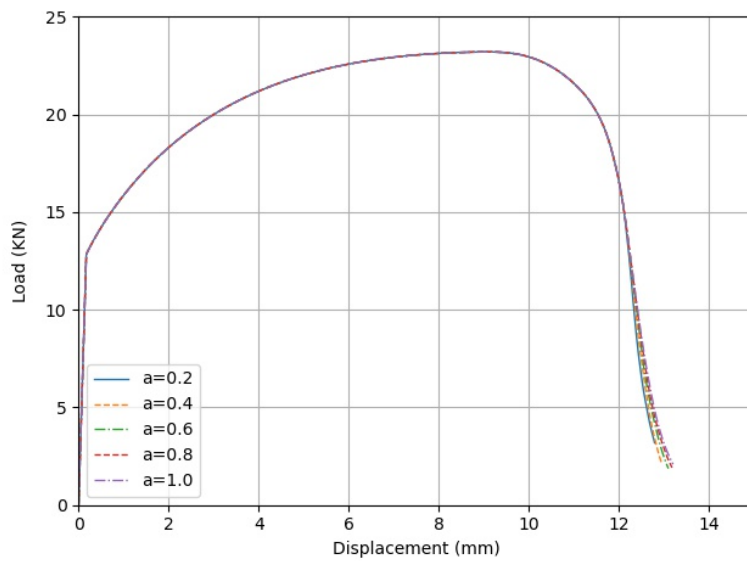


Figure 4.11: Influence of the parameter a on load-displacement curves of tensile test.

Likewise, the influence of a in Eq. 4.46 is shown in Fig. 4.11. a determines the interval of the equivalent plastic strain where the fracture toughness is degraded from the initial value to the degraded value b . The bigger a means the fracture toughness is degraded more smoothly after the effective plastic strain exceeding α_{cf} . Therefore, the fracture happens more slowly in a bigger interval of the effective plastic strain, compared with counterparts with a smaller value of a .

5 Thermal Cracking in Additive Manufacturing

In this chapter, the numerical study of the hot cracking phenomenon during the AM process, as schematically shown in Fig. 5.1, using the proposed phase-field model for thermal fracture is presented.

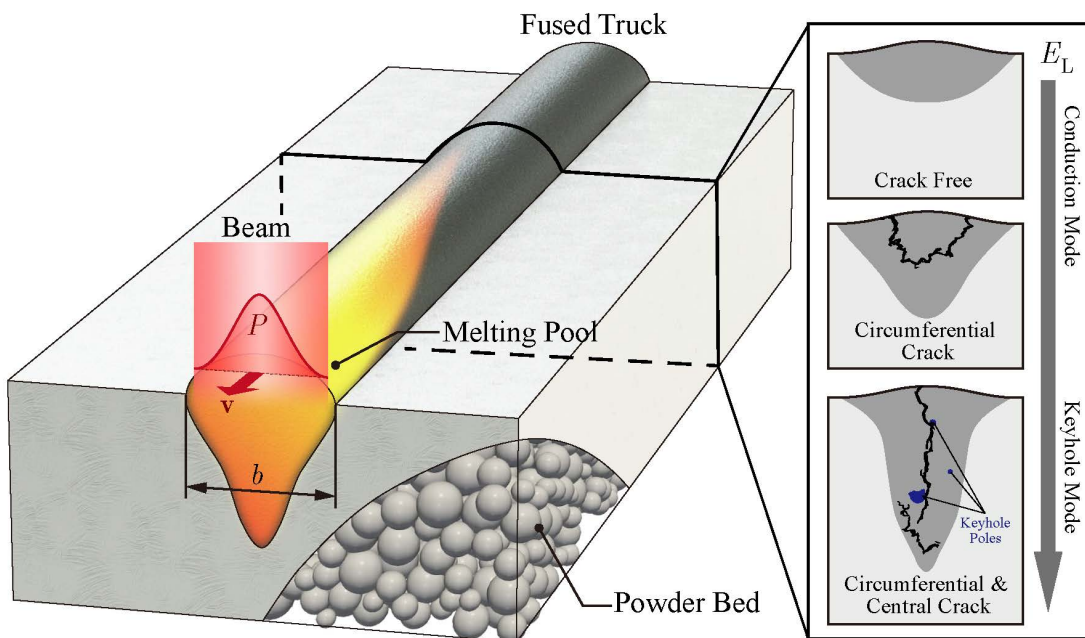


Figure 5.1: Schematic of AM process and hot cracking phenomenon. Different hot cracking patterns in the melting pool for conduction mode and keyhole mode hot cracking with the increase of energy density

During AM processes, specifically Powder Bed Fusion (PBF), different hot cracking patterns are observed in the different processes. Typically for the conduction mode AM

process, the hot cracking shows as a circumferential crack, while for the keyhole mode AM process, it shows up as a combination of circumferential crack and central crack. The two different patterns are thereby termed the conduction mode hot cracking and keyhole mode hot cracking, respectively.

5.1 Solidification shrinkage

To introduce the simulation setup, the solidification shrinkage is introduced first. In PBF, the solid-state powders melt when the temperature exceeds the melting temperature. Afterwards, it resolidifies when the temperature drops below the liquidus temperature. Most metals and alloys contract on solidifying, and the liquid-solid contraction leads to volume change, which adds the phase transformation strain to the total strain calculation, as shown in Fig. 5.2. Therefore, the mechanism of the solidification shrinkage is different from that of thermal strain induced by temperature change [131]. Meanwhile, the contribution of solidification shrinkage is relatively significant and has to be considered in the calculations. For example, the solidification shrinkage for aluminum is 6.6%, equivalent to 2.2% of the linear contraction, which is about 50% greater than the thermal contraction of cooling from the melting temperature to room temperature (about 1.5%) [132]. Therefore, the solidification shrinkage plays a significant role in the strain and stress field, particularly in the vicinity of the melting pool. Interestingly enough, this phenomenon is usually overlooked by researchers in numerical simulations of the AM process.

In this thesis, the solidification shrinkage strain ϵ_{SS} is simulated utilizing the effective thermal expansion coefficient. Solidification happens within a certain temperature range for alloys, i.e., the liquidus temperature θ_L and solidus temperature θ_S . The shrinkage is proportional to the change of solid fraction. Therefore, it is assumed to be linearly distributed in the temperature range and can be treated as an additional thermal expansion term caused by temperature changes [132]. Here, we assume the effective thermal expansion coefficient $\tilde{\alpha}(\theta)$ takes the following form:

$$\tilde{\alpha}(\theta) = \begin{cases} \alpha_t & \theta \leq \theta_S, \\ \alpha_t + \alpha_{SS} & \theta_S \leq \theta \leq \theta_L, \\ \alpha_t, & \theta_L \leq \theta, \end{cases} \quad (5.1)$$

where $\alpha_{SS} = \frac{\epsilon_{SS}}{\theta_L - \theta_S}$. Correspondingly, the thermal strain is obtained via:

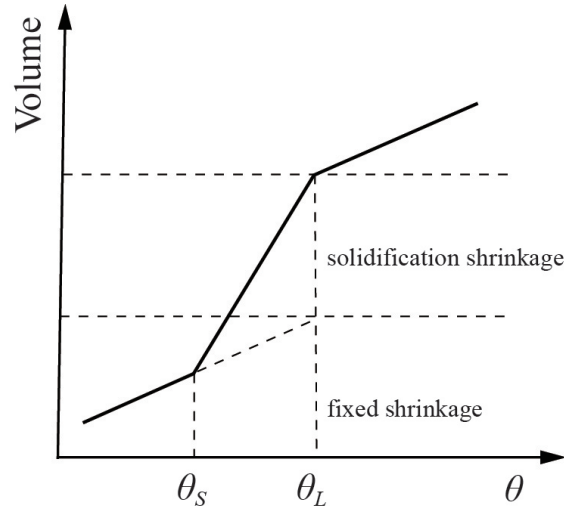


Figure 5.2: Volume change with temperature [131] and solidification shrinkage between θ_S and θ_L .

$$\varepsilon_\theta = \tilde{\alpha}(\theta)(\theta - \theta_0) = \begin{cases} \alpha_t(\theta - \theta_0), & \theta < \theta_S \\ \alpha_t(\theta - \theta_0) + \alpha_{SS}(\theta - \theta_S), & \theta_S \leq \theta < \theta_L \\ \alpha_t(\theta_L - \theta_0) + \varepsilon_{SS}, & \theta_L \leq \theta \end{cases} \quad (5.2)$$

5.2 Hot cracking with interpolated elliptic temperature profile

As the initial condition of θ , we first apply a simple interpolated solution for the thermal profile around the melt pool, and then the numerically calculated thermal profiles by a phenomenological PBF model and powder-resolved model of LPBF, respectively. The latter allows a more high-fidelity temperature field during the PBF process and the parameter study on different process parameters.

We start with the interpolated elliptic solution of the temperature profile in the vicinity of the melting pool [133], half of which is shown in Fig. 5.3(a). For a specific point (x, y) in Cartesian coordinates within the cross-section perpendicular to the scanning direction, x and y are the distance from the current location to the center line and the top surface of the melting pool, respectively. The point can also be represented by polar coordinates

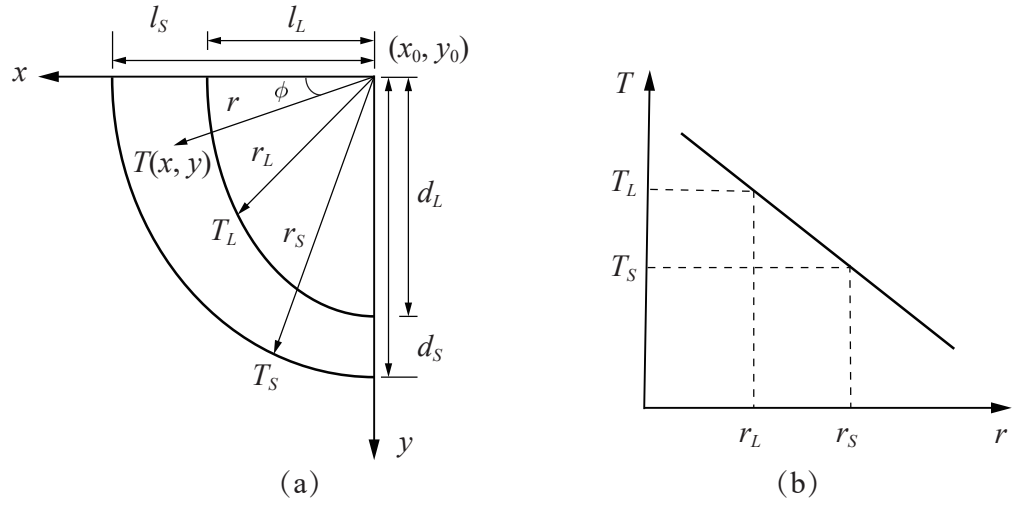


Figure 5.3: (a) Schematic of the elliptic temperature field approximation. (b) Linear interpolation of temperature profile.

(r, ϕ) , which are calculated by

$$r = \sqrt{x^2 + y^2}, \quad \phi = \tan^{-1} \left| \frac{y - y_0}{x - x_0} \right|, \quad (5.3)$$

where r denotes the distance to the center of the ellipses (x_0, y_0) , and ϕ is the angle starting from the top surface to the current position, as shown in Fig. 5.3(b). The temperature is calculated by linear interpolation between liquidus temperature θ_L and solidus temperature θ_S as

$$\theta(x, y) = \theta(r, \phi) = \theta_L + c(\theta_S - \theta_L) \frac{r - r_L(\phi)}{r_S(\phi) - r_L(\phi)}. \quad (5.4)$$

Here, $r_L(\phi)$ and $r_S(\phi)$ indicate the respective of $\theta = \theta_L$ and $\theta = \theta_S$ elliptical isolines. They are functions of ϕ and are calculated by

$$r_L(\phi) = \sqrt{\frac{(l_L d_L)^2}{(d_L \cos(\phi))^2 + (l_L \sin(\phi))^2}}, \quad (5.5)$$

$$r_S(\phi) = \sqrt{\frac{(l_S d_S)^2}{(d_S \cos(\phi))^2 + (l_S \sin(\phi))^2}}.$$

The length parameters (l_L, l_S) and the depth parameters (d_L, d_S) correspond to liquidus and solidus isotherms, respectively. As there is a large temperature gradient in the vicinity of the melting pool, a coefficient c is included in Eq. 5.4. The approximated temperature field is schematically shown in Fig. 5.3(b).

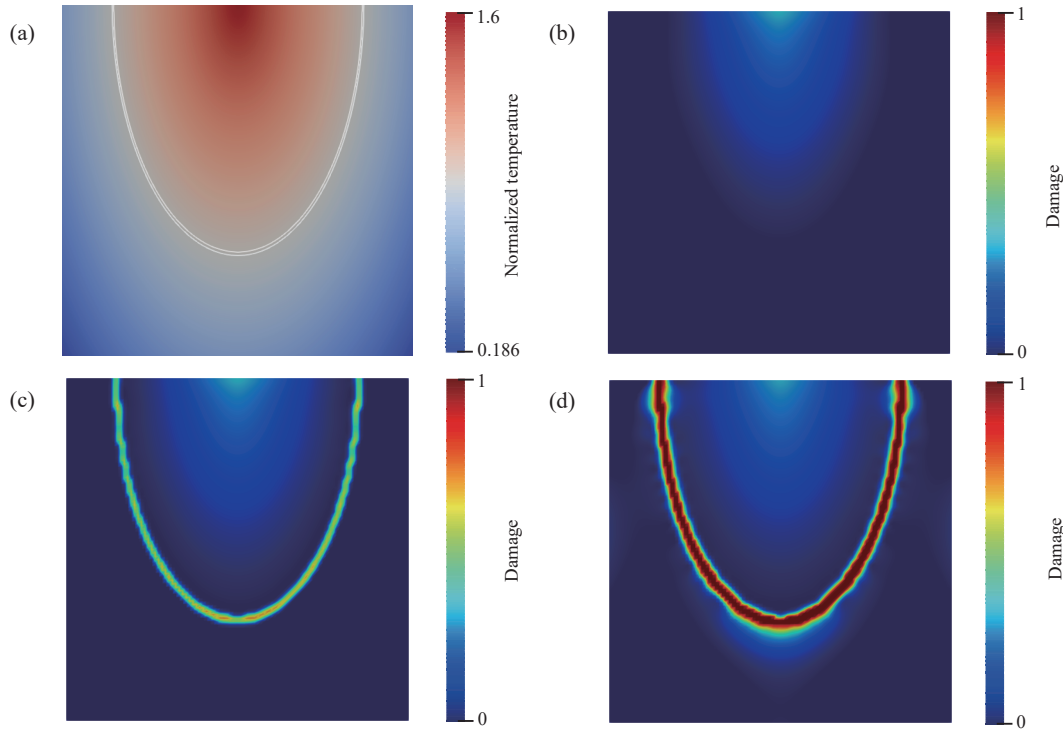


Figure 5.4: Hot cracking of single track of PBF with an aspect ratio of 1.0. (a) Normalized temperature field obtained by linear interpolation approximation, Hot cracking patterns with increasing solidification shrinkage strain, (b) $\alpha_{SS}=0$, (c) $4\alpha_t$ and (d) $26.7\alpha_t$, respectively.

In this example, a cross-section of $10\text{ mm}\times 10\text{ mm}$ perpendicular to the scanning direction is simulated. Since it is mechanically constrained along the scanning direction, the plane strain assumption is taken. The liquidus and solidus temperatures are assumed to be 890 K and 900 K, respectively, and the reference temperature is 1000 K. The coefficient c is set to 10. The aspect ratio of the melting pool equals 1.0, with parameters l_L, l_S, d_L and d_S to be 3.5 mm, 4.0 mm, 7.0 mm and 8.0 mm. All material properties for the simulations are listed in Table. 3.3. The normalized temperature field obtained from the

interpolated solution is shown in Fig. 5.4(a), with the two lines indicating the liquidus and solidus temperatures, respectively. The predicted hot cracking patterns with the increasing solidification shrinkage strain are presented in Fig. 5.4(b)-(d). When the solidification shrinkage strain is not considered ($\alpha_{SS} = 0$), a low level of damage is observed only in the central region of the melting pool where the temperature is quite high. Outside these regions, there is no damage, as shown in Fig. 5.4(b). As the value of solidification shrinkage increases ($\alpha_{SS} = 4\alpha_t$), as shown in Fig. 5.4(c), a circumferential crack starts to form. This type of crack is mainly localized in the regions where the temperature is between the interval of the liquidus and solidus isotherms (see also the temperature field profile). As illustrated above, the material goes through a phase transformation in this temperature range, which causes volume change and relatively larger solidification shrinkage strain, when compared with thermal strain in other regions. When the solidification shrinkage strain is significant enough ($\alpha_{SS} = 26.7\alpha_t$), the circumferential crack is more prominent, as shown in Fig. 5.4(d). The latter observation is coherent with experimental results observed in the laser PBF process of alloys [134], as shown in Fig. 5.5.

To study the influence of the shape of the melting pool resulting from different AM process parameters, two more melting pools with larger (1.2) and smaller (0.5) aspect ratios are studied. For the former, the melting pool is deeper, which results from the larger energy density and it is often referred to as keyhole mode in AM [135]. For the latter where the energy density is smaller and thereby the melting pool is shallower, it is called conduction mode. The temperature field is obtained by the same method in Eq. 5.4, and the results are shown in Fig. 5.6. The crack patterns resemble those shown in Fig. 5.4(d), and only a circumferential crack is shown near the melting pool. From the results, it is obvious that solidification shrinkage is responsible for the circumferential hot cracking pattern. In this case, the central cracking is barely visible, which is attributed to the inaccuracy of the interpolated thermal profile introduced previously. The formation of a central crack due to a high energy density and the corresponding high thermal gradient will be further detailed in the following.

At this point, the result of the keyhole mode differs considerably from the experimental result observed in Fig. 5.5(a). Note that for this case, in addition to the circumferential crack, one observes a central crack as well. The disagreement of the crack pattern is the result of the way the temperature field is approximated, where the coefficient $c = 10$ in Eq. 5.4 for all cases. To investigate the influence of the temperature gradient near the melting pool, further studies with different values for the parameter c ($c = 20, 25$) are conducted. The approximated normalized temperature profiles and corresponding crack patterns are shown in Fig. 5.7.

Compared with the results of the temperature field and crack pattern in Fig. 5.4(a) and (d) with $c = 10$, it becomes clear that by increasing the parameter c , the temperature

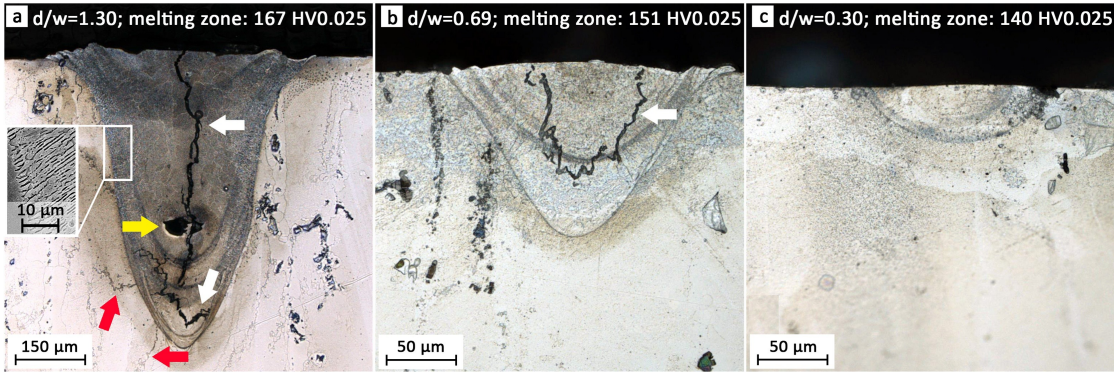


Figure 5.5: Hot cracking of single track of PBF with different power densities in experimental observations. The image is reprinted from [134] under the terms of the Creative Commons CC-BY license.

field has a similar distribution with the temperature gradient increasing accordingly. As a result, the crack pattern also changes. The damage level near the center of the melting pool increases, meaning that a central crack begins to show apart from the circumferential crack. However, because of the simple linear interpolation of temperature, the central region has the same relatively larger temperature gradient in all directions, contributing to cracks showing up in a very diffusive region. Again, the latter observation does not fully agree with the experimental results in Fig. 5.5. This implies the necessity of having a more accurate temperature profile, which will be considered in the following subsection.

5.3 Hot cracking in Powder Bed Fusion model

5.3.1 Hot cracking in the phenomenological model of PBF

The interpolated thermal profile has limited accuracy and does not allow parameter study on process conditions. In this subsection, the numerical thermal profile calculated from the phenomenological thermal PBF model developed in [136, 137] is utilized as the initial temperature distribution before it cools down to room temperature. In the phenomenological thermal PBF model, the effective thermal properties of the powder bed and the resolidified phase are regarded explicitly. A phase indicator ϕ is introduced to indicate the state of the material, i.e., $\phi = 1$ for the fused state and $\phi = 0$ for the powder bed. Readers are referred to [136, 137] for more details. Considering the phase-dependent thermal properties and the beam energy deposition, the heat transient problem is solved

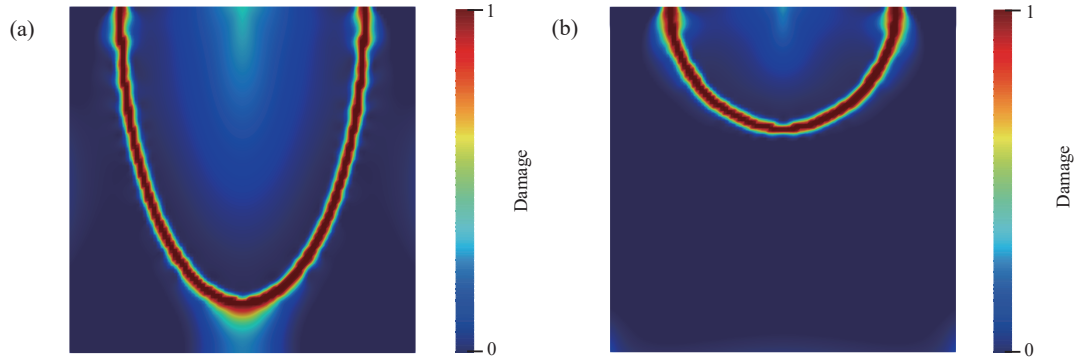


Figure 5.6: Hot cracking patterns of a single track of PBF with different shapes of the melting pool. (a) Keyhole mode with an aspect ratio of 1.2. (b) Conduction mode with an aspect ratio of 0.5.

using the finite element method.

In this simulation, the domain has a volume of $1000 \text{ mm} \times 400 \text{ mm} \times 200 \text{ mm}$, with a 50-mm-thick powder bed layer and a 150-mm-thick substrate layer made of the same solid materials as the powder, as shown in Fig. 5.8. All the outer surfaces except the bottom surface of the powder bed are subject to convection and radiation boundary conditions, while the Dirichlet boundary condition is applied to the bottom surface, i.e., the temperature is fixed. Meanwhile, the displacements in the x , y and z directions of the bottom surface are fixed, while all other surfaces are traction-free. The laser power (P) is $P_0 = 200 \text{ W}$ and the scanning speed (v) is $v_0 = 2000 \text{ mm/s}$. The material used for the LPBF process is SS316L, and its material properties are listed in Table 5.1 [136]. The other parameters used for this part are referred to the work [136].

Table 5.1: Temperature-dependent mechanical properties of SS316L

$\theta(\text{K})$	298	873	1073	1473	1623	≥ 1773
$E(\text{MPa})$	2.0×10^5	1.35×10^5	7.75×10^4	1.21×10^4	6.14×10^3	200
ν	0.33	0.35	0.36	0.38	0.39	0.40
$\sigma_Y(\text{MPa})$	345	212	199	100	50	5
$H(\text{MPa})$	6.07×10^3	1.72×10^3	1.43×10^3	101	10	1
$\alpha(1/\text{K})$	1.2×10^{-5}	1.3×10^{-5}	1.32×10^{-5}	1.36×10^{-5}	1.38×10^{-5}	1.40×10^{-5}

In Fig. 5.8, the snapshots of the temperature field and the phase indicator evolution

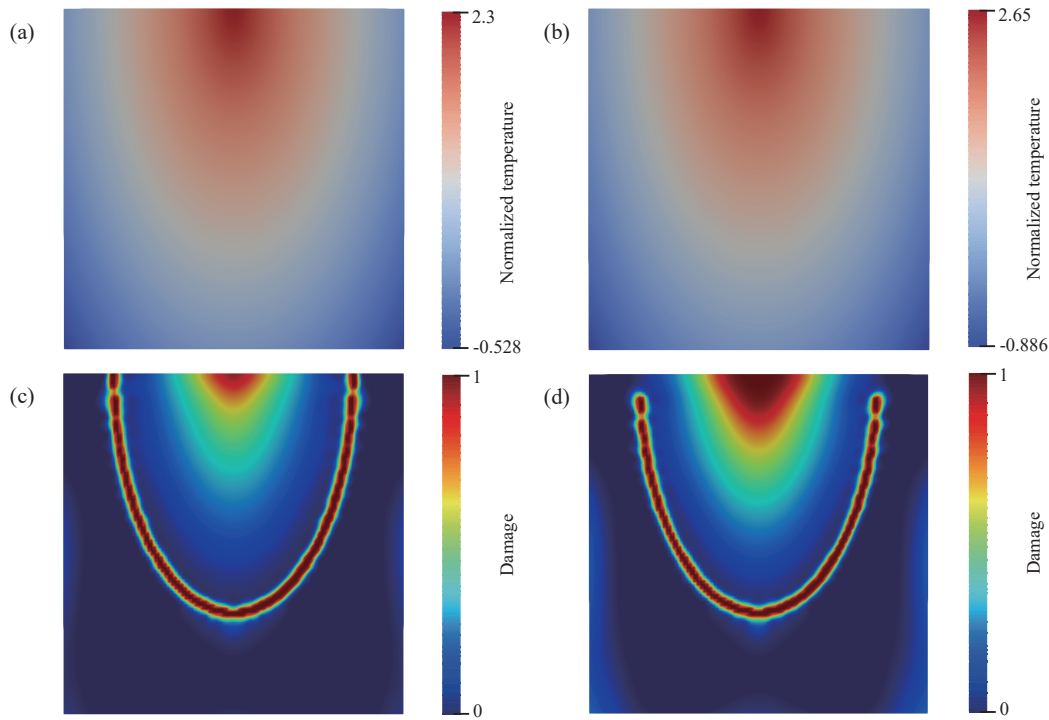


Figure 5.7: Normalized temperature profiles and hot cracking patterns of a single track of PBF with different temperature gradients c . (a) $c = 20$. (b) $c = 25$.

of the 3D phenomenological PBF model are shown. As the heat source (laser beam) moves forward (z) like a laser beam, the temperature near the beam increases to the melting temperature, and the powders melt and solidify to the substrate. This process is reflected by the phase indicator ϕ changing from blue (0) to red (1). The snapshots of the temperature field and the phase indicator evolution of the slice along the scanning direction are also shown in Fig. 5.8. As the laser approaches this slice, the temperature increases and the powders melt. As the beam moves away, the temperature drops while the materials remain in the fused state.

After obtaining the steady-state cross-sectional thermal profile and also the phase indicator distribution around the melt pool perpendicular to the scanning direction (z), they are transferred as the initial conditions for the subsequent hot cracking simulation. In the hot cracking simulation, a 2D plane strain case is assumed as the cross section is more or less mechanically constrained along the scanning direction. The bottom edge is

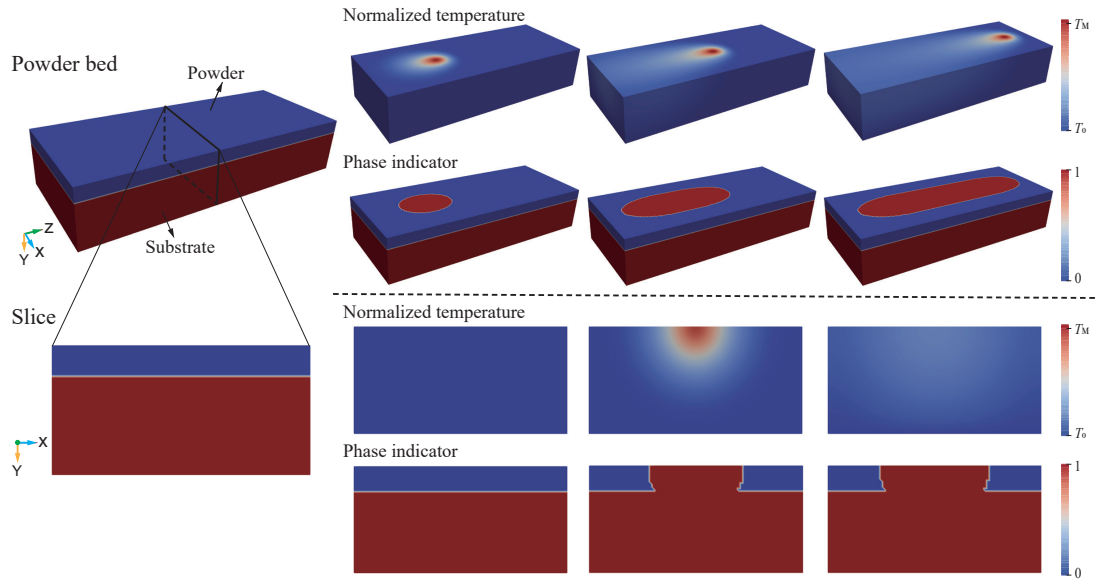


Figure 5.8: The temperature field and phase indicator evolution of the 3D phenomenological PBF model (top) and the cross-section perpendicular to the scanning direction (bottom).

fixed in the vertical direction (y), while the other edges are assumed to be traction-free. Similar to the previous subsection, the solidification shrinkage is also considered.

To study the influence of process parameters like laser power and scanning speed on the hot cracking pattern, some parameter analyses are conducted. Fig. 5.9 shows the different temperature profiles and the corresponding hot cracking patterns with varying laser power P and fixed v_0 . When the laser power is low ($P = P_0$), with the solidification shrinkage considered in the current model, only circumferential crack forms near the melting pool. In addition, a relatively low level of damage is also observed in the central region. Interestingly, this conduction mode hot cracking pattern predicted by numerical simulation is confirmed by the experimental observation of the conduction mode hot cracking, as shown in Fig. 5.5(b). With the laser power increased to $2P_0$, the damage level of the central region increases, and the central crack also arises, shifting the hot cracking pattern from the conduction mode to the keyhole mode. Meanwhile, the circumferential crack expands outwards. The reason is the increase in the maximum and overall temperature of the melting pool, and the temperature interval of the solidus and liquidus temperature gets off the center. When the laser power is further increased ($P = 3P_0$), the damage level

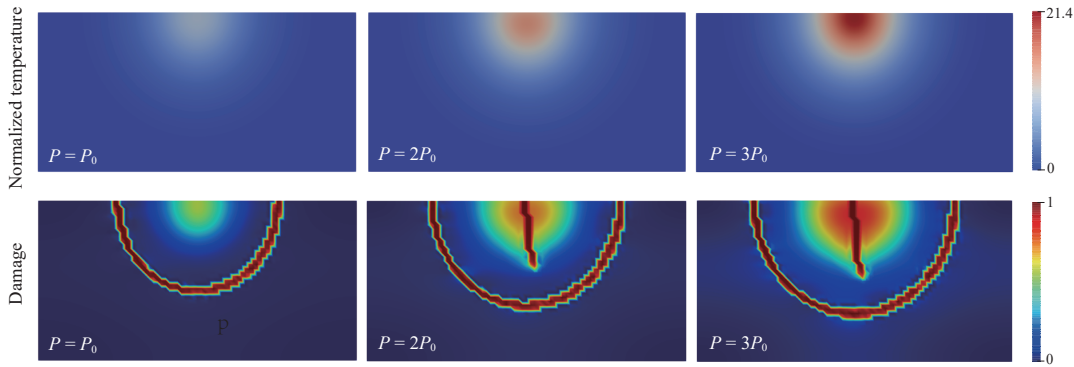


Figure 5.9: Hot cracking patterns of a slice of PBF with different laser powers.

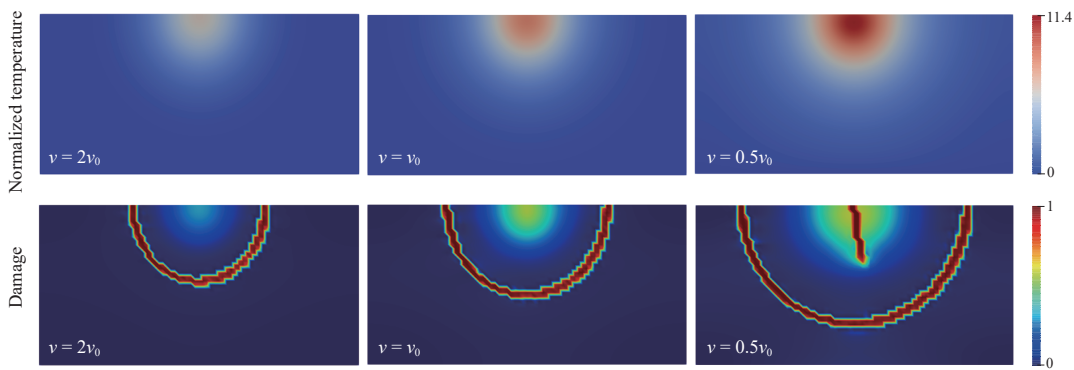


Figure 5.10: Hot cracking patterns of a slice of PBF with different scanning speeds.

in the central region becomes even larger, and the central crack also shows up. Note that the simulations with temperature-dependent elastic modulus under different laser powers were also performed and the results are provided. A similar phenomenon is observed in the cases of constant elastic modulus and a similar conclusion can be drawn.

The influence of the scanning speed v is also studied, with fixed P_0 , the results of which are depicted in Fig. 5.10. As discussed in the last paragraph, only the circumferential crack shows up in the melting pool when $v = v_0$. As the scanning speed decreases from v_0 to $0.5v_0$, more energy is input into the domain, causing the temperature and its gradient to increase. Therefore, the damage level in the central region is increased, and a central crack also appears, apart from the expanded circumferential crack, leading to the keyhole mode hot cracking. However, the hot cracking pattern tends to be the conduction mode

when the scanning speed increases. The reason is that the material absorbs less energy with high scanning speed. Accordingly, the temperature field and its gradient are reduced, and the damage level in the central region also decreases. Therefore, only the contracted circumferential crack forms near the melting pool.

In the current literature on AM process simulation, especially with the focus on the calculation of stress and displacement field, the widely-used method to simulate material behavior during melting and solidification is using temperature-dependent material properties, for example, see [138, 139, 140]. The material properties like elastic modulus normally decrease with the temperature. When the temperature is above the melting temperature, it's assumed to be degraded as a constant value to avoid numerical convergence issues. Another possible way to deal with this issue is to forcefully remove the thermal expansion or set the strain to zero when the phase becomes liquid. However, there are also some works that use constant material properties for simplicity, see [133, 141]. In this Chapter, the constant material properties are first assumed. Meanwhile, the extension to the temperature-dependent properties doesn't have a significant influence on the simulation results. The current work focuses on thermo-mechanical coupling and explores its preliminary application on hot cracking during PBF. While it's true that the elastic framework doesn't hold when the temperature exceeds the liquidus temperature, it should be noted that in any case, they share some common thermo-mechanical coupling mechanisms, which is the objective of this work.

To illustrate this point, the simulations with temperature-dependent properties under different laser power are performed here. Based on the dependence of Young's modulus on the temperature in the work of [112], here we take the form as Eq. 5.6, and after melting temperature, a residual value still exists.

$$E = E_0 \left[1 - c_1 \frac{\theta - \theta_{ref}}{\theta_{max}} - c_2 \left(\frac{\theta - \theta_{ref}}{\theta_{max}} \right)^2 \right]. \quad (5.6)$$

where $c_1 = 0.2$ and $c_2 = 0.25$, θ_{ref} and θ_{max} are the reference temperature and the maximum temperature, respectively. Moreover, E_0 is the value of E at θ_{ref} .

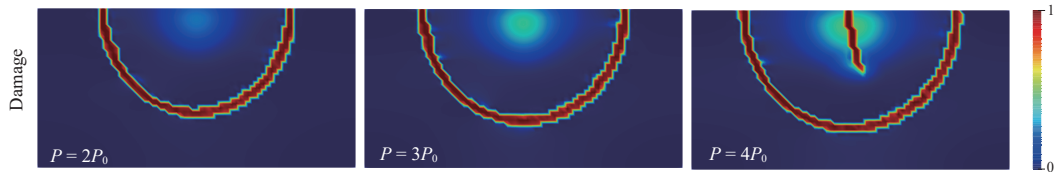


Figure 5.11: Hot cracking patterns of a slice of PBF with temperature-dependent mechanical properties under different laser powers.

The result in Fig. 5.11 shows that with the increase of the laser power, the hot cracking pattern changes from conduction mode to keyhole mode. This is in line with the conclusion that is reached for the cases with constant material properties. Compared with Fig. 5.9, the simulation results with/without temperature-dependent mechanical properties are quantitatively different. Nevertheless, the trend of the influence of the process parameter, i.e. laser power remains as before. In other words, with larger laser power and slower scanning speed, the hot cracking pattern tends to be the keyhole mode, and with smaller laser power and quicker scanning speed, the hot cracking pattern tends to be the conduction mode.

The reasons for different hot cracking patterns under different process parameters are related to energy deposition and thus to the thermal gradients. The laser power and the scanning speed determine the linear energy density $E_L = P/v$, which further determines the input energy to the PBF system. With larger laser power and slower scanning speed, E_L becomes larger, and the temperature gradient near the melting pool is enhanced as well. Therefore, a larger thermal strain is formed and drives the crack to develop. The hot cracking pattern tends to be the keyhole mode. On the contrary, with smaller laser power and quicker scanning speed, E_L becomes smaller, and the temperature gradient is lower. Correspondingly, the hot cracking pattern tends to be the conduction mode. These results are also in agreement with previous discussions. The comparisons between the numerical and experimental results above demonstrate that the currently proposed modeling strategy has the potential to predict hot cracking in the PBF and other AM processes. This study also provides some basic instructions on AM practices to eliminate the hot cracking of AM products.

For the 3D simulation, a domain of $1000 \times 400 \times 200 \mu\text{m}^3$ with a $50\text{-}\mu\text{m}$ -thick powder bed layer, and a $150\text{-}\mu\text{m}$ -thick substrate made of the same material is considered. The material used for the LPBF process is SS316L with its material properties listed in Table. 5.1. The powder bed is pre-heated to a preheating temperature $\theta_0 = 0.4\theta_M = 680 \text{ K}$. Both the mechanical and thermal material properties are linearly interpolated between the fused solid and the powders temporally and spatially. All the outer surfaces except the bottom surface of the powder bed are subject to convection and radiation boundary conditions. In contrast, the bottom surface is applied with the Dirichlet boundary condition, i.e., the temperature is fixed. For the mechanical boundary conditions, the bottom surface is fixed, and all other surfaces are traction-free.

Fig. 5.12 presents the evolutions of temperature and phase indicator of two phenomenological LPBF processes. The process parameters are $P = 200 \text{ W}$, $v = 1000 \text{ mm s}^{-1}$ and $P = 100 \text{ W}$, $v = 2000 \text{ mm s}^{-1}$, respectively. As the laser beam moves forward, the temperature of the powder near the beam increases to the melting temperature θ_M , and the powders melt. After the beam moves away, these regions cool down below θ_M and then resolidify

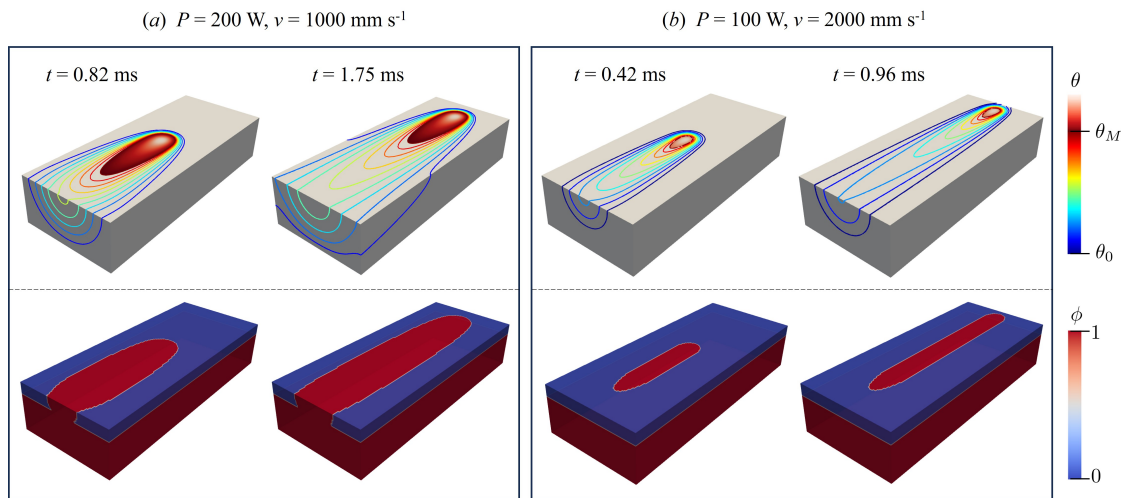


Figure 5.12: Temperature (top) and phase indicator (bottom) evolution of two phenomenological LPBF processes. (a) $P = 200 \text{ W}$, $v = 1000 \text{ mm s}^{-1}$; (b) $P = 100 \text{ W}$, $v = 2000 \text{ mm s}^{-1}$. The melting pool and fused zone are enlarged with higher laser power and slower scanning speed.

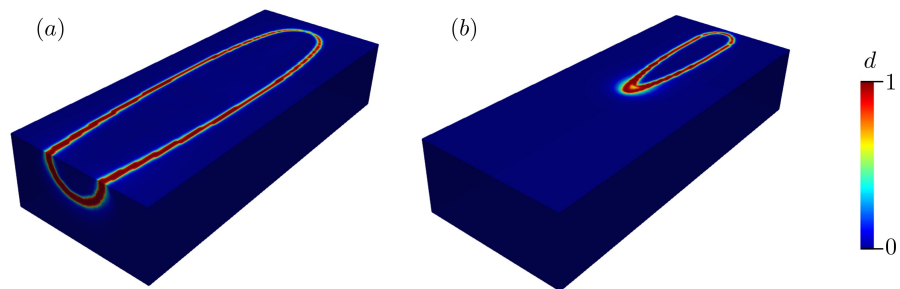


Figure 5.13: Hot cracking patterns of two phenomenological LPBF processes with (a) $P = 200 \text{ W}$, $v = 1000 \text{ mm s}^{-1}$ and (b) $P = 100 \text{ W}$, $v = 2000 \text{ mm s}^{-1}$.

to the substrate. This process is reflected by the phase indicator ϕ changing from blue (0) to red (1). The materials remain as fused solid after the laser moves away. With larger laser power and slower scanning speed, more energy is absorbed into the system so that the temperature of more powders exceeds the melting temperature, therefore the melting pool is enlarged.

The hot cracking patterns at the terminal stage of the process for the two LPBF processes

are shown in Fig. 5.13. With higher laser power and slower scanning speed, the energy input into the system is higher, according to the linear energy density $E_L = P/v$. Therefore, the melting pool size is enlarged with higher E_L . At the terminal stage of solidification, hot cracking occurs in the vicinity of the melting pool as a result of the solidification shrinkage.

5.3.2 Hot cracking in the powder-resolved model of PBF

Simulation setup of thermal fracture in LPBF

Utilizing the phenomenological LPBF model is both easy to implement numerically and computationally efficient. However, it neglects the complex morphology of the powder bed and assumes homogenized material properties. The thermo-microstructural interaction is not considered for simplicity, and thus the thermal field and microstructural evolution is not very precise. Therefore, applying the proposed thermal fracture model to a more high-fidelity powder-resolved LPBF model can deliver unique results that the phenomenological LPBF model cannot, based on the non-isothermal phase-field model proposed in [142, 143, 144]. For this model, heat transfer is strongly coupled with microstructure evolution driven by diffusion and grain growth, while the mechanical influence on the thermal field is trivial. Therefore only one-way coupling is considered here, i.e., we assume the heat conduction is not influenced by mechanics.

The workflow of the hot cracking simulation in the LPBF process is summarized in Fig.5.14, which consists of three procedures. First, the powders subject to the gravitational force are deposited on the substrate within a certain simulation domain based on the discrete element method (DEM). Then, the non-isothermal phase-field simulations under particular process parameters are performed, from which the coupled thermo-microstructural evolution during the LPBF process is obtained. Upon scan completion of one layer, the resulting microstructure is voxelized and reimported back to the DEM program for the deposition of the next layer of powders until the final layer is deposited. Finally, the thermo-elasto-plastic coupled ductile fracture simulations are performed to investigate the evolution of the mechanical and damage field of the thermo-microstructures by mapping the nodal values of the transient temperature and the order parameters of each calculation step from the previous procedure. The transient thermal field is imported as the thermal load, and the order parameter is to indicate the chronological-spatial distribution of the material phases and the interpolation of mechanical properties. This mapping is achieved by the `SolutionUserObject` and associated functions embedded in MOOSE. The detailed descriptions of the non-isothermal phase-field model of LPBF are skipped here for the brevity of this work. The interested readers are referred to the work

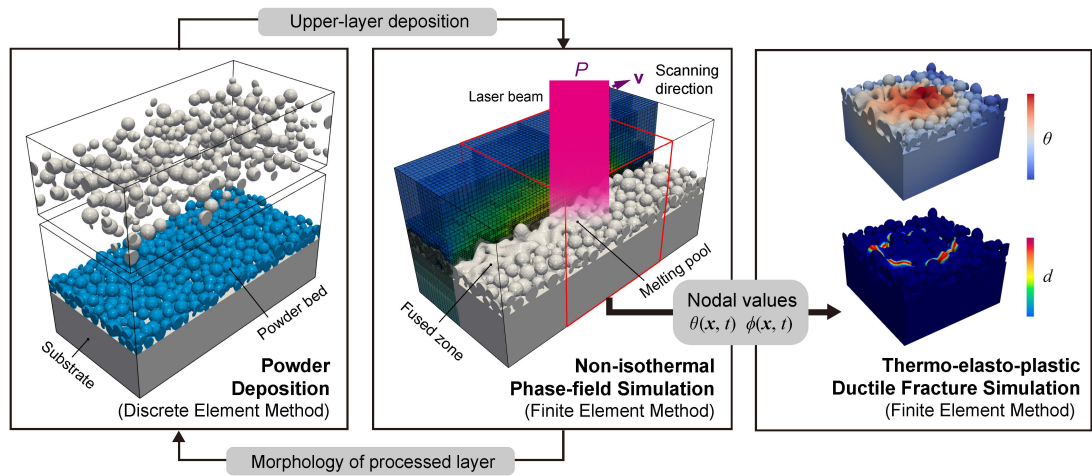


Figure 5.14: Workflow of hot cracking simulations in non-isothermal phase-field model for LPBF, including the powder deposition, the non-isothermal phase-field simulation and the thermo-elasto-plastic ductile fracture simulation.

[142] for more details.

For the simulations in this section, a $250 \times 250 \times 250 \mu\text{m}^3$ domain containing $100 \mu\text{m}$ -thick substrate and a layer of powders is considered. LPBF processes of a single layer and single scanning pass are simulated. The process parameters, including laser beam diameter, beam power P and a scanning speed v are kept constant throughout one LPBF process. Both the powders and the substrate are SS316L, with the melting temperature $\theta_M = 1700 \text{ K}$. The processing window with $P \in [25, 30] \text{ W}$ and $v \in [75, 100] \mu\text{m s}^{-1}$ is selected.

For the non-isothermal phase-field simulations, the powder bed is pre-heated to a preheating temperature $\theta_0 = 0.4\theta_M = 680 \text{ K}$, which is embodied by temperature initial condition and boundary condition. $\partial\Omega_T$ and $\partial\Omega_B$ are the top and bottom boundaries of the simulation domain, respectively, and $\partial\Omega_S$ is the set of all surrounding boundaries, as $\partial\Omega = \partial\Omega_T \cup \partial\Omega_B \cup \partial\Omega_S$. The BCs are imposed as follows: $\partial\Omega_T \cup \partial\Omega_S$ are subject to the heat convection and heat radiation, while $\partial\Omega_B$ is enforced with Dirichlet conditions θ_0 . For the thermo-elasto-plastic ductile fracture simulations, the displacements along the normal direction of all but the top boundaries are restricted while the top surface is traction-free. The mechanical properties are linearly interpolated between the fused solid materials and the pores temporally and spatially.

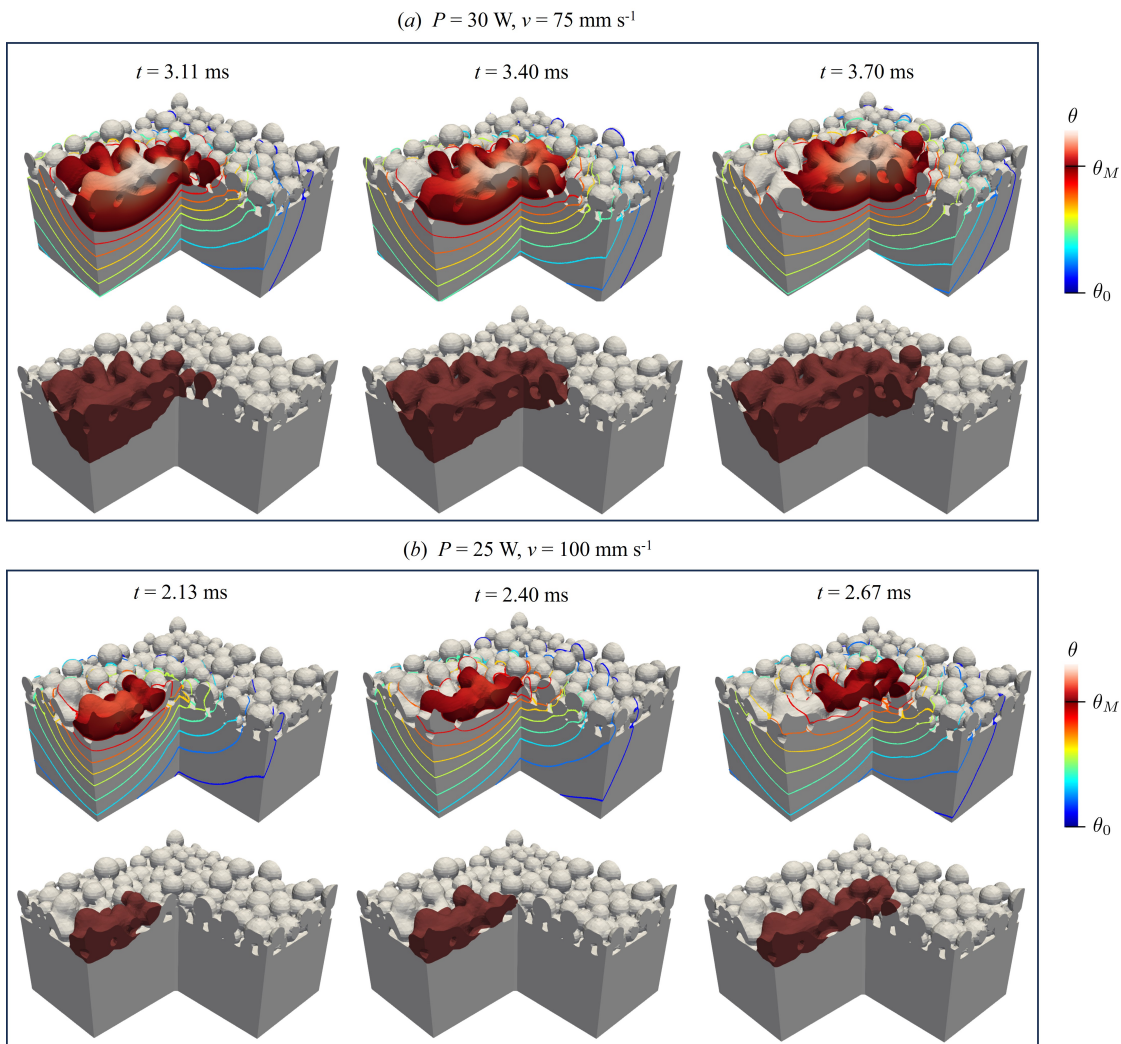


Figure 5.15: Evolution of thermal-structure morphology during two non-isothermal phase-field models of LPBF. (a) $P = 30 \text{ W}, v = 75 \text{ mm s}^{-1}$ at $t = [3.11, 3.40, 3.70]$ ms and (b) $P = 25 \text{ W}, v = 100 \text{ mm s}^{-1}$ at $t = [2.13, 2.40, 2.67]$ ms. The upper rows show the temperature profiles and the lower rows show structural morphology.

Thermal fracture in LPBF

Following the simulation scheme, the non-isothermal phase-field simulations of LPBF are first performed. In Fig. 5.15, the simulation results of the thermal-microstructural evolution during LPBF with $P = 30 \text{ W}$, $v = 75 \text{ mm s}^{-1}$ at $t = [3.11, 3.40, 3.70] \text{ ms}$ and $P = 25 \text{ W}$, $v = 100 \text{ mm s}^{-1}$ at $t = [2.13, 2.40, 2.67] \text{ ms}$ are shown, respectively. The laser beam spot is consistently positioned along the scan direction.

It shows that powders undergo complete or partial melting in the overheated regions where the temperature exceeds the melting temperature ($\theta \geq \theta_M$), which prompts molten materials to flow from convex to concave regions and form the fusion zone. Meanwhile, in regions where the temperature is lower than the melting point ($\theta \leq \theta_M$), the temperature is high enough to cause diffusion as the necking behaviors arise among neighbouring powders. Interestingly, the temperature profiles demonstrate a strong sensitivity to the local morphology. The concentrated temperature isolines are observed in the vicinity of the necking regions, which indicates a high level of temperature gradient. This thermal inhomogeneity induced by stochastic transient morphology can hardly be resolved by the phenomenological model in the previous work.

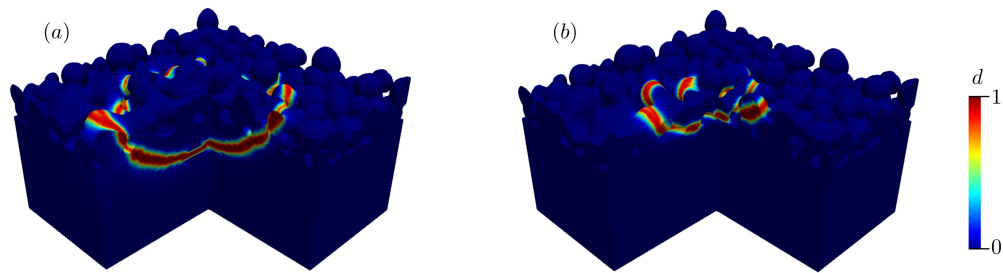


Figure 5.16: Hot cracking patterns for two powder-resolved non-isothermal phase-field models of LPBF (a) $P = 30 \text{ W}$, $v = 75 \text{ mm s}^{-1}$ and (b) $P = 25 \text{ W}$, $v = 100 \text{ mm s}^{-1}$. Crackings are located near the melting pool boundaries due to the solidification shrinkage.

The thermo-structural evolution of the powder bed is significantly affected by the process parameters, as shown by the profiles with varying beam power and scan speed. Comparing the two rows, it is apparent that heat accumulation is intensified, and the melting pool is enlarged with higher laser power and lower scan speed. A more detailed description of the thermo-structural evolution process is referred to [142].

After the non-isothermal phase-field simulations are completed, the thermo-microstructural evolution results are imported into the present thermo-ductile fracture model. To model

the mechanical behavior of the powders after melting, the fracture simulation starts when the materials have cooled down to the melting temperature. Fig. 5.16 shows the hot cracking patterns with different laser power and scanning speed during LPBF.

The hot cracking patterns are in line with those of Sec.5.3.1. In the regions near the melting pool boundaries, the powders cool down from maximum temperature to temperature below melting temperature. The solidification shrinkage takes effect during the liquid-solid phase transition and leads to hot cracking near the boundaries. Interestingly, the cracks are more likely to initiate in the necking regions between powders, corresponding to the thermal profiles.

6 Phase-field Anisotropic Fracture of Additively Manufactured Parts

6.1 Introduction

AM has emerged as a revolutionary manufacturing technology and gained widespread applications in many fields in recent decades. However, it is susceptible to process-induced defects, notably pores and microcracks, which compromise the integrity of the final products. These defects, as outlined by [145], can be categorized into three main types: porosities, melting-related defects, and cracks, each with distinct characteristics stemming from the intricate layer-by-layer fusion process. Experimental investigations of LPBF have identified various forms of porosity, including lack-of-fusion, keyhole, and gas porosities, while cracks are primarily attributed to rapid cooling, the induced sharp thermal gradients and thermal stresses, and solidification shrinkage. Consequently, an inadequately optimized combination of the process parameters often yields porous components, undermining their mechanical properties and overall performance. A detailed review of the effects of the process-induced defects on the mechanical properties is referred to [146].

Due to the layered heterogeneous microstructure induced by the building process, the AM parts exhibit anisotropic responses in the overall material behaviors. Their mechanical properties and performances depend significantly on the AM process, e.g., the way the parts are placed and the loading conditions, as illustrated in Fig. 6.1. Zou et al. [148] elucidated the anisotropic elasticity and yielding of 3D-printed acrylonitrile butadiene styrene (ABS) with different printing orientations. The anisotropic fracture patterns are shown in Fig. 6.2. Though many experiments to characterize the anisotropic mechanical behaviors of AM parts have been performed, there is still limited numerical research to study the anisotropic fracture behaviors.

Phase-field modeling of fracture has established itself as a robust, efficient, and versatile tool to solve fracture problems in the recent decade. The phase-field modeling of brittle fracture originated from the work by Francfort and Marigo [57]. They proposed a phase-field fracture model from the variational approach to brittle fracture by reformulating Griffith's energy criterion [53]. It aimed to get the displacement field and fracture field

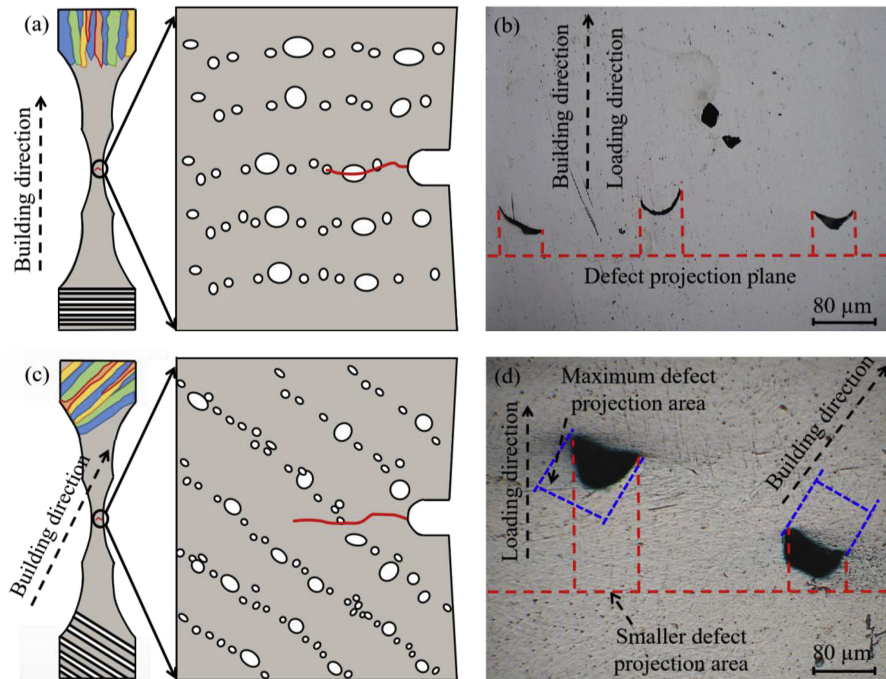


Figure 6.1: Effect of internal defects on the crack propagation of AM samples. (a) and (c) Influence of orientations of specimens on the interlayer pore distribution, (b) and (d) Defects distribution in 90° and 45° samples, respectively. Figure adapted from [147].

simultaneously by minimizing the total potential energy as the sum of the fracture energy and elastic energy of the crack system. Karma et al. [149] proposed a conceptually similar phase-field approach to brittle fracture based on the classical Ginzburg-Landau evolution equation. The numerical implementation of the brittle fracture model was developed in [57] and [59], see also [61, 62]. Phase-field fracture model has the flexibility to simulate crack initiation, propagation, merging as well as branching, and thereby has been extended to various fracture problems, such as ductile fracture [81, 83, 150], anisotropic fracture [70, 71] and multiphysics fracture problems [94, 99, 151].

Most existing phase-field fracture models assume crack evolution within isotropic solids. However, this assumption does not apply to many materials and structures that exhibit orientation-dependent mechanical behavior, like AM parts. Therefore, taking anisotropy into the fracture model is necessary to capture the fracture patterns in these scenarios

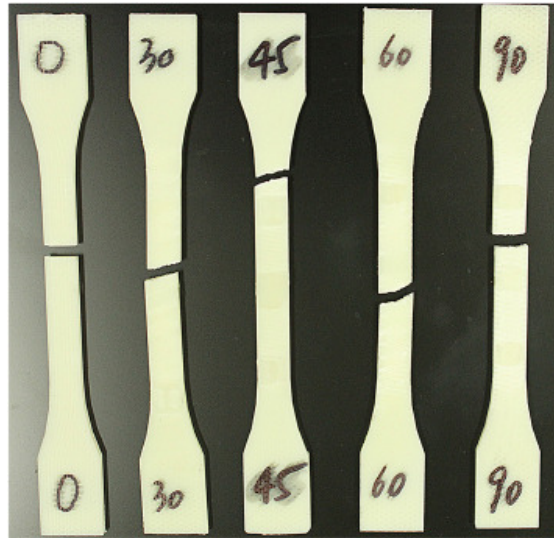


Figure 6.2: Experimental testing of anisotropic fracture of additively manufactured parts. The crack patterns with layer orientations 0° , 30° , 45° , 60° , 90° [148]. Figure reproduced from [148].

accurately. Phase-field modeling of anisotropic fracture was first introduced in [152] by combining the classical variational phase-field model of brittle fracture with the extended Cahn-Hilliard framework. However, the contribution of compressive stress to crack was also considered in this model. Teichtmeister et al. [153] included anisotropy into the phase-field fracture model by pure geometrical approach and structural tensors, separately, see [154, 155, 156, 157] as well for structural tensor approach. Further, phase-field modeling of anisotropic fracture for polycrystal materials was extended by, e.g., [158, 159, 160, 161] using single damage variable, and multi-phase-field variables [162, 163, 164, 165] where every variable is associated with a preferential cleavage direction. Likewise, investigations on phase-field models for anisotropic fracture in composite materials are performed [166, 167].

However, all the models above only consider the anisotropic fracture energy density and ignore the anisotropic elasticity. In the work [168], a phase-field fracture model was developed in the general framework of anisotropic elasticity. Nevertheless, anisotropic elasticity alone is not capable of well capturing anisotropic fracture behaviors [169, 170]. Zhang et al. [171] proposed a phase-field model of brittle fracture that accounts for any elastic anisotropy using spectral decomposition of the stress and avoids the impact of

compressive stress on crack propagation. Further, Zhang et al. [172] developed a model that includes single-crystal anisotropy in both the elastic constants and the fracture energy. Scherer et al. [173] proposed a similar framework where an anisotropic degradation of the elasticity stiffness tensor is also considered. See also the works [174, 175].

Interestingly enough, though the phase-field modeling of anisotropic fracture has been investigated extensively in the materials system aforementioned, the applications to AM parts that show significant anisotropy experimentally [148] are still rather scanty. Khosravani et al. [70] studied the anisotropic fracture behaviors of polylactic acid material (PLA) fabricated via extrusion-based 3D printing both numerically and experimentally. However, the printed specimens are treated as homogenized solids in the numerical formulation. Li et al. [176] proposed a phase-field model for anisotropic fracture of 3D printed materials with two phase-field variables representing bulk damage and microscale interfacial damage, respectively, but the contribution of compressive stress on crack propagation was not excluded, and the effects of anisotropic elasticity and anisotropic fracture property were not discussed as well. Based on the literature reviewed, this Chapter aims to develop an anisotropic phase-field model for AM materials based on the computational homogenization and spectral decomposition of stress and strain energy. The model considers both anisotropic elastic and fracture properties, with their influences on fracture behaviors of AM parts compared comprehensively.

6.2 Phase-field modeling of anisotropic fracture

To analyze the anisotropic material behaviors of AM parts, a phase-field anisotropic fracture model is proposed. To this end, the elastic properties are constructed by the computational homogenization method, while the stress-based spectral decomposition method of stress and strain energy is utilized as a result of anisotropic elasticity. A structural tensor is introduced, which entails direction-dependent fracture energy to the phase-field fracture model. Note that the temperature is assumed to be fixed, thus the model is purely mechanical and no thermo-mechanical coupling is considered in this Chapter.

6.2.1 Phase-field model of anisotropic brittle fracture

Consider a cracked solid Ω with an external boundary denoted by $\partial\Omega$ and a crack set Γ . Starting from Griffith's theory [53] in fracture mechanics, the total fracture energy is given by

$$\psi_c = \int_{\Gamma} G_c dA = \int_{\Omega} G_c \gamma(d, \nabla d) dV, \quad (6.1)$$

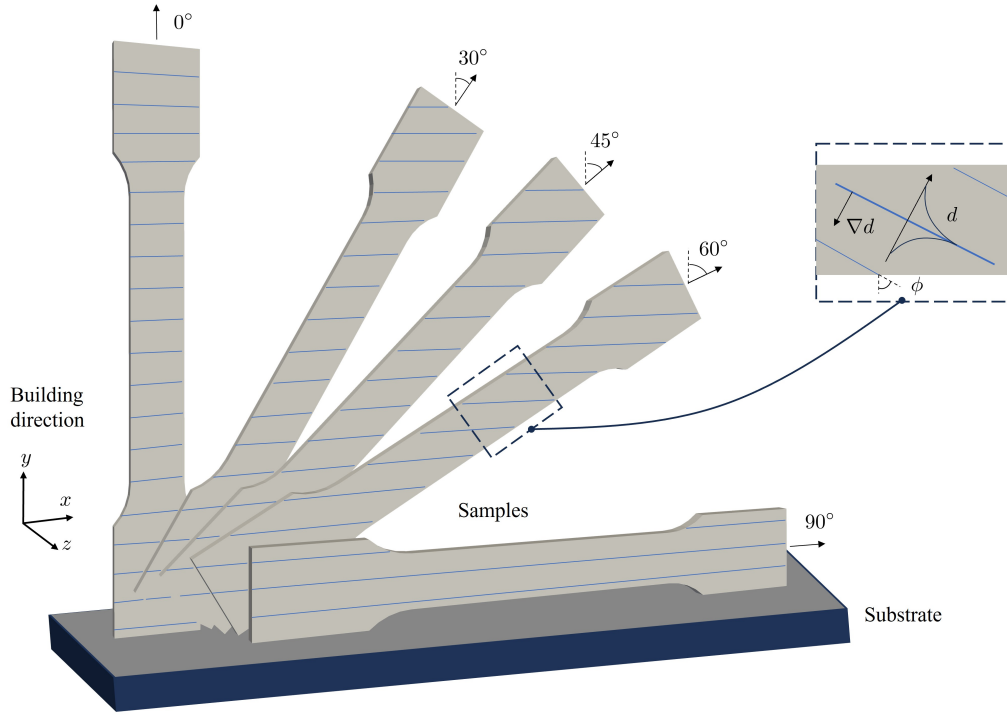


Figure 6.3: Schematic of the additively manufactured specimens with different orientations. The scanning direction in the x - z plane is isotropic, and the building direction is along y axis. Figure adapted from [148].

where G_c is the critical energy release rate. In the relation above, the surface integral is substituted with a volumetric integral, which approximates the fracture energy. Here, γ is the crack surface energy density defined as

$$\gamma(d, \nabla d) = \frac{1}{c_0} \left(\frac{1}{\ell_0} \omega(d) + \ell_0 \nabla d \cdot \mathbf{A} \cdot \nabla d \right), \quad (6.2)$$

where $c_0 = 4 \int_0^1 \sqrt{\omega(\alpha)} d\alpha$ is the scaling parameter dependent on the crack topology function $\omega(d)$. The second-order structural tensor \mathbf{A} is based on the orientation vector \mathbf{a} , and takes the form as

$$\mathbf{A} = \mathbf{I} + \beta \mathbf{a} \otimes \mathbf{a}, \quad \mathbf{a} = [\cos\phi, \sin\phi]^T, \quad (6.3)$$

where \mathbf{I} is the second-order unit tensor, the printing direction ϕ is defined as the angle between the principal axis of the specimen and the axis y of the printing platform, as

shown in Fig. 6.3. \mathbf{a} is the unit vector normal to ϕ . The scalar parameter β represents the degree of anisotropy and penalizes damage along the direction normal to \mathbf{a} . In the case of $\beta=0$, the anisotropic fracture recovers to the isotropic case.

In this work, the cohesive regularized phase-field fracture (CPF) model [106, 99] is employed to get rid of the length scale sensitivity of the fracture process. The crack geometric function and the degradation function are defined respectively as:

$$\begin{aligned}\omega(d) &= 2d - d^2, \\ g(d) &= \frac{(1-d)^2}{(1-d)^2 + a_1 d(1 + a_2 d + a_3 d^2)},\end{aligned}\tag{6.4}$$

where $a_1 = \frac{4 l_{ch}}{\pi \ell_0}$, $a_2 = -\frac{1}{2}$ and $a_3 = 0$ are selected to represent the cohesive nature of fracture in the process zone. Furthermore, $l_{ch} = \frac{EG_c}{\sigma_u^2}$ is Irwin's length of isotropic materials which measures the size of the fracture process zone. The smaller this length scale is, the more brittle the material behaves. The parameters a_2 and a_3 are the shape parameters and can be tuned to represent the different softening curves.

To differentiate degradation in tension from compression, the elastic strain energy density ψ_e is additively decomposed into a positive (tensile) part ψ_e^+ and a negative (compressive) part ψ_e^- , and only the positive part serves as the crack driving force.

$$\psi_e = g(d)\psi_e^+ + \psi_e^-. \tag{6.5}$$

Here, $g(d)$ is the degradation function defined in Eq. 6.4. To avoid cracks healing when ψ_e^+ decreases, the irreversibility condition is enforced. According to [64], a history variable is defined following the Karush-Kuhn-Tucker (KKT) conditions

$$\psi_e^+ - \mathcal{H} \leq 0, \quad \dot{\mathcal{H}} \geq 0, \quad \dot{\mathcal{H}} (\psi_e^+ - \mathcal{H}) = 0. \tag{6.6}$$

Thus, the history variable can be written as

$$\mathcal{H} = \max_{t \in [0, \tau]} \psi_e^+(\boldsymbol{\varepsilon}_e, t). \tag{6.7}$$

Employing the micro-force balance equation, the phase-field governing equation reads,

$$\frac{2G_c \ell_0}{c_0} \nabla^2 d - g'(d)\mathcal{H} - \frac{G_c}{c_0 \ell_0} \omega'(d) = 0. \tag{6.8}$$

The tensile and compressive parts of the elastic strain energy are defined as,

$$\psi_e^+ = \frac{1}{2} \boldsymbol{\sigma}^+ : \boldsymbol{\varepsilon}, \quad \psi_e^- = \frac{1}{2} \boldsymbol{\sigma}^- : \boldsymbol{\varepsilon}, \tag{6.9}$$

where σ^+ and σ^- are the tensile and compressive parts of the damaged stress.

The intact stress is calculated as

$$\sigma_0 = \mathbb{C} : \varepsilon, \quad (6.10)$$

where \mathbb{C} is the symmetric fourth-order elasticity tensor. In the context of anisotropic behaviors of the AM part, \mathbb{C} is calculated by a computational homogenization scheme, which is introduced in the following. Different ways of decomposition are utilized for isotropic materials, i.e., strain spectral decomposition [63], and strain volumetric-deviatoric decomposition [62]. For materials with anisotropic elasticity, neither method is applicable. Stress spectral split is used here to account for the anisotropic elasticity [171]. The intact stress is further decomposed as

$$\sigma_0 = Q\Lambda Q^T, \quad (6.11)$$

where $\Lambda = \mathbf{diag}(\sigma_1, \sigma_2, \sigma_3)$ is a diagonal tensor containing the three eigenvalues of the stress tensor (or the principal stress tensor), and $Q = [n_1, n_2, n_3]$ is the eigenvector tensor. From the principal stress tensor, the tensile and compressive parts are calculated as

$$\sigma^\pm = Q\Lambda^\pm Q^T, \quad (6.12)$$

where $\Lambda^\pm = \mathbf{diag}(\langle \sigma_1 \rangle_\pm, \langle \sigma_2 \rangle_\pm, \langle \sigma_3 \rangle_\pm)$. The two parts can also be expressed as

$$\sigma^\pm = P^\pm \sigma_0, \quad (6.13)$$

where the projection tensors are calculated from the spectral decomposition of the intact stress.

$$P^+ = \frac{\partial \sigma^+}{\partial \sigma_0}, \quad P^- = \mathcal{I} - P^+. \quad (6.14)$$

Therefore, the full fourth-order elasticity tensor is included. The cracked Cauchy stress reads

$$\sigma = g(d)\sigma^+ + \sigma^-, \quad (6.15)$$

The equation of the linear momentum balance, ignoring the body force is thus given,

$$\nabla \cdot \sigma = \mathbf{0}. \quad (6.16)$$

6.2.2 Effective elastic moduli based on computational homogenization

The effective elastic moduli of the heterogeneous materials are computed by computational homogenization. To make the Chapter reasonably self-contained and for the sake of clarity,

the procedure of computational homogenization with periodic boundary conditions is recapitulated here.

Essentially, a representative volume element (RVE) is extracted from a large domain, where an average displacement gradient or equivalently an average strain tensor is prescribed, and the elasticity partial differential equations are solved within the domain under periodic boundary conditions. The stress and strain fields are used to compute the average stress and strain values of the domain, and the effective elastic moduli are obtained. The elastic strain field can be decomposed into a constant macroscopic strain field $\bar{\varepsilon}$ and a microscopic fluctuation $\tilde{\varepsilon}$,

$$\varepsilon = \bar{\varepsilon} + \tilde{\varepsilon}, \quad (6.17)$$

where by definition

$$\int_{\Omega} \tilde{\varepsilon} = 0. \quad (6.18)$$

By periodic boundary condition, the displacement field $\mathbf{u}(\mathbf{x})$ over the boundary takes the form,

$$\mathbf{u}(\mathbf{x}) = \bar{\varepsilon}\mathbf{x} + \tilde{\mathbf{u}}(\mathbf{x}), \quad (6.19)$$

where the fluctuation $\tilde{\mathbf{u}}(\mathbf{x})$ is periodic, indicating the constraint for two homologous nodes on opposite boundaries of the RVE,

$$\mathbf{u}^+ - \mathbf{u}^- = \bar{\varepsilon}(\mathbf{x}^+ - \mathbf{x}^-). \quad (6.20)$$

To fully determine the effective stiffness matrix, three loading conditions with the following strain fields for 2D problems are prescribed.

$$\varepsilon_{ij}^{(1)} = \begin{bmatrix} a & 0 \\ 0 & 0 \end{bmatrix}, \quad \varepsilon_{ij}^{(2)} = \begin{bmatrix} 0 & 0 \\ a & 0 \end{bmatrix}, \quad \varepsilon_{ij}^{(3)} = \begin{bmatrix} 0 & a \\ a & 0 \end{bmatrix}, \quad (6.21)$$

where a is a constant strain value. For each loading case, one column of the effective stiffness tensor $\bar{\mathbb{C}}$ is obtained

$$\begin{aligned} \langle \boldsymbol{\sigma} \rangle_{ij}^{(1)} = \bar{\mathbb{C}}_{ijkl} \langle \boldsymbol{\varepsilon} \rangle_{kl}^{(1)} &\Rightarrow \bar{\mathbb{C}}_{ij11} = \frac{1}{a} \langle \boldsymbol{\sigma} \rangle_{ij}^{(1)}, \\ \langle \boldsymbol{\sigma} \rangle_{ij}^{(2)} = \bar{\mathbb{C}}_{ijkl} \langle \boldsymbol{\varepsilon} \rangle_{kl}^{(2)} &\Rightarrow \bar{\mathbb{C}}_{ij22} = \frac{1}{a} \langle \boldsymbol{\sigma} \rangle_{ij}^{(2)}, \\ \langle \boldsymbol{\sigma} \rangle_{ij}^{(3)} = \bar{\mathbb{C}}_{ijkl} \langle \boldsymbol{\varepsilon} \rangle_{kl}^{(3)} &\Rightarrow \bar{\mathbb{C}}_{ij12} = \frac{1}{2a} \langle \boldsymbol{\sigma} \rangle_{ij}^{(3)}. \end{aligned} \quad (6.22)$$

Thus, $\bar{\mathbb{C}}$ has the form

$$\bar{\mathbb{C}} = \begin{bmatrix} \bar{\mathbb{C}}_{1111} & \bar{\mathbb{C}}_{1122} & \bar{\mathbb{C}}_{1112} \\ \bar{\mathbb{C}}_{2211} & \bar{\mathbb{C}}_{2222} & \bar{\mathbb{C}}_{2212} \\ \bar{\mathbb{C}}_{1211} & \bar{\mathbb{C}}_{1222} & \bar{\mathbb{C}}_{1212} \end{bmatrix}. \quad (6.23)$$

For any arbitrary coordinate system $x' - y'$ rotating from the reference coordinate system $x - y$ with angle θ , the effective stiffness tensor is given

$$\bar{\mathbb{C}}' = \mathbf{Q} \bar{\mathbb{C}} \mathbf{Q}^T, \quad (6.24)$$

where

$$\mathbf{Q} = \begin{bmatrix} \cos^2\theta & \sin^2\theta & 2\cos\theta\sin\theta \\ \sin^2\theta & \cos^2\theta & -2\cos\theta\sin\theta \\ -\cos\theta\sin\theta & \cos\theta\sin\theta & \cos^2\theta - \sin^2\theta \end{bmatrix}. \quad (6.25)$$

6.3 Numerical example: fracture of single-edge notched specimen

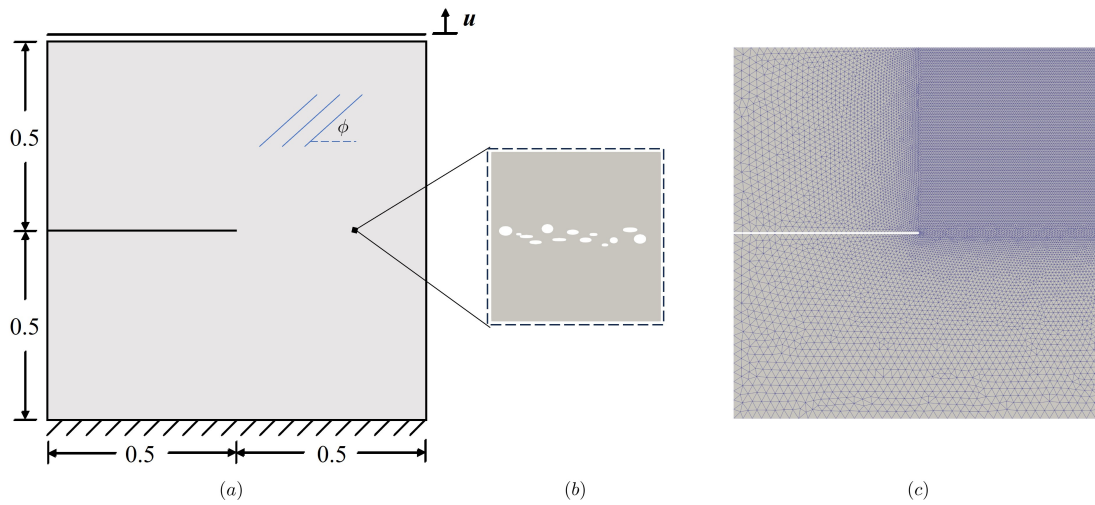


Figure 6.4: Single-edge notched tension test. (a) Geometry and boundary conditions of the specimen, (b) Geometry of RVE, (c) Mesh of specimen.

The proposed model is first validated to show its capability to model anisotropic brittle fracture. To show the influence of the anisotropic elasticity and/or fracture properties

on fracture behaviors, several numerical examples are performed with the canonical single-edge notched tension test.

6.3.1 Mode I fracture with isotropic elasticity

To compare the influence of anisotropic properties, a phase-field fracture simulation of isotropic materials is performed first. As mentioned in Eq. 6.3, the isotropic fracture model is recovered by setting $\beta = 0$. The geometry and boundary conditions are shown in Fig. 6.4(a), where the bottom edge is fixed while a vertical displacement is applied to the top edge. Fig. 6.4(b) presents the chosen RVE which contains pores and microcracks. The domain is discretized into the unstructured mesh with refined regions ($h=0.005$ mm) where the cracks are expected to propagate to ensure the phase-field variable is well resolved, as shown in Fig. 6.4(c). The material properties used for the simulations are Young's modulus $E = 340$ GPa, Poisson's ratio $\nu = 0.22$, fracture toughness $G_c = 4.247$ J/m². The length scale parameter l_c is 0.015 mm.

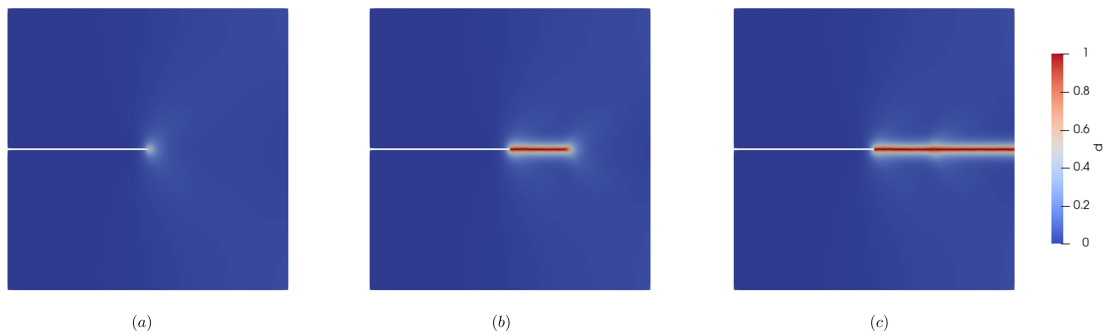


Figure 6.5: Crack evolution of Mode I fracture of isotropic materials at timesteps $186\mu s$, $187\mu s$, $188\mu s$.

The crack evolution at time $186\mu s$, $187\mu s$, $188\mu s$ for mode I fracture are shown in Figs. 6.5(a)-(c), respectively. Due to the isotropic material properties and boundary conditions, the crack initiates at the notch tip and propagates horizontally till fully broken.

6.3.2 Mode I fracture with anisotropic elasticity

In this section, the single-edge notched tension tests are performed with anisotropic elasticity, while the fracture property remains isotropic. Following the homogenization procedure in Section. 6.2.2, the effective elastic moduli, i.e., Young's modulus and Poisson's ratio are computed and shown in Figs. 6.6(a1) and (a2), respectively.

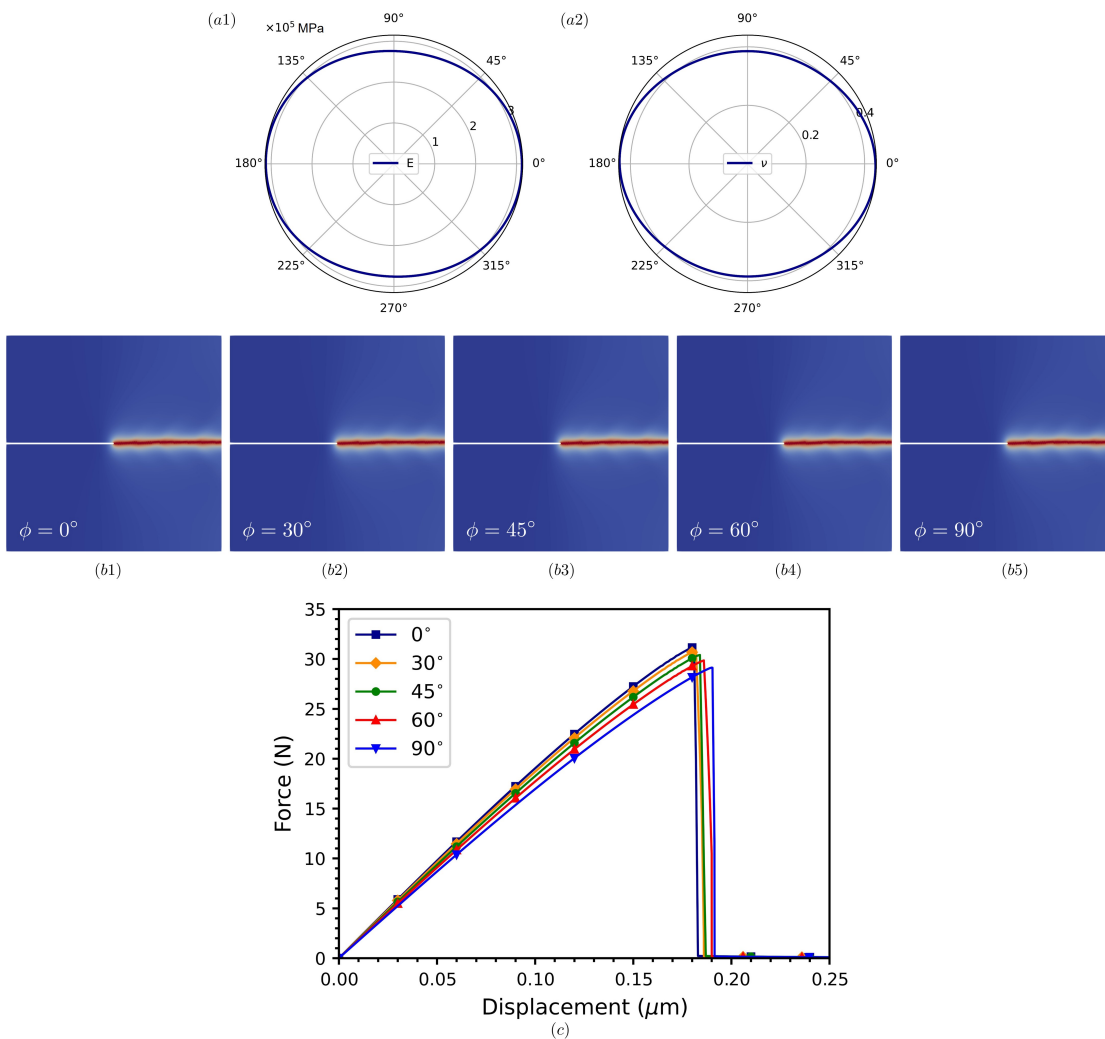


Figure 6.6: Mode I fracture with anisotropic elasticity. (a1)-(a2) Homogenized Young's modulus and Poisson's ratio. (b1)-(b5) Crack patterns with orientation-dependent elasticity tensor. (c) The corresponding load-displacement curves.

The simulated crack patterns with different preferential directions ($0^\circ, 30^\circ, 45^\circ, 60^\circ, 90^\circ$) are shown in Figs. 6.6(b1)-(b5). The cracks develop horizontally similar to Sec. 6.3.1. The simulations show that the anisotropic elasticity alone does not change the crack trajectory.

With orientation-dependent elasticity, the stress perpendicular to the loading direction remains dominant and drives the damage to accumulate at the notch tip, and then drives cracks to propagate horizontally. However, the anisotropic elasticity has an influence on the crack process, as can be seen from the load-displacement curves in Figs. 6.6(c). From Fig. 6.6(a1), Young's modulus reaches the maximum value in the orientation of $\phi = 0^\circ$, therefore the slope of the curve is steepest. Contrarily, the slope of the curve is small when $\phi = 90^\circ$. Meanwhile, a steeper slope of the load-displacement curve corresponds to a smaller fracture displacement and vice versa, due to the isotropic fracture toughness.

6.3.3 Mode I fracture with anisotropic fracture toughness

This section considers the anisotropic fracture property and keeps elasticity tensor isotropic. Fig. 6.7 shows the crack patterns with different preferential orientations ($\phi = 0^\circ, 30^\circ, 45^\circ, 60^\circ, 90^\circ$) and different degree of anisotropy ($\beta = 5, 10, 20$).

With anisotropic fracture toughness, the cracks deviate from the notch direction and are not necessarily perpendicular to the loading direction. With the increase of the angle of orientation from $\phi = 0^\circ$ to 60° , the crack angle increases accordingly, as can be seen from Figs. 6.7(a1)-(a4). The corresponding load-displacement curves with anisotropy degree $\beta = 5$ are plotted in Fig. 6.7(d). It shows that with a bigger preferential angle, the system needs more energy to initiate cracks and propagate. The influence of the anisotropy degree is shown in Fig. 6.7(e) for comparison of different anisotropy degree β with the same orientation $\phi = 0^\circ$. For the same preferential orientation, the peak load where the crack starts to propagate is enhanced with stronger anisotropy. Moreover, with a stronger anisotropy degree, the crack angles increase and are closer to the preferential orientation of the specimen.

Interestingly enough, the crack direction does not increase monolithically with the preferential direction. When ϕ further increases to 90° , the crack returns back to the horizontal direction, perpendicular to the loading direction, as shown in Fig. 6.7(a5). The same conclusion is observed regardless of the degree of anisotropy, as Figs. 6.7(b1)-(b5) and (c1)-(c5) show. To take a closer look at this behavior, a series of simulations with finer increments of the orientation is performed, and the relation between the preferential direction and the crack direction is plotted in Fig. 6.8. A transition behavior of the crack direction with respect to the preferential orientation is observed. When the preferential orientation angle is small, the cracks follow its orientation while the cracks tend to recover to a horizontal direction when the angle is large enough. A reasonable explanation for such behavior can be the competition between the crack driving force and the fracture toughness.

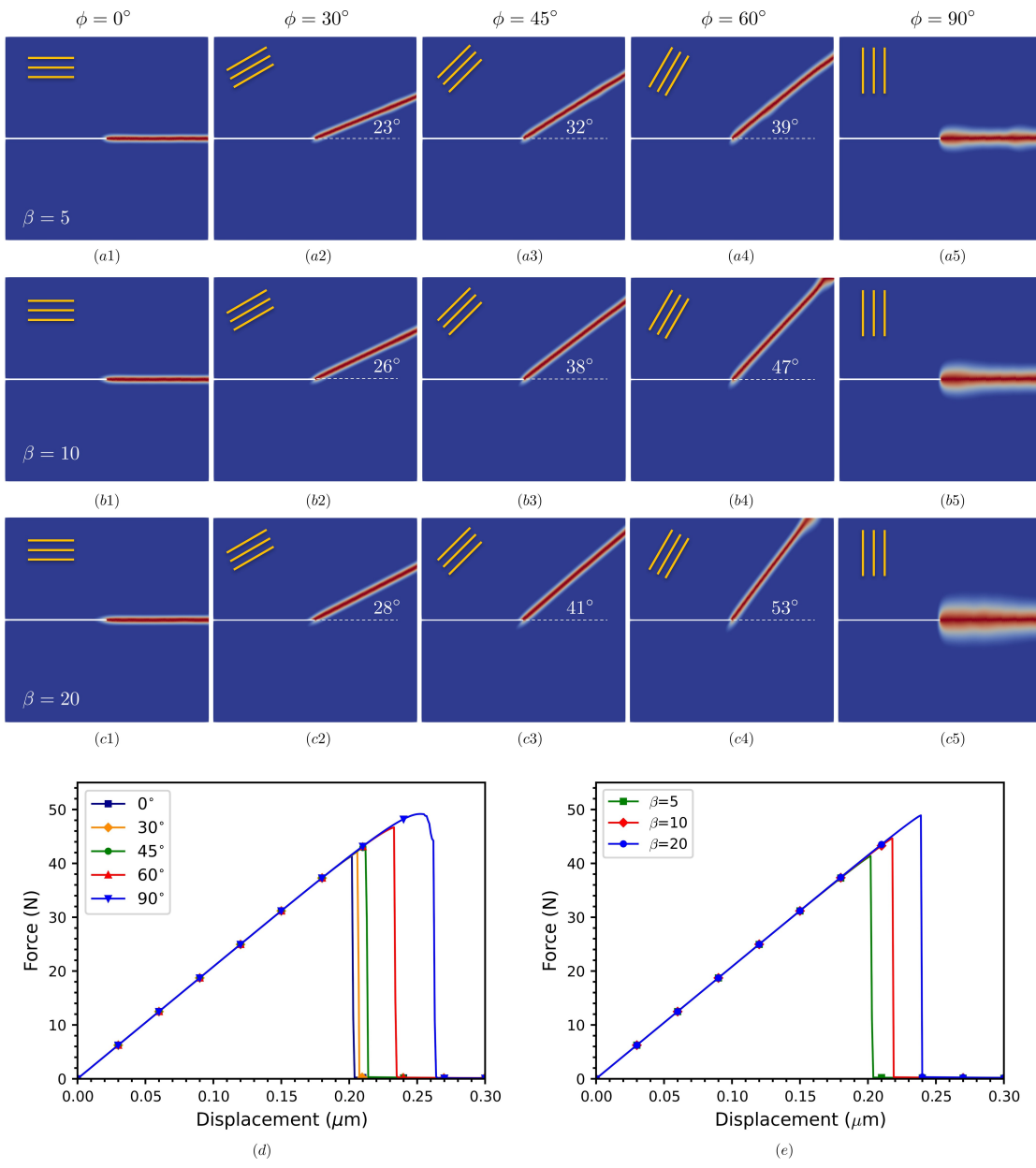


Figure 6.7: Mode I fracture of single-edge notched tension test with anisotropic fracture toughness. Crack patterns of specimens with different preferential directions ($\phi = 0^\circ, 30^\circ, 45^\circ, 60^\circ, 90^\circ$) and degree of anisotropy (a1)-(a5) for $\beta = 5$, (b1)-(b5) for $\beta = 10$, c1-c5 for $\beta = 20$. (d) Load-displacement curves with different preferential orientation with $\beta = 5$, and (e) different β with same orientation $\phi = 0^\circ$.

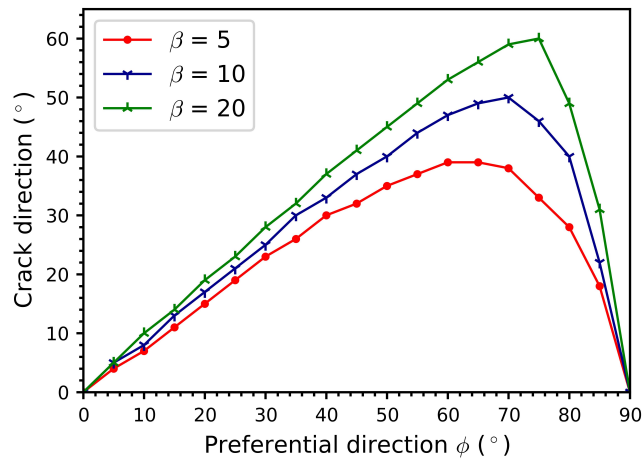


Figure 6.8: Relation of preferential direction and crack direction for single-notched tension test with anisotropic fracture toughness.

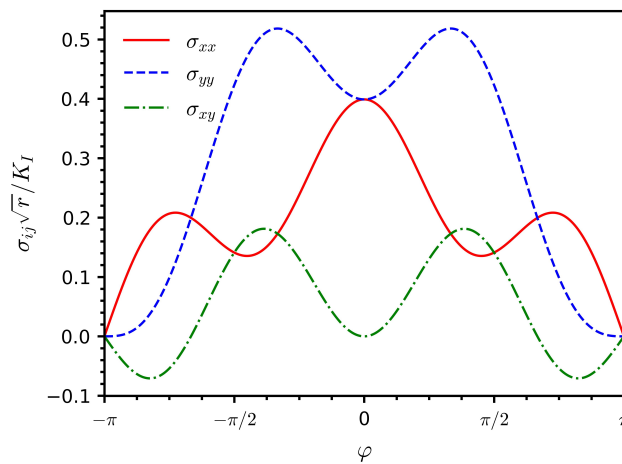


Figure 6.9: Stress fields at the crack tip.

According to the linear fracture mechanics [50], the stress field at the crack tip for mode I crack, with the origin of the coordinate system (r, φ) located at the crack tip, can

be written as

$$\begin{Bmatrix} \sigma_{xx} \\ \sigma_{yy} \\ \sigma_{xy} \end{Bmatrix} = \frac{K_I}{\sqrt{2\pi r}} \cos(\varphi/2) \begin{Bmatrix} 1 - \sin(\varphi/2) \sin(3\varphi/2) \\ 1 + \sin(\varphi/2) \sin(3\varphi/2) \\ \sin(\varphi/2) \cos(3\varphi/2) \end{Bmatrix}, \quad (6.26)$$

where K_I is the stress intensity factor for mode I crack. The stress field is plotted in Fig. 6.9.

When $\phi = 0$, the energetically preferential orientation is aligned with the pre-notch direction. By applying tensile loading on the specimen, the stress field and the corresponding crack driving force (strain energy) are along the pre-notch orientation. Therefore, the crack propagates horizontally. When ϕ increases, the energetically preferential orientation no longer aligns with pre-notch. Crack propagation along the pre-notch direction requires more energy than that of the preferential angle. As a result, the cracks follow the energetically preferential direction and deviate upwards. When ϕ increases further, even though the energy required for the cracking along the preferential angle is relatively lower, the stress field and the crack driving force are not sufficient to support crack propagation in that direction. Therefore, the cracks develop following the maximum strain energy field. Take the extreme case $\phi = 90^\circ$ for example, the energetically preferential angle is perpendicular to the pre-notch direction, and the crack tends to propagate along it as it is energetically weakest. However, the crack develops horizontally due to the given boundary conditions. Note that the damage zone of $\phi = 90^\circ$ is more diffuse than that of $\phi = 0^\circ$. Compared to Figs. 6.7(a5), (b5) and (c5), it is observed that with a stronger anisotropy degree, the damage zone is more diffuse, which could be a result of a stronger competition between crack driving force and the fracture toughness.

6.3.4 Mode I fracture with anisotropic elasticity and fracture toughness

Based on the discussion of the previous two sections, this section considers both anisotropic elasticity and fracture properties. The homogenized elastic moduli are input to the anisotropic phase-field fracture model. The crack patterns with different preferential orientations ($\phi = 0^\circ, 30^\circ, 45^\circ, 60^\circ, 90^\circ$) and different degree of anisotropy ($\beta = 5, 10, 20$) are depicted in Fig. 6.10. With anisotropic elastic and fracture properties, the cracks deviate from the pre-notch direction. Similar to Section. 6.3.3, with the increase of the preferential orientation, the crack angle increases in a certain range. A transition behavior is observed as well. When ϕ is bigger enough, the crack angle decreases and the crack goes back to the horizontal direction.

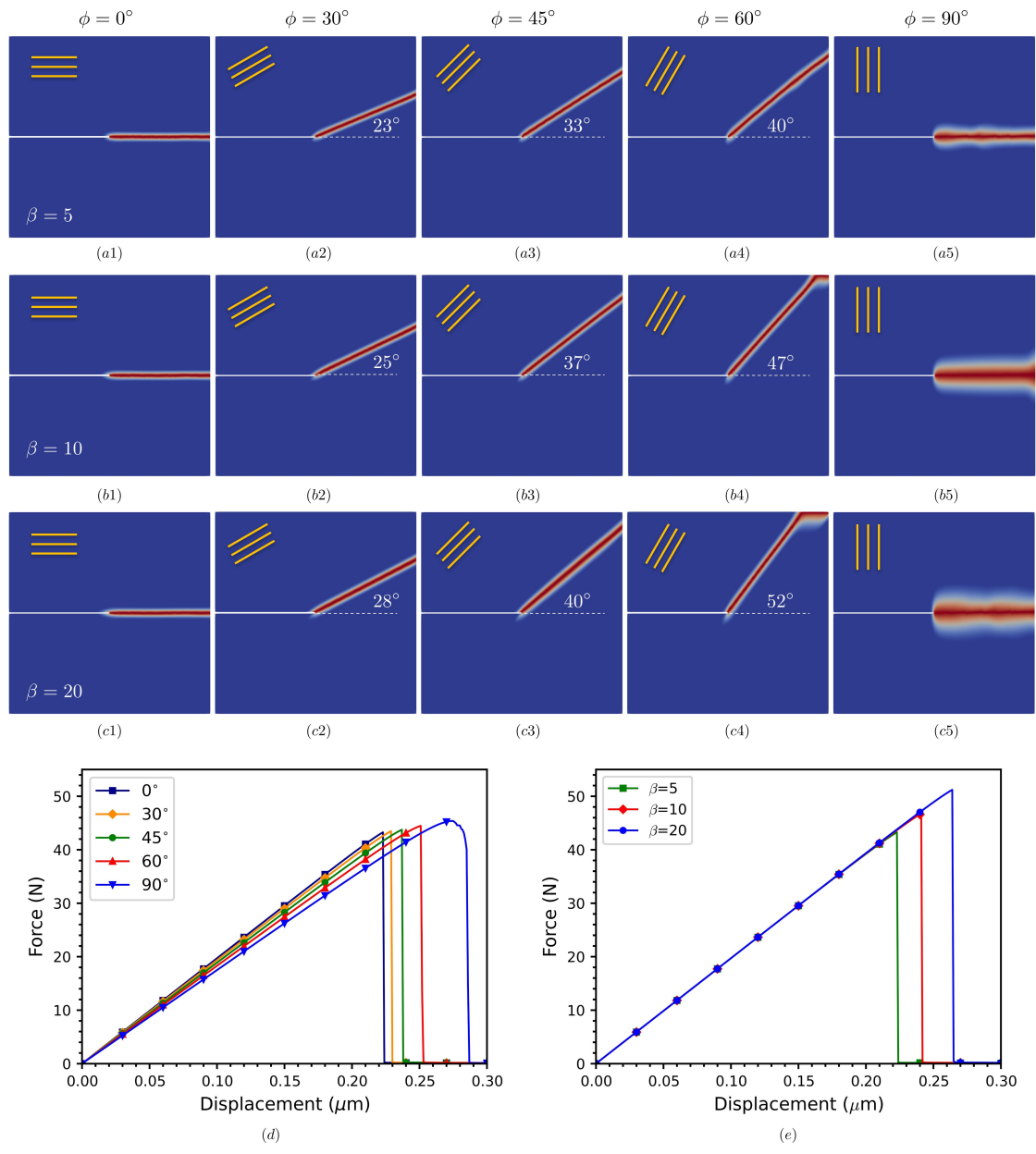


Figure 6.10: Mode I fracture of single-edge notched tension test with anisotropic elasticity and fracture toughness. Crack patterns of specimens with different preferential directions ($\phi = 0^\circ, 30^\circ, 45^\circ, 60^\circ, 90^\circ$) and degree of anisotropy (a1)-(a5) for $\beta = 5$, (b1)-(b5) for $\beta = 10$, (c1)-(c5) for $\beta = 20$. (d) Load-displacement curves with different preferential orientation with $\beta = 5$, and (e) different β with same orientation $\phi = 0^\circ$.

Moreover, the load-displacement curves are also plotted in Fig. 6.10(d). Different from Section 6.3.2 and Section 6.3.3, therein not only the slope but also the area below the curves are different, which is the result of anisotropic elastic modulus and anisotropic fracture toughness, respectively. The influence of the anisotropic degree is also shown. It shows that a stronger anisotropy degree results in a bigger crack angle when ϕ is not large enough, compared to Figs. 6.10(a1)-(a4), (b1)-(b4) and (c1)-(c4) with the same ϕ . Moreover, a larger degree of anisotropy leads to a higher peak load, as plotted in Fig. 6.10(e) for different β with the same orientation $\phi = 0^\circ$.

6.4 Anisotropic fracture simulations of additively manufactured parts

In this section, the proposed anisotropic phase-field fracture model is applied to study the anisotropic fracture behavior of additively manufactured parts. Herein, both the anisotropic elasticity and fracture properties are incorporated simultaneously.

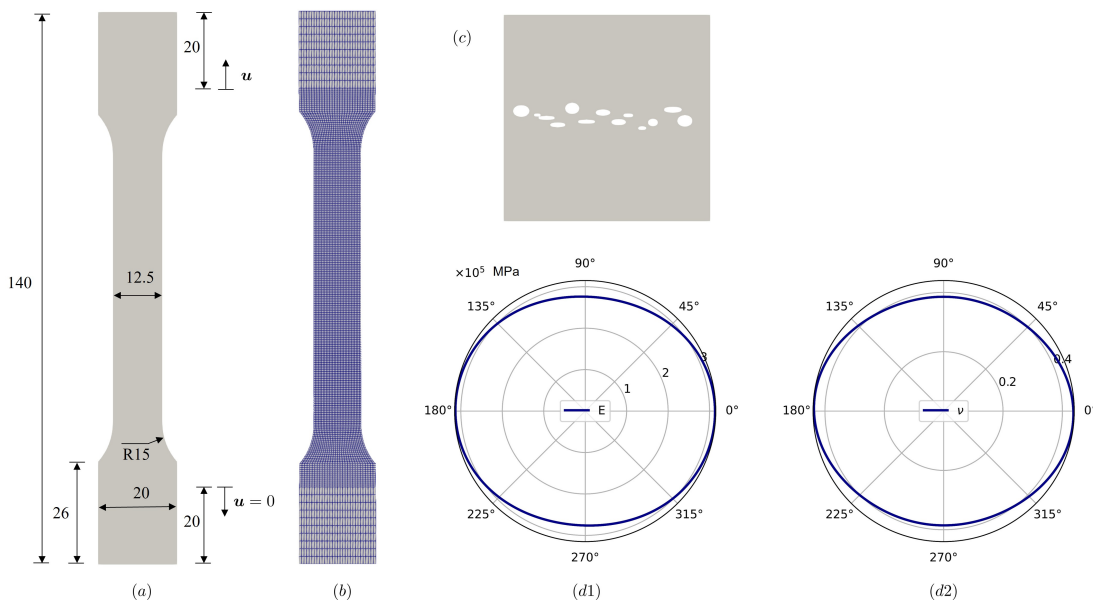


Figure 6.11: Tensile test of I-shape specimen with porous structures. (a) Geometry and (b) mesh of I-shape specimen, (c) a porous RVE of AM parts, and (d1)-(d2) Homogenized Young's modulus and Poisson's ratio.

6.4.1 Homogenization of elastic properties

The I-shape specimens are used to study the effect of building direction and porous layers. Figs. 6.11(a) and (b) show the geometry, boundary conditions and mesh of the specimen, respectively. Given the inherent porosity of additively manufactured parts and different microstructures resulting from different process parameters, a porous RVE containing certain densities of porosities and microcracks between layers is adopted, as shown in Figs. 6.11(c). The material properties used in this section are shown in Table 6.1.

Following the computational homogenization scheme in Section. 6.2.2, the effective elastic moduli of the RVE, i.e., Young's modulus and Poisson's ratio are shown in Figs. 6.11(d1) and (d2), respectively. Due to the porous layer structure, the effective properties are orientation-dependent. Due to the chosen RVE which contains a low density of pores and microcracks, the anisotropy degree of elastic properties is not quite pronounced.

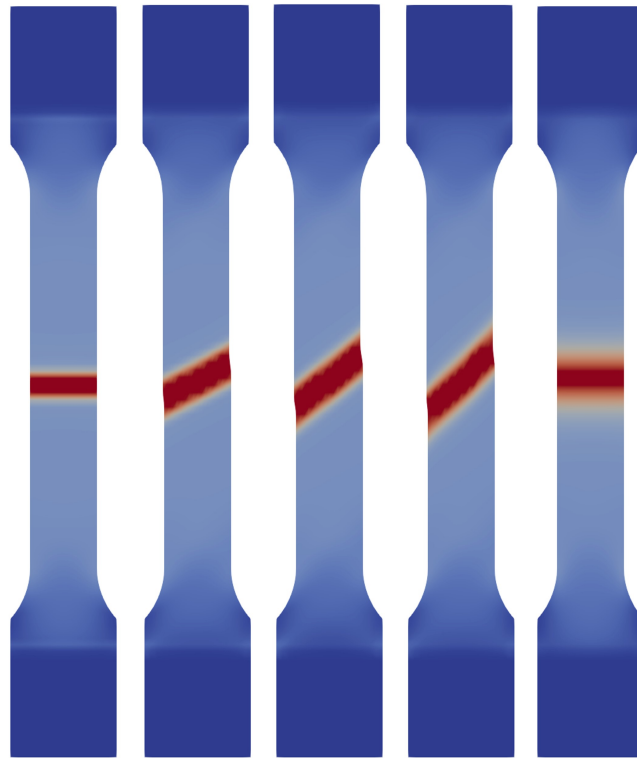
Table 6.1: Material parameters for I-shape specimen tensile test

E (GPa)	ν	G_c (J/m ²)	σ_u (MPa)
340	0.22	42.47	180

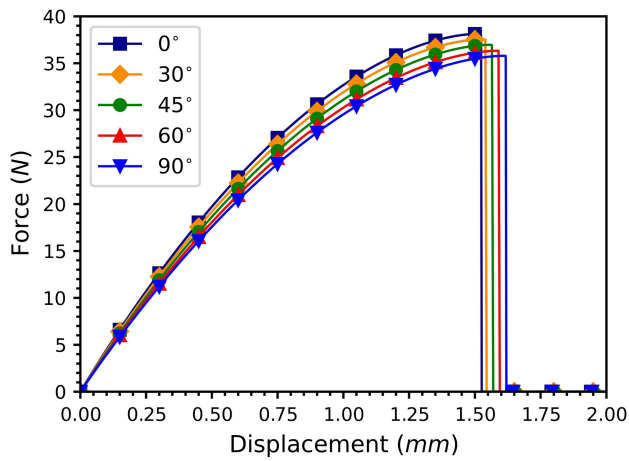
6.4.2 Anisotropic fracture of additively manufactured parts

With the anisotropic elasticity and anisotropic fracture property, the simulations of the tensile test of the additively manufactured I-shape specimen with different layer orientations are performed. The results for specimen with preferential orientations ($0^\circ, 30^\circ, 45^\circ, 60^\circ, 90^\circ$) using RVE are shown in Figs. 6.12(a1)-(a5), respectively.

It shows that the fracture behavior of the additively manufactured part would preferably follow the layers' orientation in a certain range when the orientation is not so large. Otherwise, the crack would propagate perpendicular to the loading direction. As can be seen from the load-displacement curves for both cases in Figs. 6.12(b). In view of Figs. 6.11(c), the slope of the load-displacement curves depends on the effective Young's modulus. For this RVE, Young's modulus is smallest when $\phi = 90^\circ$, and reaches its peak when $\phi = 0^\circ$. Correspondingly, the slope of $\phi = 90^\circ$ is the smallest and $\phi = 0^\circ$ the most steep. The obtained crack patterns for all orientations are in good agreement with the experimental measurements reported in Fig. 6.2.



(a1) (a2) (a3) (a4) (a5)



(b)

Figure 6.12: Simulation results of anisotropic fracture of additively manufactured parts. (a1)-(a5) the crack patterns with layer orientation 0° , 30° , 45° , 60° , 90° , respectively. (b) the corresponding load-displacement curves.

6.5 Conclusions and outlook

In this chapter, a phase-field model for anisotropic fracture based on computational homogenization is developed to study the anisotropic fracture behavior of additively manufactured parts. Herein, not only the anisotropic elasticity but also the anisotropic fracture properties are considered. Due to the various defects like pores, microcracks, etc., resulting from the AM process, the AM-built parts tend to be porous, especially between different layers. The varied building directions and/or scanning directions contribute to the direction-dependent porous layers microstructure of the AM parts. Therefore, their mechanical properties are not isotropic and instead orientation-dependent. To characterize the anisotropy, the orientation-dependent elastic moduli are computed using the computational homogenization scheme. As a result of the elastic anisotropy, a stress-based split method, i.e., the stress spectral decomposition approach is adopted. To account for the direction-dependent fracture toughness of AM parts, a second-order structural tensor which is dependent on the preferential direction is introduced to the crack energy density and the phase-field fracture model. A series of benchmark examples are performed to show the influence of the anisotropic elasticity and/or anisotropic fracture properties on the fracture process, qualitatively and quantitatively. The results show the anisotropic elasticity alone does not change the crack path but affects the load-displacement curve. On the other hand, the anisotropic fracture toughness has a significant effect on the crack patterns. The crack angle follows the trend of preferential direction and a transition zone exists. Beyond that region, the crack develops back horizontally. Furthermore, considering anisotropic elasticity and anisotropic fracture properties simultaneously results in different crack patterns and load-displacement responses at the same time. The presented model is then applied to investigate the anisotropic fracture of AM parts. Bigger porosity would cause stronger anisotropy, and the crack path differs with different preferential directions. The simulation results of AM parts with different orientations agree well with the experimental observations.

Future studies can be performed when it comes to the extension of the current anisotropic brittle fracture model to anisotropic ductile fracture, where plasticity and yielding behaviors play an important role so that the model can be used to predict a broader spectrum of material systems. The RVE chosen in the work is based on rough experimental observation. However, a more accurate description of RVE from AM parts is needed to better compute the effective elastic properties. More detailed comparisons with the experimental results are worthy of investigation as well, so that a more solid numerical model can be calibrated and validated.

7 Conclusions and Outlook

7.1 Conclusions

In this thesis, the phase-field modeling of thermo-mechanical coupled fracture and anisotropic fracture are presented to study the thermal cracking in the additive manufacturing process and the anisotropic fracture phenomenon of additively manufactured parts, respectively. The contributions of this work are summarized as follows.

- A thermodynamically-consistent framework for thermo-elastic coupled brittle fracture using the cohesive phase-field model is developed. Derived from the basic principles of thermodynamics, the coupling effects among mechanics, heat transfer, and fracture are all taken into account. Particularly, the influence of temperature-dependent fracture properties and the degradation of thermal conductivity with the crack field are studied to capture the temperature field and the crack pattern more accurately. The degraded thermal conductivity can avoid nonphysical heat transfer in the fully-cracked regions. The insensitivity of the CPF model, which is adopted in the multiphysics framework, with respect to the incorporated length scale parameter is also studied.
- A multiphysics phase-field model for thermo-ductile coupled fracture in thermo-elasto-plastic solid in the context of large deformation is developed. The theoretical framework comprises three parts: degraded elastoplasticity by damage, phase-field model of ductile fracture based on microforce balance, as well as damaged heat transfer. The intercoupling mechanisms among elastoplasticity, phase-field crack and heat transfer are considered comprehensively. Among them, threefold plasticity-damage coupling mechanisms are considered here. The proposed fracture model is benchmarked with simulation results of a tensile test of an I-shape specimen encompassing elastoplasticity, hardening, necking, crack initiation and propagation, and validated with the experimental observations and results regarding the whole ductile process. Multiple characteristic parameters of the proposed model are investigated for their influence on the fracture process.

-
- A validated numerical workflow to study thermal cracking in the additive manufacturing process, particularly powder bed fusion is developed. To accurately capture the cracking behaviors, not only the thermal strain but also the solidification shrinkage strain are considered simultaneously. To input the thermal evolution history, three different methods are utilized. Firstly, an analytic temperature solution is used to obtain the temperature field near the melting pool. Therein, different AM process is modeled via the simple modification of the thermal gradient. Subsequently, the phenomenological PBF model is utilized to obtain a more accurate temperature field, specifically for a slice of the whole powder bed model. The process parameters like the laser power and the scanning speed on the final crack pattern are investigated. Lastly, a higher-fidelity model of the PBF process, the non-isothermal phase-field model is adopted to better characterize the chronological-spatial distribution of the complex morphology of the PBF process.
 - A phase-field model for anisotropic fracture based on computational homogenization is developed to study the anisotropic fracture behavior of additively manufactured parts. Herein, not only the anisotropic elasticity but also the anisotropic fracture properties are considered. To characterize the anisotropy, the orientation-dependent elastic moduli are computed using the computational homogenization scheme. As a result of the elastic anisotropy, a stress-based split method, i.e., the stress spectral decomposition approach is adopted. To account for the direction-dependent fracture toughness of AM parts, a second-order structural tensor which is dependent on the preferential direction is introduced to the crack energy density and the phase-field fracture model.

Studies of the thesis are dedicated to understanding the fracture mechanism of complex material systems, especially in a multiphysics environment, the thermal cracking mechanisms of AM process, and the fracture behaviors of AM-built parts. The following conclusions can be drawn from these numerical investigations.

- The cohesive phase-field fracture model holds the length-scale insensitivity in thermo-mechanical settings. In other words, the material's response is independent of the length scale parameter used in the model. Meanwhile, the damage zone of the CPF model is more compact than that of the AT2 model.
- The heat-damage coupling is important to accurately capture the heat flux distribution and the temperature jump at cracked regions in thermo-mechanical problems.
- With a higher initial temperature, the number of thermal-induced cracks and the crack density are increased in the quenching test.

-
- The damage-plasticity coupling plays an important role in the fracture process of ductile materials.
 - The solidification shrinkage strain is indispensable to accurately predict the thermal cracking phenomenon in the additive manufacturing process.
 - The cracking patterns depend on the process parameters. Higher laser power and slower scanning speed result in higher liner energy density, and a combination of keyhole mode cracking. On the other hand, lower laser power and faster scanning speed lead to lower liner energy density and conduction mode cracking pattern.
 - The anisotropic elasticity and anisotropic fracture toughness should be considered simultaneously to model the anisotropic fracture behaviors of AM parts.

7.2 Outlook

Based on the studies of this work, further investigations can be performed when it comes to the following two main aspects. First, as for the phase-field fracture models,

- Assumption that the quasi-static fracture process in both the phase-field brittle fracture model and ductile fracture model is made. Thus, extension to the transient dynamical fracture process is of great interest.
- The additional heat source terms in the heat equation induced by the coupling mechanisms between heat and other physics are ignored. Accounting for all the coupling terms in the heat equation contributes to a more precise prediction of the temperature field and heat flux distribution.
- More physical phenomena of the ductile fracture process can also be incorporated to the ductile fracture model, like void growth and coalescence. Different hardening functions should also be customized for different materials for more accurate prediction. Further, systematic experimental tests under varying temperatures can be performed to benchmark and validate the capability of the present model.
- Alternative methods to introduce the anisotropy into the phase-field model for anisotropic fracture are worthy of investigation, e.g., the arbitrary anisotropy. Meanwhile, the precise construction of the RVE of the AM parts resorts to the experiment characterization.

Moreover, as for the numerical modeling of the AM process,

-
- Different ways to obtain the temperature profile of the AM process have been utilized in this work. However, given that the metal AM like LPBF is a highly localized complex process involving multiphysics across length and time scales, it is challenging to develop a sound model to capture all the physics. In this work, the interpolated elliptic solution, a phenomenological model, and a non-isothermal phase-field model are employed, but only the thermal diffusion and grain growth are considered, and all other complex physics occurring in AM are not in the scope for now. For example, after materials melt, thermal fluid dynamics comes into play in the melting pool, which captures the solid-liquid transition and is crucial in the terminal stage of solidification shrinkage and hot cracking. With very high energy input into the small-scale melting pool, the materials can even evaporate. The evaporation leads to the formation of voids or keyholes where stress concentration inhabits and crackings are prone to develop. Moreover, it is also worth exploring the combination of the dendrite growth model with the fracture model to study the influence on hot cracking.
 - Single-layer and single-pass AM process is considered for simplicity. However, multi-layer multipass manufacturing is needed for real production, where the cracking healing phenomenon occurs. The laser scanning of the next layer causes the previously solidified materials to re-melt, and possible cracking of the existing cracking to heal. A more accurate yet complex model is required for such a complicated process.
 - The AM process studied in this work is confined to the LPBF. However, other AM techniques, like direct energy decomposition which shares similarities with LPBF but has its own features like materials decomposition are also widely employed. Therefore, the extension of the current thermal cracking study of LPBF to DED would also be of great interest.

Bibliography

- [1] Quanquan Han et al. “Effect of Hot Cracking on the Mechanical Properties of Hastelloy X Superalloy Fabricated by Laser Powder Bed Fusion Additive Manufacturing”. In: *Optics & Laser Technology* 124 (Apr. 2020), p. 105984.
- [2] Cassiopée Galy et al. “Main Defects Observed in Aluminum Alloy Parts Produced by SLM: From Causes to Consequences”. In: *Additive Manufacturing* 22 (Aug. 2018), pp. 165–175.
- [3] DG Eskin, L Katgerman, et al. “Mechanical properties in the semi-solid state and hot tearing of aluminium alloys”. In: *Progress in materials science* 49.5 (2004), pp. 629–711.
- [4] Michel Rappaz and Jonathan A Dantzig. *Solidification*. EPFL Press, 2009.
- [5] John H Martin et al. “3D printing of high-strength aluminium alloys”. In: *Nature* 549.7672 (2017), pp. 365–369.
- [6] Jiangwei Liu and Sindo Kou. “Susceptibility of ternary aluminum alloys to cracking during solidification”. In: *Acta Materialia* 125 (2017), pp. 513–523.
- [7] Xiaoqiang Zhang et al. “Cracking mechanism and susceptibility of laser melting deposited Inconel 738 superalloy”. In: *Materials & Design* 183 (2019), p. 108105.
- [8] Yao Li, Kai Chen, and Nobumichi Tamura. “Mechanism of heat affected zone cracking in Ni-based superalloy DZ125L fabricated by laser 3D printing technique”. In: *Materials & Design* 150 (2018), pp. 171–181.
- [9] Mohammad Saadati, Amir Keyvan Edalat Nobarzad, and Mohammad Jahazi. “On the hot cracking of HSLA steel welds: Role of epitaxial growth and HAZ grain size”. In: *Journal of Manufacturing Processes* 41 (2019), pp. 242–251.
- [10] Alixe Dreano et al. “Computational Design of a Crack-Free Aluminum Alloy for Additive Manufacturing”. In: *Additive Manufacturing* 55 (July 2022), p. 102876.
- [11] Wojciech Stopyra et al. “Laser Powder Bed Fusion of AA7075 Alloy: Influence of Process Parameters on Porosity and Hot Cracking”. In: *Additive Manufacturing* 35 (Oct. 2020), p. 101270.

-
-
- [12] Syed Z Uddin et al. "Processing and characterization of crack-free aluminum 6061 using high-temperature heating in laser powder bed fusion additive manufacturing". In: *Additive Manufacturing* 22 (2018), pp. 405–415.
- [13] Andreas Wimmer et al. "Experimental and numerical investigations of the hot cracking susceptibility during the powder bed fusion of AA 7075 using a laser beam". In: *Progress in Additive Manufacturing* (2023), pp. 1–15.
- [14] Jiangwei Liu and Sindo Kou. "Crack Susceptibility of Binary Aluminum Alloys during Solidification". In: *Acta Materialia* 110 (May 2016), pp. 84–94.
- [15] Alixe Dreano et al. "Computational Design of a Crack-Free Aluminum Alloy for Additive Manufacturing". In: *Additive Manufacturing* 55 (July 2022), p. 102876.
- [16] L. Aucott et al. "A Three-Stage Mechanistic Model for Solidification Cracking During Welding of Steel". In: *Metallurgical and Materials Transactions A* 49.5 (May 2018), pp. 1674–1682.
- [17] Chuan Guo et al. "Additive manufacturing of Ni-based superalloys: Residual stress, mechanisms of crack formation and strategies for crack inhibition". In: *Nano Materials Science* 5.1 (2023), pp. 53–77.
- [18] Qingsong Wei et al. "Crack types, mechanisms, and suppression methods during high-energy beam additive manufacturing of nickel-based superalloys: A review". In: *Chinese Journal of Mechanical Engineering: Additive Manufacturing Frontiers* (2022), p. 100055.
- [19] Edouard Chauvet et al. "Hot cracking mechanism affecting a non-weldable Ni-based superalloy produced by selective electron Beam Melting". In: *Acta Materialia* 142 (2018), pp. 82–94.
- [20] Shubham Chandra et al. "A Generalised Hot Cracking Criterion for Nickel-Based Superalloys Additively Manufactured by Electron Beam Melting". In: *Additive Manufacturing* 37 (Jan. 2021), p. 101633.
- [21] Ning Li et al. "Crack initiation mechanism of laser powder bed fusion additive manufactured Al-Zn-Mg-Cu alloy". In: *Materials Characterization* 195 (2023), p. 112415.
- [22] Shibo Wu et al. "Hot Cracking Evolution and Formation Mechanism in 2195 Al-Li Alloy Printed by Laser Powder Bed Fusion". In: *Additive Manufacturing* 54 (June 2022), p. 102762.
- [23] Janusz Adamiec. "Assessment of the Hot-Cracking Susceptibility of Welded Joints of the 7CrMoVTiB10-10 Bainitic Steel Used in Heat Exchangers". In: *Energies* 16.1 (2022), p. 162.

-
-
- [24] Alberta Aversa et al. “A study of the microstructure and the mechanical properties of an AlSiNi alloy produced via selective laser melting”. In: *Journal of Alloys and Compounds* 695 (2017), pp. 1470–1478.
- [25] Mathieu Opprecht et al. “A solution to the hot cracking problem for aluminium alloys manufactured by laser beam melting”. In: *Acta Materialia* 197 (2020), pp. 40–53.
- [26] David T Rees et al. “In situ X-ray imaging of hot cracking and porosity during LPBF of Al-2139 with TiB₂ additions and varied process parameters”. In: *Materials & Design* (2023), p. 112031.
- [27] Meirong Gu et al. “Scalable Manufacturing of the Al-based Master Composites Containing TiB₂ and TiC Particles and Their Modification Effect on the Hot Cracking of Rapidly Solidified Al Alloys”. In: *Materials Today Communications* 37 (Dec. 2023), p. 107142.
- [28] Peng Wang et al. “Effect of Zr on Microstructure and Hot Cracking Susceptibility of ZGH451 Superalloy Fabricated by Direct Energy Deposition”. In: *Journal of Alloys and Compounds* 965 (Nov. 2023), p. 171371.
- [29] Yanan Zhao et al. “New Alloy Design Approach to Inhibiting Hot Cracking in Laser Additive Manufactured Nickel-Based Superalloys”. In: *Acta Materialia* 247 (Apr. 2023), p. 118736.
- [30] KenHee Ryou et al. “Microstructural Evolution and Hot Cracking Prevention in Direct-Laser-Deposited Ni-based Superalloy through Hf Addition”. In: *Materials & Design* 234 (Oct. 2023), p. 112298.
- [31] Xintian Wang et al. “Solving the Problem of Solidification Cracking during Additive Manufacturing of CrMnFeCoNi High-Entropy Alloys through Addition of Cr₃C₂ Particles to Enhance Microstructure and Properties”. In: *Materials Today Advances* 18 (June 2023), p. 100371.
- [32] Fabian Soffel et al. “Laser Preheating for Hot Crack Reduction in Direct Metal Deposition of Inconel 738LC”. In: *Metals* 12.4 (2022), p. 614.
- [33] Hongyang Cui et al. “Microstructure Control and Hot Cracking Behavior of the New Ni-Co Based Superalloy Prepared by Electron Beam Smelting Layered Solidification Technology”. In: *Journal of Materials Science & Technology* 175 (Mar. 2024), pp. 55–71.
- [34] Mingyu Liu et al. “Laser Powder Bed Fusion of a Ni₃Al-based Intermetallic Alloy with Tailored Microstructure and Superior Mechanical Performance”. In: *Advanced Powder Materials* 3.1 (Feb. 2024), p. 100152.

-
-
- [35] DG Eskin and L Katgerman. “A quest for a new hot tearing criterion”. In: *Metallurgical and Materials Transactions A* 38 (2007), pp. 1511–1519.
- [36] Yue Li et al. “Recent advances in hot tearing during casting of aluminium alloys”. In: *Progress in Materials Science* 117 (2021), p. 100741.
- [37] DJ Lahaie and M Bouchard. “Physical modeling of the deformation mechanisms of semisolid bodies and a mechanical criterion for hot tearing”. In: *Metallurgical and materials Transactions B* 32 (2001), pp. 697–705.
- [38] Mohammed M’Hamdi, Asbjørn Mo, and Hallvard G Fjær. “TearSim: A two-phase model addressing hot tearing formation during aluminum direct chill casting”. In: *Metallurgical and Materials Transactions A* 37 (2006), pp. 3069–3083.
- [39] M Rappaz, J-M Drezet, and Met Gremaud. “A new hot-tearing criterion”. In: *Metallurgical and materials transactions A* 30.2 (1999), pp. 449–455.
- [40] M Braccini et al. “Relation between mushy zone rheology and hot tearing phenomena in Al-Cu alloys”. In: *Modeling of casting, welding, and advanced solidification processes IX* (2000), pp. 18–24.
- [41] Joar Draxler. “Modeling and Simulation of Weld Hot Cracking”. PhD thesis. Luleå tekniska universitet, 2019.
- [42] Fan Zhang et al. “Prediction of cracking susceptibility of commercial aluminum alloys during solidification”. In: *Metals* 11.9 (2021), p. 1479.
- [43] Suyitno, WH Kool, and L Katgerman. “Integrated approach for prediction of hot tearing”. In: *Metallurgical and Materials Transactions A* 40 (2009), pp. 2388–2400.
- [44] Sindo Kou. “A criterion for cracking during solidification”. In: *Acta Materialia* 88 (2015), pp. 366–374.
- [45] Wenbin Liu, Gan Li, and Jian Lu. “Modeling solidification cracking: A new perspective on solid bridge fracture”. In: *Journal of the Mechanics and Physics of Solids* 188 (2024), p. 105651.
- [46] Meisam Sistaninia et al. “Simulation of semi-solid material mechanical behavior using a combined discrete/finite element method”. In: *Metallurgical and Materials Transactions A* 42 (2011), pp. 239–248.
- [47] M Sistaninia et al. “A 3-D coupled hydromechanical granular model for simulating the constitutive behavior of metallic alloys during solidification”. In: *Acta Materialia* 60.19 (2012), pp. 6793–6803.

-
-
- [48] AB Phillion, SL Cockcroft, and PD Lee. “A three-phase simulation of the effect of microstructural features on semi-solid tensile deformation”. In: *Acta Materialia* 56.16 (2008), pp. 4328–4338.
- [49] M Sistaninia et al. “Three-dimensional granular model of semi-solid metallic alloys undergoing solidification: Fluid flow and localization of feeding”. In: *Acta Materialia* 60.9 (2012), pp. 3902–3911.
- [50] Dietmar Gross and Thomas Seelig. *Fracture mechanics: with an introduction to micromechanics*. Springer, 2017.
- [51] Ted L Anderson and Ted L Anderson. *Fracture mechanics: fundamentals and applications*. CRC press, 2005.
- [52] Chin-Teh Sun and Zhihe Jin. *Fracture mechanics*. Academic press, 2011.
- [53] Alan Arnold Griffith. “VI. The phenomena of rupture and flow in solids”. In: *Philosophical transactions of the royal society of london. Series A, containing papers of a mathematical or physical character* 221.582-593 (1921), pp. 163–198.
- [54] George Rankin Irwin. “Onset of fast crack propagation in high strength steel and aluminum alloys”. In: (1956).
- [55] George R Irwin. “Analysis of stresses and strains near the end of a crack traversing a plate”. In: (1957).
- [56] James R. Rice. “A Path Independent Integral and the Approximate Analysis of Strain Concentration by Notches and Cracks”. In: (1968).
- [57] Gilles A Francfort and J-J Marigo. “Revisiting brittle fracture as an energy minimization problem”. In: *Journal of the Mechanics and Physics of Solids* 46.8 (1998), pp. 1319–1342.
- [58] Andrea Braides et al. *Approximation of free-discontinuity problems*. 1694. Springer Science & Business Media, 1998.
- [59] Blaise Bourdin, Gilles A Francfort, and Jean-Jacques Marigo. “Numerical experiments in revisited brittle fracture”. In: *Journal of the Mechanics and Physics of Solids* 48.4 (2000), pp. 797–826.
- [60] Blaise Bourdin. “Numerical implementation of the variational formulation for quasi-static brittle fracture”. In: *Interfaces and free boundaries* 9.3 (2007), pp. 411–430.
- [61] Blaise Bourdin, Gilles A Francfort, and Jean-Jacques Marigo. “The variational approach to fracture”. In: *Journal of elasticity* 91.1 (2008), pp. 5–148.

-
-
- [62] Hanen Amor, Jean-Jacques Marigo, and Corrado Maurini. “Regularized formulation of the variational brittle fracture with unilateral contact: Numerical experiments”. In: *Journal of the Mechanics and Physics of Solids* 57.8 (2009), pp. 1209–1229.
- [63] Christian Miehe, Fabian Welschinger, and Martina Hofacker. “Thermodynamically consistent phase-field models of fracture: Variational principles and multi-field FE implementations”. In: *International journal for numerical methods in engineering* 83.10 (2010), pp. 1273–1311.
- [64] Christian Miehe, Martina Hofacker, and Fabian Welschinger. “A phase field model for rate-independent crack propagation: Robust algorithmic implementation based on operator splits”. In: *Computer Methods in Applied Mechanics and Engineering* 199.45-48 (2010), pp. 2765–2778.
- [65] Michael J Borden et al. “A phase-field description of dynamic brittle fracture”. In: *Computer Methods in Applied Mechanics and Engineering* 217 (2012), pp. 77–95.
- [66] Rudy JM Geelen et al. “A phase-field formulation for dynamic cohesive fracture”. In: *Computer Methods in Applied Mechanics and Engineering* 348 (2019), pp. 680–711.
- [67] Christian Miehe and Steffen Mauthe. “Phase field modeling of fracture in multi-physics problems. Part III. Crack driving forces in hydro-poro-elasticity and hydraulic fracturing of fluid-saturated porous media”. In: *Computer Methods in Applied Mechanics and Engineering* 304 (2016), pp. 619–655.
- [68] Jacinto Ulloa et al. “Variational modeling of hydromechanical fracture in saturated porous media: A micromechanics-based phase-field approach”. In: *Computer Methods in Applied Mechanics and Engineering* 396 (2022), p. 115084.
- [69] Bo Yin and Michael Kaliske. “Fracture simulation of viscoelastic polymers by the phase-field method”. In: *Computational Mechanics* 65.2 (2020), pp. 293–309.
- [70] Mohammad Reza Khosravani et al. “Fracture behavior of anisotropic 3D-printed parts: Experiments and numerical simulations”. In: *Journal of Materials Research and Technology* (2022).
- [71] Shahed Rezaei et al. “Direction-dependent fracture in solids: Atomistically calibrated phase-field and cohesive zone model”. In: *Journal of the Mechanics and Physics of Solids* 147 (2021), p. 104253.
- [72] Bai-Xiang Xu, Ying Zhao, and Peter Stein. “Phase field modeling of electrochemically induced fracture in Li-ion battery with large deformation and phase segregation”. In: *GAMM-Mitteilungen* 39.1 (2016), pp. 92–109.

-
-
- [73] Bai-Xiang Xu et al. “Phase field simulation of domain structures in cracked ferro-electrics”. In: *International journal of fracture* 165.2 (2010), pp. 163–173.
- [74] A Valverde-González et al. “Computational modelling of hydrogen assisted fracture in polycrystalline materials”. In: *international journal of hydrogen energy* 47.75 (2022), pp. 32235–32251.
- [75] Roberto Alessi et al. “Comparison of phase-field models of fracture coupled with plasticity”. In: *Advances in computational plasticity: A book in honour of D. Roger J. Owen* (2018), pp. 1–21.
- [76] Martina Hofacker and Christian Miehe. “A phase field model for ductile to brittle failure mode transition”. In: *Pamm* 12.1 (2012), pp. 173–174.
- [77] Heike Ulmer, Martina Hofacker, and Christian Miehe. “Phase field modeling of brittle and ductile fracture”. In: *Pamm* 13.1 (2013), pp. 533–536.
- [78] Fernando P. Duda et al. “A Phase-Field/Gradient Damage Model for Brittle Fracture in Elastic–Plastic Solids”. In: *International Journal of Plasticity* 65 (Feb. 2015), pp. 269–296.
- [79] C. Miehe et al. “Phase Field Modeling of Fracture in Multi-Physics Problems. Part II. Coupled Brittle-to-Ductile Failure Criteria and Crack Propagation in Thermo-Elastic–Plastic Solids”. In: *Computer Methods in Applied Mechanics and Engineering* 294 (Sept. 2015), pp. 486–522.
- [80] Charlotte Kuhn, Timo Noll, and Ralf Müller. “On Phase Field Modeling of Ductile Fracture”. In: *GAMM-Mitteilungen* 39.1 (2016).
- [81] Marreddy Ambati, Roland Kruse, and Laura De Lorenzis. “A Phase-Field Model for Ductile Fracture at Finite Strains and Its Experimental Verification”. In: *Computational Mechanics* 57.1 (Jan. 2016), pp. 149–167.
- [82] Christian Miehe, Fadi Aldakheel, and Arun Raina. “Phase Field Modeling of Ductile Fracture at Finite Strains: A Variational Gradient-Extended Plasticity-Damage Theory”. In: *International Journal of Plasticity* 84 (Sept. 2016), pp. 1–32.
- [83] Michael J Borden et al. “A phase-field formulation for fracture in ductile materials: Finite deformation balance law derivation, plastic degradation, and stress triaxiality effects”. In: *Computer Methods in Applied Mechanics and Engineering* 312 (2016), pp. 130–166.

-
-
- [84] Christian Miehe, Fadi Aldakheel, and Stephan Teichtmeister. “Phase-Field Modeling of Ductile Fracture at Finite Strains: A Robust Variational-Based Numerical Implementation of a Gradient-Extended Theory by Micromorphic Regularization”. In: *International Journal for Numerical Methods in Engineering* 111.9 (2017), pp. 816–863.
- [85] N. Khandelwal and A. Ramachandra Murthy. “Ductile Fracture Simulation Using Phase Field Method with Various Damage Models Based on Different Degradation and Geometric Crack Functions”. In: *Materials Today Communications* 35 (June 2023), p. 105627.
- [86] M. Ambati, T. Gerasimov, and L. De Lorenzis. “Phase-Field Modeling of Ductile Fracture”. In: *Computational Mechanics* 55.5 (May 2015), pp. 1017–1040.
- [87] M Dittmann et al. “Variational phase-field formulation of non-linear ductile fracture”. In: *Computer Methods in Applied Mechanics and Engineering* 342 (2018), pp. 71–94.
- [88] Jike Han et al. “Crack Phase-Field Model Equipped with Plastic Driving Force and Degrading Fracture Toughness for Ductile Fracture Simulation”. In: *Computational Mechanics* 69.1 (Jan. 2022), pp. 151–175.
- [89] Bo Yin and Michael Kaliske. “A Ductile Phase-Field Model Based on Degrading the Fracture Toughness: Theory and Implementation at Small Strain”. In: *Computer Methods in Applied Mechanics and Engineering* 366 (July 2020), p. 113068.
- [90] Hao Zhang et al. “Phase-field modeling of coupled spall and adiabatic shear banding and simulation of complex cracks in ductile metals”. In: *Journal of the Mechanics and Physics of Solids* 172 (2023), p. 105186.
- [91] Revanth Matthey et al. “Phase-Field Fracture Coupled Elasto-Plastic Constitutive Model for 3D Printed Thermoplastics and Composites”. In: *Engineering Fracture Mechanics* 291 (Oct. 2023), p. 109535.
- [92] Emilio Martínez-Pañeda, Alireza Golahmar, and Christian F Niordson. “A phase field formulation for hydrogen assisted cracking”. In: *Computer Methods in Applied Mechanics and Engineering* 342 (2018), pp. 742–761.
- [93] Tushar Kanti Mandal, Vinh Phu Nguyen, and Jian-Ying Wu. “Comparative study of phase-field damage models for hydrogen assisted cracking”. In: *Theoretical and Applied Fracture Mechanics* 111 (2021), p. 102840.
- [94] Shahed Rezaei et al. “A cohesive phase-field fracture model for chemo-mechanical environments: Studies on degradation in battery materials”. In: *Theoretical and Applied Fracture Mechanics* 124 (2023), p. 103758.

-
-
- [95] Aashique A Rezwan, Andrea M Jokisaari, and Michael R Tonks. “Modeling brittle fracture due to anisotropic thermal expansion in polycrystalline materials”. In: *Computational Materials Science* 194 (2021), p. 110407.
- [96] Lampros Svolos et al. “Anisotropic thermal-conductivity degradation in the phase-field method accounting for crack directionality”. In: *Engineering Fracture Mechanics* 245 (2021), p. 107554.
- [97] Peidong Li et al. “Phase-field modeling of hydro-thermally induced fracture in thermo-poroelastic media”. In: *Engineering Fracture Mechanics* 254 (2021), p. 107887.
- [98] Tushar Kanti Mandal et al. “Fracture of thermo-elastic solids: Phase-field modeling and new results with an efficient monolithic solver”. In: *Computer Methods in Applied Mechanics and Engineering* 376 (2021), p. 113648.
- [99] Hui Ruan et al. “A thermo-mechanical phase-field fracture model: Application to hot cracking simulations in additive manufacturing”. In: *Journal of the Mechanics and Physics of Solids* 172 (2023), p. 105169.
- [100] M Dittmann et al. “Phase-field modeling of porous-ductile fracture in non-linear thermo-elasto-plastic solids”. In: *Computer Methods in Applied Mechanics and Engineering* 361 (2020), p. 112730.
- [101] Lampros Svolos, Curt A Bronkhorst, and Haim Waisman. “Thermal-conductivity degradation across cracks in coupled thermo-mechanical systems modeled by the phase-field fracture method”. In: *Journal of the Mechanics and Physics of Solids* 137 (2020), p. 103861.
- [102] Luigi Ambrosio and Vincenzo Maria Tortorelli. “Approximation of functional depending on jumps by elliptic functional via t-convergence”. In: *Communications on Pure and Applied Mathematics* 43.8 (1990), pp. 999–1036.
- [103] Charlotte Kuhn, Alexander Schlüter, and Ralf Müller. “On degradation functions in phase field fracture models”. In: *Computational Materials Science* 108 (2015), pp. 374–384.
- [104] Bernard D Coleman and Walter Noll. “The thermodynamics of elastic materials with heat conduction and viscosity”. In: *The foundations of mechanics and thermodynamics*. Springer, 1974, pp. 145–156.
- [105] Eric Lorentz, Sam Cuvilliez, and Kyrylo Kazymyrenko. “Convergence of a gradient damage model toward a cohesive zone model”. In: *Comptes Rendus Mécanique* 339.1 (2011), pp. 20–26.

-
-
- [106] Jian-Ying Wu and Vinh Phu Nguyen. “A length scale insensitive phase-field damage model for brittle fracture”. In: *Journal of the Mechanics and Physics of Solids* 119 (2018), pp. 20–42.
- [107] Eric Lorentz. “A nonlocal damage model for plain concrete consistent with cohesive fracture”. In: *International Journal of Fracture* 207.2 (2017), pp. 123–159.
- [108] Shahed Rezaei et al. “An anisotropic cohesive fracture model: Advantages and limitations of length-scale insensitive phase-field damage models”. In: *Engineering Fracture Mechanics* 261 (2022), p. 108177.
- [109] M Dittmann et al. “Variational modeling of thermomechanical fracture and anisotropic frictional mortar contact problems with adhesion”. In: *Computational Mechanics* 63.3 (2019), pp. 571–591.
- [110] K Kitamura. “Crack surface energy: Temperature and force dependence”. In: *Materials transactions* (2008), pp. 0802120324–0802120324.
- [111] MR Bayoumi and MN Bassim. “Temperature dependence of fracture toughness J IC and ductility for BCC materials in the transition region”. In: *International Journal of Fracture* 23.4 (1983), pp. 259–269.
- [112] D Zakarian, A Khachatrian, and S Firstov. “Universal temperature dependence of Young’s modulus”. In: *Metal Powder Report* 74.4 (2019), pp. 204–206.
- [113] Jian-Ying Wu, Tushar Kanti Mandal, and Vinh Phu Nguyen. “A phase-field regularized cohesive zone model for hydrogen assisted cracking”. In: *Computer Methods in Applied Mechanics and Engineering* 358 (2020), p. 112614.
- [114] Cody J. Permann et al. “MOOSE: Enabling massively parallel multiphysics simulation”. In: *SoftwareX* 11 (2020), p. 100430.
- [115] Alexander Lindsay et al. In: *Nuclear Technology* 207.7 (2021), pp. 905–922.
- [116] Nicholas Malaya et al. “MASA: a library for verification using manufactured and analytical solutions”. In: *Engineering with Computers* 29.4 (2013), pp. 487–496.
- [117] Tianchen Hu, Johann Guilleminot, and John E Dolbow. “A phase-field model of fracture with frictionless contact and random fracture properties: Application to thin-film fracture and soil desiccation”. In: *Computer Methods in Applied Mechanics and Engineering* 368 (2020), p. 113106.
- [118] Raja Gopal Tangella, Pramod Kumbhar, and Ratna Kumar Annabattula. “Hybrid phase-field modeling of thermo-elastic crack propagation”. In: *International Journal for Computational Methods in Engineering Science and Mechanics* 23.1 (2022), pp. 29–44.

-
-
- [119] Tao Wang et al. “A phase-field model of thermo-elastic coupled brittle fracture with explicit time integration”. In: *Computational Mechanics* 65.5 (2020), pp. 1305–1321.
- [120] CP Jiang et al. “A study of the mechanism of formation and numerical simulations of crack patterns in ceramics subjected to thermal shock”. In: *Acta Materialia* 60.11 (2012), pp. 4540–4550.
- [121] Juan C Simo and Thomas JR Hughes. *Computational inelasticity*. Vol. 7. Springer Science & Business Media, 2006.
- [122] Marreddy Ambati, Roland Kruse, and Laura De Lorenzis. “A phase-field model for ductile fracture at finite strains and its experimental verification”. In: *Computational Mechanics* 57 (2016), pp. 149–167.
- [123] Ying Zhao et al. “Phase-field study of electrochemical reactions at exterior and interior interfaces in Li-ion battery electrode particles”. In: *Computer Methods in Applied Mechanics and Engineering* 312 (2016), pp. 428–446.
- [124] S Felder et al. “Thermo-mechanically coupled gradient-extended damage-plasticity modeling of metallic materials at finite strains”. In: *International Journal of Plasticity* 148 (2022), p. 103142.
- [125] Benjamin E. Grossman-Ponemon, Ataollah Mesgarnejad, and Alain Karma. “Phase-Field Modeling of Continuous Fatigue via Toughness Degradation”. In: *Engineering Fracture Mechanics* 264 (Apr. 2022), p. 108255.
- [126] Pietro Carrara et al. “A framework to model the fatigue behavior of brittle materials based on a variational phase-field approach”. In: *Computer Methods in Applied Mechanics and Engineering* 361 (2020), p. 112731.
- [127] Martha Seiler et al. “An Efficient Phase-Field Model for Fatigue Fracture in Ductile Materials”. In: *Engineering Fracture Mechanics* 224 (Feb. 2020), p. 106807.
- [128] Alexander D Lindsay et al. “2.0-MOOSE: Enabling massively parallel multiphysics simulation”. In: *SoftwareX* 20 (2022), p. 101202.
- [129] Satish Balay et al. “PETSc users manual”. In: (2019).
- [130] Derek R. Gaston et al. “Physics-based multiscale coupling for full core nuclear reactor simulation”. In: *Annals of Nuclear Energy* 84 (2015), pp. 45–54.
- [131] Serope Kalpakjian. *Manufacturing processes for engineering materials*. Pearson Education India, 1984.

-
-
- [132] Zhili Feng. “A computational analysis of thermal and mechanical conditions for weld metal solidification cracking”. In: *WELDING IN THE WORLD-LONDON-* 33 (1994), pp. 340–340.
- [133] SM Elahi et al. “Multiscale simulation of powder-bed fusion processing of metallic alloys”. In: *Computational Materials Science* 209 (2022), p. 111383.
- [134] Wojciech Stopyra et al. “Laser powder bed fusion of AA7075 alloy: Influence of process parameters on porosity and hot cracking”. In: *Additive Manufacturing* 35 (2020), p. 101270.
- [135] Christian Tenbrock et al. “Influence of keyhole and conduction mode melting for top-hat shaped beam profiles in laser powder bed fusion”. In: *Journal of Materials Processing Technology* 278 (2020), p. 116514.
- [136] Yangyiwei Yang et al. “Validated dimensionless scaling law for melt pool width in laser powder bed fusion”. In: *Journal of Materials Processing Technology* 299 (2022), p. 117316.
- [137] Min Yi, Bai-Xiang Xu, and Oliver Gutfleisch. “Computational study on microstructure evolution and magnetic property of laser additively manufactured magnetic materials”. In: *Computational Mechanics* 64.4 (2019), pp. 917–935.
- [138] Yingli Li et al. “Modeling temperature and residual stress fields in selective laser melting”. In: *International Journal of Mechanical Sciences* 136 (2018), pp. 24–35.
- [139] Zhidong Zhang et al. “3-Dimensional heat transfer modeling for laser powder-bed fusion additive manufacturing with volumetric heat sources based on varied thermal conductivity and absorptivity”. In: *Optics & Laser Technology* 109 (2019), pp. 297–312.
- [140] Xufei Lu et al. “Residual stress and distortion of rectangular and S-shaped Ti-6Al-4V parts by Directed Energy Deposition: Modelling and experimental calibration”. In: *Additive Manufacturing* 26 (2019), pp. 166–179.
- [141] Liang-Xing Lu, N Sridhar, and Yong-Wei Zhang. “Phase field simulation of powder bed-based additive manufacturing”. In: *Acta Materialia* 144 (2018), pp. 801–809.
- [142] Yangyiwei Yang et al. “Elasto-plastic residual stress analysis of selective sintered porous materials based on 3D-multilayer thermo-structural phase-field simulations”. In: *arXiv preprint arXiv:2310.13351* (2023).
- [143] Yangyiwei Yang et al. “Tailoring magnetic hysteresis of additive manufactured Fe-Ni permalloy via multiphysics-multiscale simulations of process-property relationships”. In: *npj Computational Materials* 9.1 (2023), p. 103.

-
-
- [144] Xiandong Zhou et al. “3D-multilayer simulation of microstructure and mechanical properties of porous materials by selective sintering”. In: *GAMM-Mitteilungen* 44.4 (2021), e202100017.
- [145] Bi Zhang, Yongtao Li, and Qian Bai. “Defect formation mechanisms in selective laser melting: a review”. In: *Chinese Journal of Mechanical Engineering* 30.3 (2017), pp. 515–527.
- [146] Wen Hao Kan et al. “A critical review on the effects of process-induced porosity on the mechanical properties of alloys fabricated by laser powder bed fusion”. In: *Journal of Materials Science* 57.21 (2022), pp. 9818–9865.
- [147] ZW Xu, A Liu, and XS Wang. “The influence of building direction on the fatigue crack propagation behavior of Ti6Al4V alloy produced by selective laser melting”. In: *Materials Science and Engineering: A* 767 (2019), p. 138409.
- [148] Rui Zou et al. “Isotropic and anisotropic elasticity and yielding of 3D printed material”. In: *Composites Part B: Engineering* 99 (2016), pp. 506–513.
- [149] Alain Karma, David A Kessler, and Herbert Levine. “Phase-field model of mode III dynamic fracture”. In: *Physical Review Letters* 87.4 (2001), p. 045501.
- [150] Marreddy Ambati, Tymofiy Gerasimov, and Laura De Lorenzis. “Phase-field modeling of ductile fracture”. In: *Computational Mechanics* 55.5 (2015), pp. 1017–1040.
- [151] Hui Ruan et al. “Phase-field ductile fracture simulations of thermal cracking in additive manufacturing”. In: *Journal of the Mechanics and Physics of Solids* (2024), p. 105756.
- [152] Bin Li et al. “Phase-field modeling and simulation of fracture in brittle materials with strongly anisotropic surface energy”. In: *International Journal for Numerical Methods in Engineering* 102.3-4 (2015), pp. 711–727.
- [153] S Teichtmeister et al. “Phase field modeling of fracture in anisotropic brittle solids”. In: *International Journal of Non-Linear Mechanics* 97 (2017), pp. 1–21.
- [154] Christoph Schreiber et al. “A phase field modeling approach of crack growth in materials with anisotropic fracture toughness”. In: *2nd International Conference of the DFG International Research Training Group 2057–Physical Modeling for Virtual Manufacturing (iPMVM 2020)*. Schloss-Dagstuhl-Leibniz Zentrum für Informatik. 2021.
- [155] Shahed Rezaei et al. “An anisotropic cohesive fracture model: Advantages and limitations of length-scale insensitive phase-field damage models”. In: *Engineering Fracture Mechanics* 261 (2022), p. 108177.

-
-
- [156] Bo Yin and Michael Kaliske. “An anisotropic phase-field model based on the equivalent crack surface energy density at finite strain”. In: *Computer Methods in Applied Mechanics and Engineering* 369 (2020), p. 113202.
- [157] Eric C Bryant and WaiChing Sun. “A mixed-mode phase field fracture model in anisotropic rocks with consistent kinematics”. In: *Computer Methods in Applied Mechanics and Engineering* 342 (2018), pp. 561–584.
- [158] JD Clayton and JCMS Knap. “Phase field modeling of directional fracture in anisotropic polycrystals”. In: *Computational Materials Science* 98 (2015), pp. 158–169.
- [159] Pratheek Shanthraj et al. “Elasto-viscoplastic phase field modelling of anisotropic cleavage fracture”. In: *Journal of the Mechanics and Physics of Solids* 99 (2017), pp. 19–34.
- [160] Zhengkun Liu and Daniel Juhre. “Phase-field modelling of crack propagation in anisotropic polycrystalline materials”. In: *Procedia Structural Integrity* 13 (2018), pp. 787–792.
- [161] R Ma and W Sun. “Computational thermomechanics for crystalline rock”. In: *Part ii: Chemo-damage-plasticity and healing in strongly anisotropic polycrystals, Comput. Method Appl. M* 369 (2020).
- [162] Thanh-Tung Nguyen et al. “Multi-phase-field modeling of anisotropic crack propagation for polycrystalline materials”. In: *Computational Mechanics* 60 (2017), pp. 289–314.
- [163] Jeremy Bleyer and Roberto Alessi. “Phase-field modeling of anisotropic brittle fracture including several damage mechanisms”. In: *Computer Methods in Applied Mechanics and Engineering* 336 (2018), pp. 213–236.
- [164] Ran Ma and WaiChing Sun. “FFT-based solver for higher-order and multi-phase-field fracture models applied to strongly anisotropic brittle materials”. In: *Computer methods in applied Mechanics and engineering* 362 (2020), p. 112781.
- [165] Nishant Prajapati et al. “Brittle anisotropic fracture propagation in quartz sandstone: insights from phase-field simulations”. In: *Computational Geosciences* 24 (2020), pp. 1361–1376.
- [166] Christoph Herrmann et al. “Phase-field model for the simulation of brittle-anisotropic and ductile crack propagation in composite materials”. In: *Materials* 14.17 (2021), p. 4956.

-
-
- [167] Udit Pillai et al. “An anisotropic cohesive phase field model for quasi-brittle fractures in thin fibre-reinforced composites”. In: *Composite Structures* 252 (2020), p. 112635.
- [168] Hela Gmati et al. “A phase-field model for brittle fracture of anisotropic materials”. In: *International Journal for Numerical Methods in Engineering* 121.15 (2020), pp. 3362–3381.
- [169] Vincent Hakim and Alain Karma. “Crack path prediction in anisotropic brittle materials”. In: *Physical review letters* 95.23 (2005), p. 235501.
- [170] Yue Gao et al. “Theoretical and numerical prediction of crack path in the material with anisotropic fracture toughness”. In: *Engineering Fracture Mechanics* 180 (2017), pp. 330–347.
- [171] Shuaifang Zhang, Wen Jiang, and Michael R Tonks. “A new phase field fracture model for brittle materials that accounts for elastic anisotropy”. In: *Computer Methods in Applied Mechanics and Engineering* 358 (2020), p. 112643.
- [172] Shuaifang Zhang et al. “A phase field model of crack propagation in anisotropic brittle materials with preferred fracture planes”. In: *Computational Materials Science* 193 (2021), p. 110400.
- [173] Jean-Michel Scherer, Stella Brach, and Jeremy Bleyer. “An assessment of anisotropic phase-field models of brittle fracture”. In: *Computer Methods in Applied Mechanics and Engineering* 395 (2022), p. 115036.
- [174] Zhiheng Luo et al. “A phase-field fracture model for brittle anisotropic materials”. In: *Computational Mechanics* 70.5 (2022), pp. 931–943.
- [175] Hirshikesh Hirshikesh and Alankar Alankar. “On the interplay of elastic anisotropy and fracture toughness anisotropy in fracture of single and multiphase polycrystals”. In: *Engineering Fracture Mechanics* 273 (2022), p. 108696.
- [176] Pengfei Li et al. “Anisotropic elastoplastic phase field fracture modeling of 3D printed materials”. In: *Computer Methods in Applied Mechanics and Engineering* 386 (2021), p. 114086.

Curriculum Vitae

Personal

Name Hui Ruan
Date of birth August 1994
Place of birth Anhui, China
Nationality Chinese

Education

- 12.2020 - Today Ph.D. Candidate in Materials Science
Thesis: Phase-field modeling of thermal fracture and its applications to Additive Manufacturing
Advisor: Prof. Bai-Xiang Xu & Prof. Dietmar Gross
Technische Universität Darmstadt, Darmstadt, Germany
- 09.2017 - 02.2020 M. Sc. in Aerospace Engineering
Thesis: An Efficient Numerical Simulation Method for WAAM of Large Metal Components
Advisor: Prof. Leiting Dong & Prof. Peng Yan
Beihang University, Beijing, China
- 09.2013 - 06.2017 B. Sc. in Aerospace Engineering
Thesis: Analysis of Stability and Maneuverability of Unmanned Flight Vehicles
Advisor: Prof. Huaming Wang
Nanjing University of Aeronautics and Astronautics, Nanjing, China

List of Publications

Journal Publications

- [1] **Hui Ruan**, Xiang-Long Peng, Yangyiwei Yang, Dietmar Gross, Bai-Xiang Xu. (2024) Phase-field ductile fracture simulations of thermal cracking in additive manufacturing. *Journal of the Mechanics and Physics of Solids*, 105756. <https://doi.org/10.1016/j.jmps.2024.105756>
- [2] **Hui Ruan**, Shahed Rezaei, Yangyiwei Yang, Dietmar Gross, Bai-Xiang Xu. (2023). A thermo-mechanical phase-field fracture model: Application to hot cracking simulations in additive manufacturing. *Journal of the Mechanics and Physics of Solids*, 172, 105169. <https://doi.org/10.1016/j.jmps.2022.105169>
- [3] Mohammad Reza Khosravani, Shahed Rezaei, **Hui Ruan**, Tamara Reinicke. (2022). Fracture behavior of anisotropic 3D-printed parts: Experiments and numerical simulations. *Journal of Materials Research and Technology*, 19, 1260-1270. <https://doi.org/10.1016/j.jmrt.2022.05.068>
- [4] Shahed Rezaei, Jacob Niikoi Okoe-Amon, Cerun Alex Varkey, Armin Asheri, **Hui Ruan**, Bai-Xiang Xu. (2023). A cohesive phase-field fracture model for chemo-mechanical environments: Studies on degradation in battery materials. *Theoretical and Applied Fracture Mechanics*, 124, 103758. <https://doi.org/10.1016/j.tafmec.2023.103758>

Contributions to conferences

- 18th European Mechanics of Materials Conference, April 2022, Oxford, UK.
- 8th GAMM Workshop on Phase-field modeling, February 2023, Zurich, Switzerland.
- 2nd FRASCAL Symposium, March 2023, Erlangen, Germany.
- 93rd GAMM Annual Meeting, June 2023, Dresden, Germany.
- 9th GAMM Workshop on Phase-field modeling, February 2024, Dresden, Germany.
- 9th European Congress on Computational Methods in Applied Sciences and Engineering, June 2024, Lisboa, Portugal.
- 2nd GIMC SIMAI YOUNG 2024, July 2024, Naples, Italy